Integrated Micromachined Quantum Barrier Mixers for High Harmonic Number Millimeter Wave Receivers

By

L. W.Y Liu, B Eng (Hon)

Submitted in accordance with the requirements for the degree of the Doctor of Philosophy

University of Leeds
Institutes of Microwaves and Photonics
Woodhouse Land
Leeds LS2 9JT
United Kingdom

January, 2002

The candidate confirms that the work submitted is his/her own and that appropriate credit has been given where reference has been made to the work of others.

Acknowledgements

The author wishes to express his sincere gratitude to all those who provided valuable assistance and support throughout the project, and in the preparation of the manuscript. In particular, to Dr. David Paul Steenson of University of Leeds, Prof. Michael Steer of Unversity of Carolina, Dr. Jay Guo of Unverisity of Michigan, Dr. Xiao Ming Duan of Da La Rue and Dr. G. Jian and other colleagues in industry.

Abstract

This thesis presents the results of my endeavours at Leeds on research into subharmonic mixing employing double barrier resonant tunneling device (Quantum Barrier Device) at microwave and millimeter wave frequencies and an enabling technology for future improvement of the Quantum Barrier mixer. The research commenced with an empirical study of the electrical characteristics of a typical Quantum Barrier Device, and a model was developed to accurately simulate the discontinuities in the current-voltage characteristic as well as the capacitance-voltage behavior in the dc and the frequency domain. With a detailed analytical model, a general theory of subharmonic mixing was derived to demonstrate, with experimental proof , factors which favor the use of a Quantum Barrier Device as a mixing device at microwave frequencies, and to reveal any shortcomings. Measurements of a mixer at microwave frequencies and a harmonic multiplier at millimeter wave frequencies were also carried out, and presented with suggestions for possible improvements on the existing Quantum Barrier Device structure. In addition, several novel polymer-based micromachining technologies were developed for integration of these high frequency devices in the future, and presented in this thesis with S-parameter measurements. Particular reference was given to a handful of membrane-based micromachining technologies that enable a planar membrane-based printed circuit to be fabricated on a 5 micron thick polymer membrane in the absence of any steps involving thermal oxidation and low pressure chemical vapor deposition (LPCVD). The relatively low-cost low-temperature process uses a photosensitive resin (SU-8) to form a self-supporting membrane to which active devices can be mounted. Measured losses of transmission lines in these technologies are typically no more than 0.5 dB/cm at W-band, and this performance is comparable to the existing GaAs (or Silicon) membrane technologies.

Contents

CONTENTS ... iii
LIST OF ILLUSTRATIONS ... vii
CHAPTER 1: INTRODUCTION ... 1
1.1 BACKGROUND ... 1
1.2 MIXER IN GENERAL ... 1
1.3 QUANTUM BARRIER DEVICES, PROS AND CONS ... 3
1.4 ORGANIZATION OF THIS THESIS ... 5
1.5 A BRIEF REVIEW OF THE NOVEL AND ORIGINAL CONTRIBUTION OF THIS WORK AND ACHIEVEMENT THUS FAR ... 7
REFERENCES ... 11
CHAPTER 2: CHARACTERIZATION OF ELECTRICAL PARAMETERS OF RESONANT TUNNELING DIODES ... 13
2.1 INTRODUCTION ... 13
2.2 PRELIMINARY THEORY OF RTD'S ... 16
2.3 PHYSICS BASED CHARACTERIZTION OF ELECTRICAL BEHAVIOR ... 20
2.3.1 COHERENT TUNNELING CURRENT ... 20
2.3.2 CURRENT DUE TO INELASTIC SCATTERING ... 25
2.3.3 CURRENT-VOLTAGE CHACTERISTIC OF RTD ... 27
2.3.4 SKIN-RESISTANCES AT THE EMITTER AND THE COLLECTOR ... 28
2.3.5 BARRIER CAPACITANCE OF AN RTD ... 30
2.3.6 PROBLEMS OF CHACTERIZATION BASED ON THE PHYSICAL MODELS ... 31
2.4 MEASUREMENT BASED CHARACTERIZATION OF CURRENT-VOLTAGE RELATIONSHIP OF RTD ... 33
2.4.1 CONTINUITY FUNCTIONS ... 34

2.4.2 LOG-BASED CONTINUITY FUNCTION.......35
2.4.3 STEP FUNCTION APPROACH.......36
2.4.4 DEMONSTRATION OF MODELING OF NONLINEAR CONDUCTANCE OF RESONANT TUNNELING DIODE.......37
2.4.5 HARMONIC CONTENTS RESULTING FROM THE SHARP DISCONTINUITIES IN THE I-V CHARACTERISTIC.......41
2.5 MEASUREMENT BASED CAPACITACE CHARACTERIZATION OF NONLINEAR DEVICE IN FREQUENCY DOMAIN.......44
2.5.1 METHOD OF SOLUTIONS.......46
2.5.2 DEMONSTRATION: CHARACTERATION OF RESONANT TUNNELING DEVICE CAPACITANCE.......55
2.6. SIMULATION MODEL OF SKIN LOSSES.......58
2.7 CONCLUSIONS.......61
REFERENCES.......62
CHAPTER 3: THEORY OF SUBHARMONIC MIXING.......65
3.1 INTRODUCTION.......65
3.2 DOUBLE BARRIER DEVICE AS A MIXING DEVICE.......66
3.2 DOUBLE BARRIER DEVICE AS A MIXING DEVICE.......68
3.3. QUALITATIVE TREATMENT.......69
3.3.1 DECOMPOSITION OF RESISTIVE CURRENT INTO HARMONIC SUM (WEAKLY NONLINEAR CASE).......70
3.3.2 DECOMPOSITION OF CAPACITANCE CURRENT INTO HARMONIC SUM (WEAKLY NONLINEAR CASE).......73
3.3.3 OVERALL MIXING EQUIVALENT.......75
3.3.4 IF VOLTAGE.......79
3.4 IMPLICATIONS FOR QBD-BASED SUBHAMONIC MIXER WITH LIMITED LOCAL OSCILLATOR PUMP.......81
3.4.1 VOLTAGE-INDEPENDENT ADMITTANCE AND UNBIASED CAPACITANCE.......81
3.4.2 FIRST MINIMUM CONVERSION LOSS.......85

3.4.3 IMPLICATIONS OF MULTIPLE MINIMA (MAXIMA) IN CONVERSION LOSS 88
3.5 EXPERIMENTAL FINDINGS ON THE EFFECTS OF VOLTAGE-INDEPENDENCE IN CONDUCTANCE 88
3.6. THE DEVICE WITH STRONGLY NONLINEAR CHARACTERISTIC 93
3.7. DISCUSSIONS AND CONCLUSIONS 99
REFERENCES 100
CHAPTER 4: PLANAR CIRCUIT TECHNOLOGY 103
4.1 INTRODUCTION 103
4.2 MICROMACHINING IN GENERAL 104
4.3 FLOW OF THE CHAPTER 108
4.4 EMBEDDED SUBMILLIMETER WAVE COMPONENTS USING PHOTOSENSITIVE RESIN MICROMACHINING 109
4.4.1 MICROFABRICATION PROCEDURES OF EMBEDDED RECTANGULAR WAVEGUIDES 110
4.4.2 MICROFABRICATION PROCEDURES OF E-PLANE COMPONENTS 113
4.4.3 MEASUREMENTS OF WAVEGUIDE AND ULTRA-THIN POLYMER E-PLANE CIRCUITS AT W-BAND 114
4.5 POLYMER MEMBRANE-SUPPORTED CPWS WITH MOUNTED ACTIVE DEVICES 117
4.5.1 LOSS AND DISPERSION CONSIDERATIONS 118
4.5.2 POLYMER-MEMBRANE-SUPPORTED CPWS 118
4.5.3 MICROFABRICATION PROCEDURES FOR POLYMER-MEMEBRANE-SUPPORTED CPWS 119
4.5.4 EXPERIMENTAL RESULTS OF PLANAR MEMBRANE-SUPPORTED CPWS 121
4.5.5 QUALITATIVE TREATMENT OF MEMBRANE SUPPORTED CPWS 122
4.6 POLYMER-MEMBRANE-SUPPORTED COPPER E-PLANE CIRCUITS 134
4.6.1 INSULATED/NON-INSULATED MEMBRANE-SUPPORTED E-PLANE CIRCUITS 136
4.6.2 MEASUREMENTS OF INSULATED POLYMER-MEMBRANE-SUPPORTED

E-PLANE CIRCUITS 137
4.7 COPPER-ON-POLYMER-MEMBRANE BOARDS 141
4.7.1 MASS PRODUCTION OF PRINTED CIRCUITS USING COPPER-ON-MEMBRANE BOARDS 142
4.7.2 EXPERIMENTAL RESULTS OF COPPER-ON-MEMBRANE BOARDS 143
4.7.3 FURTHER EXTENTIONS OF THE EXISTING MEMBRANE BOARD TECHNOLOGY 144
4.8 CONCLUSIONS 148
REFERENCES 149
CHAPTER 5: DESIGN AND MEASUREMENT OF QBD MIXER/MULTIPLIER 153
5.1 INTRODUCTION 153
5.2 QBD DOWN-CONVERTER FROM 18 GHZ TO 1 GHZ USING A QUANTUM BARRIER RESONANT TUNNELING DIODE WITH ANTI-SYMMETRIC CONDUCTANCE 153
5.3 QBD FREQUENCY MULTIPLIER, 20-TO-100 GHZ 160
5.4 CONCLUSIONS 165
REFERENCES 165
CHAPTER 6: FUTURE WORK 168
6.1 INTRODUCTION 168
6.2 REDUCTION OF VALLEY CURRENT IN RTD 168
6.3 PHYSICAL MODEL OF NONLINEAR RTD CAPACITANCE 169
6.4 CASCADE OF MULTIPLE DOUBLE-BARRIER STRUCTURES AS A MIXING DEVICE, BY EPITAXIAL GROWTH 169
6.6 CIRCUIT INTEGRATION BY HIGH RESOLUTION 3-D MICROMACHINING 171
6.7 CONCLUSIONS 173
REFERENCES 174
CHAPTER 7: CONCLUSIONS 177
7.1 INTRODUCTION 177
7.2 SUMMARY AND CONCLUSIONS 177
APPENDIX 1 – LISTING OF HARMONIC DECOMPOSITION PROGRAM 181

List of Illustrations

Fig. 2.1.1 Equivalent circuit of an Resonant Tunneling Diode....14

Fig. 2.2.1 (a) Basic configuration of a typical RTD, and (b) Related conduction and valence band structure....17

Fig. 2.2.2 Current-voltage Relationship of a Typical Double Barrier RTD. 20

Fig. 2.3.1 (a) $SS(V)$ against different resonant width W 's. (b) $J_t(V)$ against different resonant width W 's....24

Fig. 2.3.2 Current density $J_t(V)$ against different E_F 's....25

Fig. 2.3.2.1 Current-voltage relationship of a Quantum Barrier Device (a) at 290K, (b) at 77K. 27

Fig. 2.3.3 Calculated current-voltage characteristic of a real RTD....28

Fig. 2.3.5.1 (a) Band diagram of the tunneling structure; (b) the small-signal equivalent circuit modeling the band diagram in (a)....31

Fig. 2.4.4.1 Modeled I-V characteristic of the RTD, obtained from Equation 2.4.4.3. 40

Fig. 2.4.4.2 Relative discrepancies (in percent) between the modeled IV characteristic and that measured....40

Fig.2.6.2.1 Schematic of Experimental Setup for CV Measurement....56

Table 2.5.1.1 Measured and simulated output harmonics at Rload, when the source was fundamentally driven at Power=7.5 dbm and frequency = 2 Ghz....57

Fig. 2.6.1 (a) Cross-sectional view of a round wire with 4 current carrying shell; and (b) The equilivent ladder network modeling the skin effect of the round wire. Here R_i and L_i respectively represents the resistance and the inductance of the i-th shell. 59

Fig. 2.6.2 (a) Cross-sectional view of a round wire; (b) Sen et al [19] equilivent network modeling the skin effect of the round wire. Here R_i and L_i respectively represents the resistance and the inductance of the i-th shell....61

Table 3.1.1 Comparison between Quantrum Barrier performance and Schottky performance68
Fig. 3.2.1 Equivalent circuit of a nonlinear diode....69
Fig. 3.2.2 Equivalent circuit of the embedding impedance for harmonic *n*....76
Fig. 3.4.1.1 Illustration of Voltage-independent Conductance, a_1 83
Fig. 3.4.2.2 (a) Measured IF power versus LO power characteristic. (b) Simulated conversion loss versus LO power (CL=conversion loss)....88
Fig. 3.5.1 Layout of the Test Fixture....89
Fig. 3.5.2 (a) Measured *I-V* characteristic of QBD of 10 μ m in diameter (voltage-independent conductance = 0.0016). (b) Measured IF power against LO frequency for LO power = 0 dBm, RF frequency = 20 GHz, RF power = -20 dBm....91
Fig. 3.5.3 (a) Measured *I-V* characteristic of QBD of 10 μ m in diameter (voltage-independent conductance = 0.024). (b) Measured IF power against LO frequency for different LO power, RF frequency = 18 GHz, RF power =-23 dBm....93
Fig. 4.4.1 An Example E-plane Circuit....110
Fig. 4.4.2.1 A metal block, with an oversized waveguide channel....112
Fig. 4.4.2.2 Oversized waveguide channel filled with SU-8....112
Fig. 4.4.2.3 Metal block with the required waveguide channel....113
Fig. 4.4.3.1 A glass slide with metalization pattern on the silver coated surface....115
Fig. 4.4.3.2 Metalization pattern, topped with an SU-8 layer....115
Fig. 4.4.3.3 The finished samples after step 3: (a) Waveguide-to-finline transition; (b) Finline resonantor....116
Fig 4.4.3.4 Measured performance of an E-plane transition realized on an SU-8 substrate with 0.05mm in thickness....116
Fig 4.4.3.5 Measured guide wavelength versus free-space wavelength (SU-8 substrate thickness = 0.05 mm)....117
Fig. 4.5.1 Fabrication steps for a membrance-supported CPW with mounted active device. 131
Fig. 4.5.2 A bath of thin photosensitive resin (SU-8), contained in a hand-assembled container formed using glass slides....132

Fig. 4.5.3 Membrane-supported coplanar waveguides of different lengths (line width = 50 μm, gap = 40 μm, membrane thickness < 5 μm, membrane distance away from ground = 110 μm). 132

Fig. 4.5.4 Method of mounting a device onto a printed circuit supported by an polymer membrane (photo taken from the back-side of the membrane-supported coplanar waveguide test-set). 133

Fig. 4.5.5 Measured S-parameters for a 50 Ω membrane-supported CPW line. (metal thickness = 200 nm, line length = 1.55 mm). 133

Fig. 4.5.6 Cross-sectional view of the Membrane-supported CPW. 134

Fig. 4.5.7 Cross-sectional view of non-leaky CPW.($\varepsilon_2 = \varepsilon_3$, $\varepsilon_1 = \varepsilon_4$ and $\varepsilon_3, \varepsilon_2 > \varepsilon_4, \varepsilon_1$). 134

Fig. 4.6.1 Fabrication steps of insulated membrance-supported E-plane circuits with a mounted active device. 139

Fig. 4.6.2 Photograph of finline resonator of length 1.8 mm shown mounted in half of a split block waveguide, with metalalization of 5 microns thick 139

Fig. 4.6.3 Measured S-parameters of a finline resonator , with resonant frequency = 81.5 GHz, resonator length = 1.8 mm. 140

Fig. 4.6.4 Photograph of E-plane ladder bandpass filter shown mounted in half of a split block waveguide, with metalization thickness = 5 μm. 140

Fig. 4.6.5 Measured S-parameters of a bandpass filter with passband frequency centered at 107 GHz 141

Table 4.7.4 The thermal expansion coefficient (TCE) for different materials 145

Fig. 4.7.1 Cross sectional view of single-sided Copper-on-Membrane board. 146

Fig. 4.7.2 Steps for realization of membrane-based printed circuit from a Copper-on-Membrane board of Fig. 4.7.1 147

Fig. 4.7.3 A pair of back-to-back membrane-supported finline-to-waveguide transitions. 147

Fig. 4.7.4 Measured S-parameters of the two finline-to-waveguide transitions connected back-to-back. 148

Fig. 5.2.1 Subharmonic 18-to-1 Ghz Quantum Barrier Mixer (a) Schematic Diagram; (b)

Layout. 156

Fig. 5.2.2 Layer Profile of the QBD used in this Experiment, Device Diameter=10 microns. 157

Fig. 5.2.3 QBD mounted in a LID package.......... 157

Fig. 5.2.4 Voltage-dependent Conductance of the QBD.......... 158

Fig. 5.2.5 Voltage-dependent Capacitance of the QBD (The dashed regions are interpolated regions). 158

Fig. 5.2.6 Measured Conversion Loss versus IF Frequency (LO Power = 0 dBm, RF Power = -20 dBm, RF Frequency = 18 Ghz, Harmonic Number=2).......... 159

Fig. 5.2.7 Noise Measurement Setup (Measured Noise Figure = 9 dB).......... 159

Fig. 5.3.1 Quantum Barrier Device used in the multiplier experiment (a) Cross-sectional layer profile [19]; (b) current voltage characteristic. (device diameter = 10 microns).......... 162

Fig. 5.3.2 Layout of the x5 Quantum Barrier Multiplier. 162

Fig. 5.3.3 Multiplier output versus bias voltage (fundamental signal @ 20 Ghz, 17 dbm).... 163

Table. 5.3.1 Comparison between the measured multiplier output and simulated output. (fundamental signal @ 20 Ghz, 17 dbm) 163

Fig. 5.3.4 (a) Mutiplier output measured in spectral domain the quantum barrier device is biased to 0.5 volts and (b) Multiplier output measured in spectral domain when the device is unbiased. (Input at 17 dbm, at 20 Ghz) 164

Chapter 1: Introduction

1.1 BACKGROUND

This thesis presents the outcome of research into subharmonic mixing employing a double barrier resonant tunneling device (Quantum Barrier Device) at microwave and millimeter wave frequencies. The first part of the work is largely an investigation into the nature of the underlying phenomena, which leads to the mixing behavior and the analysis given in this thesis takes into account effects on the conversion loss of the strongly nonlinear device conductance, capacitance and skin effects. To start with, the pros and cons of double barrier resonant tunneling devices are first identified. An empirical study of the electrical characteristics of a typical quantum barrier device is presented, and a model is developed to accurately simulate the discontinuities in the current-voltage characteristic as well as the capacitance-voltage behavior. With a detailed analytical model, a general theory of subharmonic mixing is derived, with particular attention given to subharmonic mixing using a quantum barrier device. Practical implementation and technological issues form the major part of this work and have been carefully studied with one of the aims being to develop a mixer on a dielectric-free transmission media. Measurements of a mixer at microwave frequencies and a harmonic multiplier at millimeter wave frequencies were carried out and presented with suggestions on possible improvements on the existing Quantum Barrier Device structure. Other enabling technologies are also considered in this work as a foundation for future studies.

1.2 MIXER IN GENERAL

The first published analytical study of mixer started in World War II by Torrey and Whitmer

[18]. Those mixers were mainly intended for down-conversion of signals operating at microwave frequencies. Over decades of evolution, the operating frequencies of the mixers have been extended from microwave to terahertz frequencies [10-17]. Presently , almost all the terahertz frequency-conversion architectures are non-crynogenic and implemented in a membrane-supported dielectric-less transmission medium [17]. With this approach, all the circuit components are totally integrated in a 3-micron thick GaAs membrane, without the need for whisker electrical contacting in any form. The highest operating frequency that has been attained using this approach exceeds 2.5 Thz [12]. Like the conventional silicon membrane technologies [17], the cost of realization using a similar GaAs membrane is very high.

The mixing devices for terahertz mixers [12, 19] are typically non-crynogenic Schottky diodes, with junction capacitance less than 5 fF. These kinds of Schottky diodes are commercially available, at around US$2000 per piece. Though these are expensive, some commercial companies offer cheaper alternatives for operation at low submillimeter wave frequencies, e.g. silicon based GaAs diodes with junction capacitance less than 50 fF are offered by Alpha Micro at around US$1 per piece. Although these diodes appear to offer good alternative to realize some of the project goals of this research, the objective was to use a Quantum Barrier Diode. The Quantum Barrier Diode essentially consists of a double-barrier resonant tunneling diode, with barrier thickness as of 1.4 nm. The original concept was to exploit the quantum barrier devices' strong nonlinearity and nonlinear negative differential resistance regions, which should be able to offer non-schottky mixing characteristics. While a Schottky device exhibits a monotonic decrease in conversion efficiency, as the harmonic order of the mixing increases, it has been proven both experimentally and analytically that this monotonic decrease in mixing efficiency does not necessary apply to quantum barrier devices with negative resistance regions.

Despite considerable research on Quantum Barrier Devices and RTDs, they remain restricted to only a few niche applications. Presently, there have not been any physics-based models, which accurately describe both the current-voltage and capacitance-voltage

characteristics of a quantum barrier RTD. Hence, the objective of this research was to achieve following results:

1) To develop a simulation model of Quantum Barrier Devices from the dc and frequency-domain measurements.
2) To demonstrate with analysis and experimental proof the factors which favor the use of a quantum barrier diode as a mixing device at microwave frequencies, and to reveal any shortcomings.
3) Finally, to develop a low-cost micromachining technology with performance comparable to the existing GaAs (or Silicon) membrane technology, for integration of these high frequency devices in the future.

In the sections that follow, a fair assessment of the present capabilities of RTDs will be presented, with suggestions on possible improvements. Although the present performance of RTDs does not favor significant industrial support, we have developed a number of very important micromachining technologies, which not only cost-effectively revolutionize the current membrane technologies, but also generate a number of routes for realizing mixers in the future.

1.3 QUANTUM BARRIER DEVICES, PROS AND CONS

Resonant tunneling diodes (RTDs) were first demonstrated by Esaki and Tsu [1]. Subsequently, over a thousand of research publications have been written on various aspects of the resonant tunneling devices, including physical modeling, fabrication technology and electronic applications. In electronic applications, Sollner et al [10] successfully demonstrated resonant tunneling and detection up to 2.5 THz. Since then, the negative conductance of RTDs has generated interest for power generation at millimeter-wave frequencies. Brown et al [3], for example, demonstrated oscillations up to 712 Ghz in an InAs/AlSb double barrier RTD. For frequencies above 90 Ghz, the maximum output power from a single double barrier RTD has

been below 0.1 mW. However, it is theoretically feasible to increase the output power by a device-level integration, which stacks a number of RTD layers in series. In addition to these unique features, other advantages of RTD are:

1) RTDs are suited to integration with other high-speed three-terminal devices, such as heterojunciton bipolar transistors (HBTs) or heterojunciton field-effect transistors (HFETs). When used as the base-emitter junctions in bipolar transistors (HBTs) , they can form three terminal resonant tunneling transistor (RTTs). Recently, surface tunneling transistors (STTs) have been proposed to incorporate resonant tunneling in the channel of a FET. RTDs and high electron mobility transistors (HEMTs) have been successfully co-integrated to demonstrate a number of mult-gigahertz digital circuits [9]. These possibilities of combining RTDs with three-terminal devices have been very effective in enhancing the device performance [5-9], while avoiding the problems of isolation between input and output.
2) The capacitance of an RTD can be reduced by an added depletion layer adjacent to the double-barrier quantum well, so that the cut-off frequency is increased. This also has effects of increasing the voltage between the peak and the valley, thus increasing the potential output power of such devices.

However, each new technology must be critically assessed and compared with existing alternatives. After more than three decades of development, RTDs still have not been adopted by industry or even government laboratories for millimeter wave electronic applications. The original proposal of this research was to develop an 180Ghz mixer based on an RTD, but despite considerable progress in meeting many of the technological challenges, successful demonstration of using this device as a submillimeter mixer may not be forthcoming. Whether RTDs will find their way to mainstream electronics in future, remains uncertain. Nevertheless, it is highly useful to understand the reasons behind its present failure to gain industrial acceptance. The main reasons seem to be the following:

1) RTDs have a finite zero-bias conductance, which, in turns, generates little or no isolation between the emitter and the collector when used as a two-terminal active device. This creates problems when the device is intended for high-frequency rectification. As will be demonstrated in Chapter 3, this finite zero-bias conductance is also a disadvantage when the device is used as a mixing device.
2) The cost of fabrication of RTDs are extremely high. Also, the reproducibility, device matching, and control over device characteristics are still not resolved.
3) The peak-to-valley current ratio (PVCR) of GaAs based RTDs are generally small, i.e. ~2.5. Even though for digital circuit applications, where large PVCR may not be necessary, low PVCR may lead to low noise margins and hence poor performance. When used as an oscillating device, RTDs have not been demonstrated to be as good in efficiency as varactor, Gunn and IMPATT diodes.

In order for RTDs to be adopted by in industry, a considerable amount of improvement is needed in fabrication technology so far as yield and reliability are concerned. At the moment, most of the RTD modeling research activities are centered on understanding the current-voltage characteristic of the device, ignoring the voltage-dependence capacitance ---- which is the most importance aspect for applications beyond microwave frequencies. Accurate prediction of voltage-dependent current and capacitance characteristics requires accurate modeling of not only coherent resonant tunneling but also the other important phenomena affecting the RTD device performance, such as inelastic scattering, skin effect and electromigration that generates critical problems at nanometric scale, etc.

1.4 ORGANIZATION OF THIS THESIS

The following paragraphs outline the thesis content and its organization:

Chapter 2 presents the all modeling aspects of a resonant tunneling diode. Starting with a

general review on the physics-based modeling, this chapter explains why the existing physics-based models are not going to be adequate for circuit simulations. The negative resistance regions of an RTD are highly discontinuous. To be able to model the discontinuities exactly, we incorporate the step-function based continuity function into our measurement based modeling of the current-voltage and capacitance-voltage characteristics. Skin effect resistance of the RTD is also discussed in this chapter.

Chapter 3 presents the general subharmonic mixing theories, which is applicable to all resistive mixing devices. Particular reference is given to subharmonic mixing using a quantum barrier RTD. The features of an RTD in mixing applications are further elaborated. Suggestions on how to tailor the nonlinearity of the device are also given at the end of this chapter.

Chapter 4 presents the implementation issues. Our solutions for incorporating the RTD devices were originally intended for transmission line above 100 Ghz and implementation was based on a handful of novel polymer-based micromachining techniques, including embedded-polymer-based waveguide, polymer-membrane-supported coplanar waveguides, polymer-membrane-supported copper E-plane circuits as well as a methodology to mass-produce polymer-membrane-supported components. In this chapter, an introduction to other standard micromachining technologies is also critically reviewed. Our newly discovered polymer-based micromachining techniques are then presented, together with measurements to 110 Ghz. Some critical transmission parameters are presented, with self-contained analytical derivations where possible. These parameters include the relative dielectric constant of membrane-supported CPW, dispersion effects, dielectric loss and the radiation loss due to leaky parallel plate mode.

Chapter 5 presents the measurement of our 18-to-1 Ghz x2 Quantum Barrier Subharmonic Mixer and 20-to-100 x5 Ghz Quantum Barrier Multiplier. At microwave frequencies, the measurement of our subharmonic mixer using our Quantum Barrier Device reveals for the first

time that its conversion loss is less than 7 dB. The noise figure is around 9 dB using an LO pump at 20 dBm at 18.5 Ghz. Most of our resonant tunneling devices which were available cuts off at around 40 Ghz. As will be demonstrated by measurement, this then significantly degrades the frequency-conversion efficiency at W-band.

Chapter 6 points the way to future work for this research. The future work covers some remaining unresolved issues of the RTD modeling work, and feasibility study of total integration for applications at millimeter wave and sub-millimeter wave frequencies.

Chapter 7 presents a final summary and review of the work.

1.5 A BRIEF REVIEW OF THE NOVEL AND ORIGINAL CONTRIBUTION OF THIS WORK AND ACHIEVEMENT THUS FAR

There were four main pieces of analytical work in this research:

1) *Development of power-series based approach of characterizing weakly nonlinear electrical behaviors (Chapter 2).* Power-series based approach provides easy access to frequency domain information and, in general, suffices to model weakly nonlinear devices.
2) *Development of continuity-function based technique for characterizing the current voltage characteristic of an RTD (Section 2.4).* Quantum Barrier Device is strongly nonlinear in nature, with sharp transitions in its current-voltage characteristic and capacitance characteristic. Modeling the electrical characteristics of Quantum Barrier Device using the power-series based approach tends to over-smooth the sharp discontinuities in the electrical characteristics, and very often ends up with inaccuracy in frequency domain analysis. To compensate this over-smoothing effect, this thesis reports a continuity-function approach that can effectively capture the harmonic contents embedded in each sharp transition in the electrical characteristic. In addition to improvement in modeling accuracy, the

continuity-function based approach also resolves many convergence-failures in simulation resulting from other modeling approaches reported in the open literature.

3) *Examination of the harmonic contents resulting from sharp discontinuities (Section 2.4.5).* The harmonic contents resulting from the sharp discontinuities in the electrical behaviors of a quantum barrier device can be visualized from numerical frequency-domain simulation, such as the well-known harmonic balance technique. However, numerical simulation will hardly reveal the criticality of certain physical parameters in the design of the Quantum Barrier Device. It is for this reason that the nonlinearity is empirically derived in relation to the sharpness and the threshold voltage of the transition in the electrical characteristic.
4) *Development of a frequency-domain algorithm to estimate the voltage-dependent capacitance for weakly nonlinear device (Section 2.5).* The voltage-dependent capacitance can be measured using a conventional capacitance-meter. But many conventional capacitance-meters are restricted to operating at frequencies below 1 Ghz and thus have difficulty in measuring device capacitances below 1 pF. The problem is particularly difficult to handle if the device contains negative-resistive elements which generate resonances at low frequencies. However, if the device is measured in the frequency domain, the device capacitance can be extracted using the available harmonic data and other dc-domain measurements. The frequency domain measurement technique can also be applied in conjunction with the continuity-function based modeling technique.

Since the quantum barrier device has non-Schottky electrical characteristics. Conventional mixer-theory based on the Schottky nonlinear electrical characteristics is not suitable to explain the nonlinear operation of the quantum barrier device as a mixing device, nor is it adequate to reveal the shortcoming of the quantum barrier devices in use in this research. For this reason, the following pieces of work were done:

1) *Development of an analysis of general subharmonic mixing theory particularly suitable for the requirements of quantum barrier mixer (Section 3.2-3.5).*
2) *Extension of subharmonic mixing theory, with consideration of the nonlinearities due to*

sharp discontinuities (Section 3.6).

The following summarizes the practical achievements which are mostly related to the polymer micromachining work undertaken during this research:

1) *Implementation of the first polymer-based embedded waveguide using thin photosensitive resin, with a return loss of 20 dB or better (Section 4.3).*
2) *Implementation of the first polymer-based membrane-supported coplanar waveguide with mounted devices, with a near dielectric-free transmission line region and a loss of around 1 db/mm in an open structure (Section 4.4).*
3) *Implementation of the first polymer-based self-supporting membrane-supported E-plane circuits, with a loss of less than 0.5 dB/cm (Section 4.5)*
4) *Implementation of the first copper-on-membrane board for mass-reduction of membrane-support E-plane circuits, mimicking the copper-clapped Duriod board, to simplify the processing of polymer membrane technologies (Section 4.6).*
5) *Implementation of the second subharmonically pumped downconverter from 20 Ghz to 1 Ghz employing Quantum Barrier Device, with a conversion loss below 8 dB and noise figure below 9 dB (Section 5.2).*

Altogether the previously described work resulted in (or contributed to) more than 13 publications, of which there were four journals and five referred conference papers.

1) W.Y. Liu, D.P. Steenson, "18-to-2 GHz Subharmonically Pumped downconverter using a Quantum Barrier Device with Symmetric Conductance", *PREP99*, Jan, 1999.
2) W.Y. Liu, D.P. Steenson, "Investigation of Subharmonically Excited Quantum Barrier Mixers", *Microwave Theory and Techniques, IEEE Transactions on,* Vol. 48, No. 4, Part 2, pp 757-763, April, 2000.
3) W.Y. Liu, D.P. Steenson, "Demonstration of Subharmonically Excited Quantum

Barrier Mixers", *SPIE*, April, 1999.

4) W.Y. Liu, D.P. Steenson, M.B.Steer, "A Technique of Micromachining Suitable For Fabrication of Submillimeter Wave Components", *The First International Symposium on Laser Precision Microfabrication, Japan*, September, 2000.
5) W.Y. Liu, "Novel Technique of Thin Photoresist Micromachining for Submillimeter Wave Circuits", *SPIE*, Vol 4176-28, September 2000.
6) W.Y. Liu, D.P. Steenson, M.B. Steer, "A Simple but Novel Technique of Micromachining for Millimeter Wave and Submillimeter Wave Applications, *IWMF'2000 Workshop*, Oct. 9-10, 2000.
7) W.Y. Liu, A. Harkar, D.P. Steenson, M.B.Steer, "A Novel Technique To Estimate the Voltage-Dependent Capacitance of a Weakly Nonlinear Device At Microwave Frequencies", *LCS2000*, London, September, 2000.
8) W.Y. Liu, M.B. Steer, D.P. Steenson, "Characterization of the Nonlinear Device Capacitance in Frequency Domain", *2000 International Symposium on Electron Devices for Microwave and Optoelectronic Applications*, EDMO 2000, November, 2000.
9) W.Y. Liu, D.P. Steenson, M.B. Steer, "Membrane-Supported CPW with Mounted Device", *IEEE Guided Wave Letters*, April, 2001.
10) W.Y. Liu, D.P. Steenson, M.B. Steer, "Membrane-Supported Copper Finline", *IMS2001*, May, 2001
11) W.Y. Liu, "Mass-Produced Copper-On-Polymer-Membrane Boards for Micromachined Millimeterwave Circuits", *2001 International Symposium on Electron Devices for Microwave and Optoelectronic Applications*, EDMO 2001, Nov. 2001.
12) W.Y. Liu, D.P. Steenson "Frequency-domain characterization of conductance and capacitance of Resonant Tunnelling Diode", *2001 International Symposium on Electron Devices for Microwave and Optoelectronic Applications*, EDMO 2001, Nov. 2001.
13) W.Y. Liu, D.P. Steenson, M.B. Steer, "Organic Micromachining Techniques For Mass Production of Millimeter-wave and Submillimeter-Wave Planar Circuits," submitted to and accepted by SPIE for publication in JM3, 2001

REFERENCES

[1] R.Tsu and L. Esaki, "Tunneling in a Finite Superlattice," *Applied Physics Letters*, Vol. 22, pp. 562-564, 1973

[2] Wan-Rone Liou, and Patrick Roblin, "High Frequency Simulation of Resonant Tunneling Diodes," *IEEE Transactions on Electron Devices*, Vol., 41, No. 7. July 1994.

[3] E.R. Brown, T.C. L. G. Sollner, C. D. Parker, W. D. Goodhue and Chen, "Oscillations up to 420 Ghz in GaAs/AlAs resonant Tunneling Diodes," *Appl. Phys. Lett.*, Vol. 55, no. 17, pp. 1777-1779, 1989

[4] S. Luryi, "Frequency limit of double barrier resonant tunneling oscillators," *Appl. Phys. Lett.*, Vol. 47, pp. 490–492, Sept. 1985.

[5] H. J. De Los Sanos, K. K Chui, D.H. Chow, and H.L. Dunlap, "An Efficient HBT/RTD Oscillator for Wireless Applications", *IEEE Microwave and Wireless Components Letters*, Vol. 11. No. 5, May 2001.

[6] D.H.Chow, M. Hafizi, W.E. Stanchian, J.A.Roth, J.J. Zinck, J.-J. Dubray, and H.L. Dunlap, "Monolithic integration of resonant tunneling diodes and heterojunciton bipolar transistors on patterned InP substrates, " *J. Vac. Sci. Technol. B*, Vol. 16, p. 1413, 1998.

[7] U.Auer, W. Prost, G.Janssen, M. Agethen, R. Reuter, and F. J. Tegude, "A novel 3-D integrated HFET/RTD frequency multiplier," *IEEE J. Select. Topics Quantum Electron.*, Vol.2, pp. 650-654, Sept. 1996

[8] W. Prost, U. Auer, C. Pacha, G. Janben, R. Bertenburg., W. Brockerhoff, K. Groser, and F.J.Tegude, "InP-based HFETs and RTDs for high speed digital circuitry," in *Proc. Symp. Signals, Syst., Electron.*, Pisa, Italy, 1998.

[9] P.Mazumder, S. Kulkarni, M. Bhattacharya, J.P.Sun, and G.I.Haddad, "Digital circuit applications of resonant tunneling transistors for threshold logic circuit applications," in *Proc. 9th IEEE Great Lakes Symp. VLSI*, Ann Arbor, MI. March 4-6, 1999.

[10] T.C.L.G. Sollner, W.D. Goodhue, P.E. Tannenwald, C.D. Parker, D.D.Peek, and H.W. Le, "Resonant Tunneling Through Quantum Wells up to 2.5 Thz," in Conference Digest - *8th Internation Conference on Infrared and Millimeter Waves*, 1983

[11] P. Zimmermann, "Solid-state oscillators for the THz-range," proceedings of the *8 th International Conference on Terahertz Electronis*, Darmstadt, 28-29 September 2000.

[12] P.H. Siegel, R.P. Smith, S. Martin and M. Gaidis, "2.5 THz GaAs monolithic membrane-diode mixer", *IEEE Trans. Microwave Theory and Tech.*, Vol. 47, No. 5, May 1999, pp. 596-604.

[13] Michael C. Gaidis, Herbert M. Pickett, C. D. Smith, Suzanne C. Martin, R. Peter Smith, and Peter H. Siegel, "A 2.5 THz receiver front end for spaceborne applications, " *IEEE Trans. Microwave Theory and Tech.*, Vol. 48, No. 4, April 2000, pp. 733-739.

[14] N. R. Erickson, R.P Smith, S. C. Martin, B Nakamura, and I. Mehdi, "High efficiency MMIC frequency triplers for millimeter and submillimeter wavelengths," *2000 IEEE MTT-S Int. Microwave Symp. Dig.*, Vol. 2, pp. 1003-1006, June 2000.

[15] A. Maestrini, D. Pukala, F. Maiwald, E. Schlecht, G. Chattopadhyay, and I. Mehdi, "Cryogenic operation of GaAs based multiplier chians to 400GHz," proceedings of the *8 th International Conference on Terahertz Electronis*, Darmstadt, 28-29 September 2000.

[16] F. Maiwald, S. Martin, J. Bruston, A. Maestrini, T. Crawford, I. Mehdi, and P. H. Siegel, "2.7 THz waveguide tripler using monolithic membrane diodes (MOMED)," *2001 IEEE MTT-S Int. Mic. Sym.*, Dec. 2001

[17] Suzanne Martin, Barbara Nakamura, Andy Fung, Peter Smith, Jean Bruston, Alain Maestrini, Frank Maiwald, Peter Siegel, Erich Schlecht, and Imran Mehdi , " Fabrication of 200 to 2700 GHz Multiplier Devices using GaAs and Metal Membranes", *IEEE MTT-S International Microwave Symposium*, Phoenix, Arizona, May 20-25, 2001

[18] H.C. Torrey and C.A. Whitner, "Crystall Rectifiers", *Radiation Laboratory Series*, Vol. 15, New York, McGraw Hill, 1948

[19] S.W. Moon, C.M. Mann, B.J. Maddison, I.C.E. Turcu, U. Allot, S.E. Hug, N. Lisi, "Terahertz waveguide components fabricated using a 3D X-ray microfabrication technique", *Electronics Letters*, Vol. 32, No. 19, pp-1794-1795, 12 Sept. 1996

Chapter 2: Characterization of Electrical Parameters of Resonant Tunneling Diodes

2.1 INTRODUCTION

This chapter discusses the general issues of modeling the electrical behavior of a Resonant Tunneling Device (RTD). To start with, the physical understanding of the Quantum Mechanics behind the current-voltage relationship of an RTD is first given as a preliminary introduction for the sections that follow. Concentration will be placed on the current-voltage characteristic of the double barrier resonant tunneling diode (RTD).

The simplest lumped element equivalent circuit for the RTD, which is likely to give realistic estimates for its behavior in a mixer or multiplier, is illustrated in Fig. 2.1.1. In this diagram C_j is the barrier capacitance across the barriers, R_j is the nonlinear resistance of the barriers, R_s is the series resistance of the emitter and collector due to the skin effect, substrate and back contact and C_p is the parasitic capacitance of the package (if relevant). The methodology to characterize R_j, C_j and R_s will be discussed in Section 2.5, 2.6 and 2.7, respectively. Here, the parasitic inductance and fringing capacitance of the whisker are ignored. Based upon this equivalent circuit the figure of merit normally used to evaluate the high-frequency performance potential of the double-barrier resonant tunneling diode is the cutoff frequency $F_c = 1/(2\pi R_s C_o)$ where C_o=$C_j(V=0)$ the zero-bias barrier capacitance. The cut off frequency is thus seen to define the point at which the reactance of the shunting

capacitance equals the series resistance.

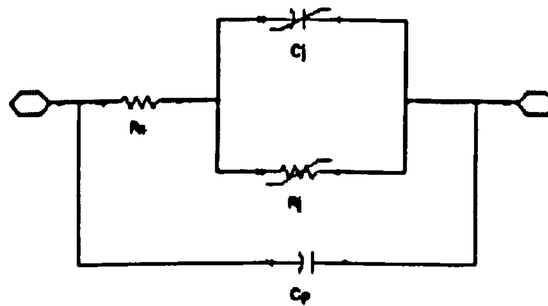

Fig. 2.1.1 Equivalent circuit of an Resonant Tunneling Diode

The electrical current through an RTD is governed by the tunneling process and the inelastic scattering process, both of which, strictly speaking, require full quantum mechanical and self-consistent calculations. However, as will be demonstrated in this chapter, characterization of the current-voltage relationship is still mathematically trivial, if the intention is only for harmonic analysis. In this regard, the scope of this chapter will not go beyond a brief outline of the known physical models that can be analytically expressed in closed form. However, this analysis provides no information which would enable an improved layer design to increase the nonlinear characteristics of the device. The analysis nevertheless points the way to what characteristic would be desirable and leaves a more physical analysis to provide the answers as to how these nonlinearities are increased or otherwise to others.

To some extent the available physical models bridge the gap between models used in circuit simulation and quantum mechanical models. As will be discussed in the next few sections, the sharp discontinuities in the modeled current-voltage characteristic appear to be excessively smoothed out when compared with actual measurements. In this regard, the quantum physics based model was primarily used here to estimate the physical device parameters, rather than

curve-fitting the measured data. Driven by the problem of obtaining an exact fit using the physics based model, we decided to employ the measurement-based characterization to derive the current-voltage characteristic of an RTD. In doing so, the current-voltage characteristic was sectionalized into multiple weakly nonlinear segments, each of which was individually curve-fit into a single polynomial for a given independent variable range. This process continued until the final set of equations fully defines the entire dc-characteristic. This set of equations was finally connected together using a chain of step functions into a closed-form expression that was later used as a behavioral model in nonlinear circuit analysis. In this chapter, the modeling technique will be demonstrated through an example. Results of simulation and measurement will be finally given to substantiate this presentation.

Following a measurement-based characterization of the current-voltage curve, this chapter additionally presents two measurement-based techniques suitable for extracting nonlinear device capacitances in the spectral domain. Characterized by its simplicity, the technique approximately resolves the capacitance-voltage characteristic using the available current-voltage characteristic and the harmonic data measured in the frequency domain. Large-signal frequency-domain characterization can be used to estimate ultra-small variation in capacitance versus voltage without running into problems related to usual small signal capacitance extraction at varying bias levels. This procedure avoids instability problems and the problem of extracting pico-farad-level capacitances using conventional capacitance meters operating at 10 MHz and 100 MHz. Experimental evidence reveals that the frequency domain technique can yield a reliable first order estimate of the capacitance-voltage characteristic.

The aim of the work described in this chapter is incorporation of as many electrical parameters in the simulation model of the RTD as possible. As will be highlighted in Section 2.2, there exists one phenomenon, the skin resistance, that cannot be directly used as a simulation model without further consideration. The skin effect represents the preferential current distribution over the surface of a conductor when the frequency becomes sufficiently high, resulting in a frequency-dependent resistance which becomes significant at or above

millimeter wave frequencies. Resistance due to skin effect at the RTD's terminals significantly reduces the effective voltage drop across the RTD at millimeter wave and submillimeter wave frequencies and more importantly decreases the cut-off frequency. For completeness, several published lumped-element models that are causal and that simulate the skin effect with reasonable accuracy are examined in Section 2.6. The result of the work presented in this chapter is a model of a Quantum Barrier Device that can be conveniently extracted from measurement and used in circuit design.

2.2 PRELIMINARY THEORY OF RTD'S

The tunnel diode was discovered in 1958 by Esaki[1]. Around one year later, the integrated circuit was invented. During this time, electrons were intuitively assumed to be classical particles responding with an effective mass to the external electrical field. The semiconductor band theory and the Fermi-Dirac statistics were the primary tools across the electronics industry in understanding the electrical behavior of a conventional device. The classical theories of semiconductor physics were somewhat akin to those of vacuum tubes.

In 1973, Tsu and Esaki showed that negative resistance could arise from finite superlattices [1]. Around one year after, Esaki et al [2] demonstrated a working model of Resonant Tunneling Diodes (RTDs). The classical picture of electrons originally employed in modeling tunnel diodes were inappropriate for explaining the electrical behavior of RTDs whose active dimensions are around a few nano-meters, i.e. a fraction of the de Broglie electron wavelength. The negative differential resistance of an RTD and the photosensitivity of the current are the example phenomena that cannot be predicted using the classical electron theory. The electronic transport mechanism of RTDs cannot be understood without incorporating the concepts of electronic tunneling and energy discretization, both of which violates the most elementary laws of classical mechanics. Within an RTD, there exists two kinds of electronic tunneling, i.e. coherent tunneling and incoherent tunneling. Coherent tunneling of electrons accounts for the negative resistance phenomenon of an RTD. But the coherent tunneling formulation given in [2] does not explain the non-zero valley current in the current-voltage characteristic. It is

believed that the large spread of electrons at the emitter at room temperature generates non-zero valley current. In general, the coherent tunneling theory coupled with the concept of electron spread suffices to model the basic current-voltage relationship of an RTD.

Fig. 2.2.1(a) depicts a schematic representing a Double Barrier Device structure of nano-meter dimensions. The emitter and the collector are made with heavily doped small bandgap semiconductor material(s), e.g. GaAs. Barrier 1 and Barrier 2 are the ultra-thin potential barriers made from materials with a relatively large bandgap, e.g. AlGaAs. Between the two barriers is the quantum well which is made from a smaller bandgap semiconductor, e.g. GaAs again. In practice, there should be an added depletion region adjacent to the double-barrier quantum well. This depletion region (not shown in Fig. 2.2.1) serves to reduce the capacitance, thus increasing the cut-off frequency. The energy profile is in general described by the bandgap structure as shown in Fig. 2.2.1(b) and is determined primarily by the materials being used for these regions.

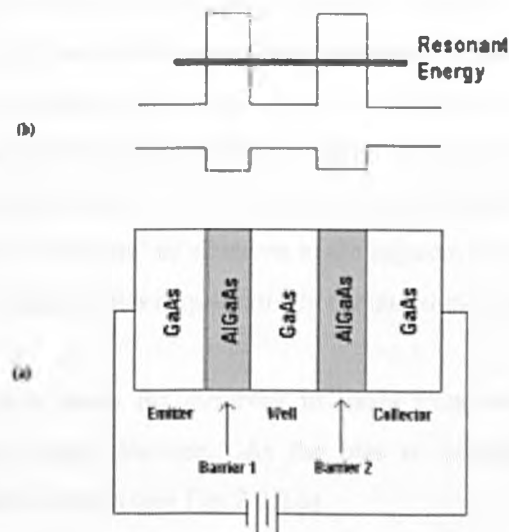

Fig. 2.2.1 (a) Basic configuration of a typical RTD, and (b) Related conduction and valence band structure

By the process of quantum mechanical tunneling, electrons energetically cross the potential barriers, yielding a tunneling current which can be discontinuous and accounts for the negative differential resistance regions in an RTD. It is well known that the tunneling current through a single potential barrier depends exponentially on the height and width of the barrier. It might seem that the electrical behavior with two barriers in series could not be much more interesting than that of a single barrier. However, if the width of the well between the two barriers is only a few nano-meters (i.e. smaller than the de Broglie electron wavelength), the current-voltage characteristic is qualitatively and quantitatively different from that of a single barrier. Indeed, the electronic behavior of the double barrier somehow is analogous to an optical fabry Periot Etalon with electron energy substituted for photon energy.

In theory, the electron energies related to the wave function inside the quantum well can only take several discrete values. However, if the quantum well is only a fraction of the de Broglie electron wavelength, there are only a few allowed energy states inside the well. These we call resonant energies. This double-barrier structure acts like a filter that allows only electrons with energy near the resonant one to be transmitted across the barriers. It is assumed that the double-barrier structure is operating at a low temperature; in which case, the thermal distribution of electrons is not dominant. When a bias is applied, the whole conduction band structure of Fig. 2.2.1(b) is modified, with a corresponding decrease in the resonant energy (see Fig. 2.2.2.a) with respect to the 'sea' of electrons in the adjacent semiconductor emitter region. The current flow under different bias is qualitatively explained as follows:

(a) The applied bias that causes the electrons to travel from the emitter to the collector modifies the conduction band structure. As the bias is increased, the conduction band decreases and the current increases (see Fig. 2.2.2.a)

(b) The current increases as the resonant energy approaches the energies of the most populated electron states in the emitter (see Fig. 2.2.2.b).

(c) When the bias increases to an extent that the resonant energy falls below the edge of the conduction band in the emitter (see Fig. 2.2.2.c), there are few electrons which can tunnel across the barriers. This results in the current dropping until it reaches a minimum value, known as the valley. The non-zero valley current is due in part to the inelastic electron scattering processes, but mainly due to electrons in the thermionic tail of the electron distribution in the emitter either passing through the next resonant state or over the top of the barriers.

(d) Finally, at high voltage bias, the thermal excitation in the RTD becomes a significant factor. The inelastic scattering effect becomes dominant over the coherent tunneling effect. Electrons pass over the barriers (see Fig. 2.2.2.d), leading to a rapid rise in current.

It should be noted that this explanation mainly applies to a low temperature condition. During resonant tunneling at room temperature, however, it is the thermal distribution of electrons in the emitter which is dominant.

In Fig. 2.2.2, the region between the peak and the valley is termed the negative differential resistance (NDR) region of the RTD. The NDR region is commonly employed as an active source in oscillator and parametric amplifier designs. The non-zero valley current due to the scattering results in dc power dissipated in dc-biasing. The difference between the peak and the valley represents the dynamic range that determines the maximum oscillating power obtainable from the device. Hence, the figures of merit for the RTD are the valley current and the ratio of the peak to the valley currents. Improvement of both magnitudes of both figures of merit of an RTD requires engineering the bandgap parameters, such as barrier dimensions, doping concentrations, etc.

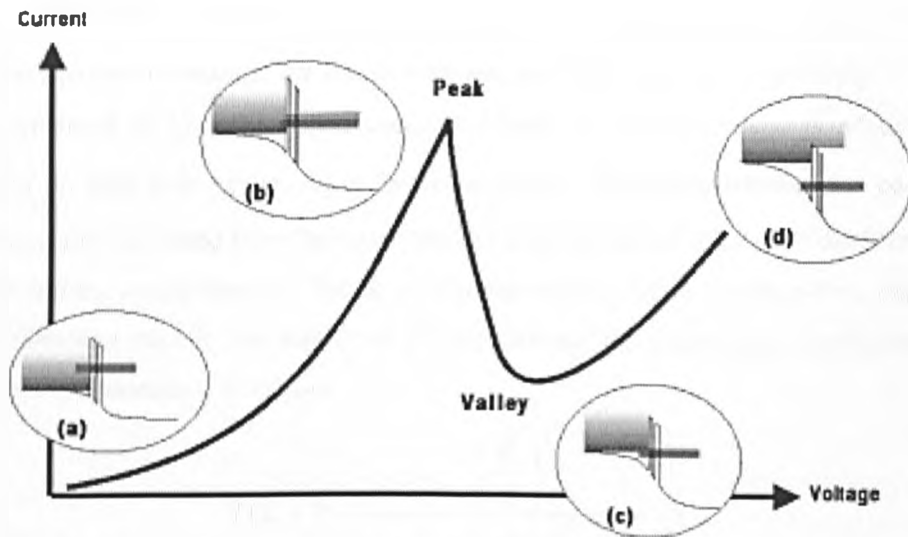

Fig. 2.2.2 Current-voltage Relationship of a Typical Double Barrier RTD.

2.3 PHYSICS BASED CHARACTERIZTION OF ELECTRICAL BEHAVIOR

2.3.1 COHERENT TUNNELING CURRENT

In this section, a published physical model that successfully expresses the current-voltage relationship in a closed-form expression is examined and expanded upon. Most of the material is extracted from Ref [6] and Ref [20]. This model is derived from the original standard formula [1] which expresses the tunneling current density $J_t(V)$ as:

$$J_t(V) = \frac{em^* k_B T}{2\pi^2 \hbar^3} \int_{E_c}^{\infty} T(E) \log \left[\frac{1 + \exp\left(\dfrac{E_F - E}{k_B T} \right)}{1 + \exp\left(\dfrac{E_r - E - qV}{k_B T} \right)} \right] dE$$

(2.3.1.1)

where e, m^*, K_B, T and $\hbar$ represent the charge of the electron, the effective electron mass, the Boltzmann constant, the temperature and the Plank constant respectively. E is the energy measured up from the emitter conduction band. E_r is resonant energy relative to the bottom of the well at its center. E_F is the Fermi energy. $T(E)$ is the transmission coefficient that is normally calculated from the wave function available in the solution of the Schrodinger equation and the supply function. But in order to analytically derive the close-form expression for the tunneling current, the authors of [6] approximate the transmission coefficient using Lorentzian approximation as follows:

$$T(E,V)=\frac{\left(\frac{W}{2}\right)^2}{\left[E-\left(E_r-\frac{eV}{2}\right)\right]^2+\left(\frac{W}{2}\right)^2}$$

(2.3.1.2)

where W is the resonance width. The Lorentzian approximation given in Equation (2.3.1.2) is based on two assumptions: 1) the width of both barriers are identical and 2) half the voltage drop falls from the emitter to the center of the well. Obviously, these assumptions are not valid if the RTD is not symmetrical, and indeed, the application of a bias disturbs this symmetry to an extent but this is considered as only a modest purtabation.

For a small resonance width W, the transmission coefficient is negligible except when E is close to resonance, i.e. $E=E_r-eV/2$. By substituting $E=E_r-eV/2$ only to the log term of Equation (2.3.1.1), we obtain the following approximation:

$$J_t(V)=\frac{em^*k_BT}{2\pi^2\hbar^3}\log\left[\frac{1+\exp\left(\frac{E_F-E_r+eV/2}{k_BT}\right)}{1+\exp\left(\frac{E_F-E_r-eV/2}{k_BT}\right)}\right]\int_{E_c}^{\infty}\frac{\left(\frac{W}{2}\right)^2}{\left[E-\left(E_r-\frac{eV}{2}\right)\right]^2+\left(\frac{W}{2}\right)^2}.dE$$

(2.3.1.3)

The solution of Equation (2.3.1.3) is:

$$J_t(V)=\frac{em^*k_BT}{2\pi^2\hbar^3}\log\left[\frac{1+\exp\left(\frac{E_F-E_r+eV/2}{k_BT}\right)}{1+\exp\left(\frac{E_F-E_r-eV/2}{k_BT}\right)}\right]\left[\frac{\pi}{2}+\tan^{-1}\left(\frac{E_r-eV/2}{\frac{W}{2}}\right)\right]$$

(2.3.1.4)

However, the Lorentzian approximation given in Equation (2.3.1.2) is only valid when the double barrier structure is fully symmetrical. To compensate the non-ideal Lorentzian approximation, the authors of [6] suggests the use of $E=E_r-eVn$, instead of $E=E_r-eV/2$. Here, eVn represents a fraction of voltage, instead of half of voltage, effectively applied from the emitter to the well. It follows from Equation (2.3.1.4) that a more general analytical description of the tunneling current against voltage can be approximated as:

$$J_t(V)=\frac{em^*k_BT}{2\pi^2\hbar^3}\log\left[\frac{1+\exp\left(\frac{E_F-E_r+eVn}{k_BT}\right)}{1+\exp\left(\frac{E_F-E_r-eVn}{k_BT}\right)}\right]\left[\frac{\pi}{2}+\tan^{-1}\left(\frac{E_r-eVn}{\frac{W}{2}}\right)\right]$$

(2.3.1.5)

Let us define the last bracketed term as $SS(V)$. That is,

$$SS(V)=\left[\frac{\pi}{2}+\tan^{-1}\left(\frac{E_r-eVn}{\frac{W}{2}}\right)\right]$$

(2.3.1.6)

Consider Fig. 2.3.1(a) and Fig. 2.3.1(b), which respectively shows a plot of $SS(V)$ and $J_t(V)$ against different resonant width W. The parameters being used in this illustration are $E_r = 0.2972eV$, $E_F = 0.17eV$ and $n = 0.5$. It is interesting to note from Fig. 2.3.1(a) that the function $SS(V)$ (or the last bracketed term of Equation (2.3.1.5)) is simply a step function with the threshold being at NDR region and with the resonant width determining the sharpness of the transition at the NDR region. On the other hand, it appears from Fig. 2.3.1 (b) that the resonant width directly determines the slope of the NDR region and the peak of the device current. At low voltage, the current-voltage relationship is largely determined by the log term of Equation (2.3.1.5). The current increases monotonically with the bias voltage until $SS(V)$ changes from 3 to zero. There is no sign that the resonant width can contribute any effect on the nonlinearity around the origin of the current-voltage characteristic (, although the position of the resonance relative to the bottom of the well will affect the position (i.e. voltage) of the resonant peak). Consistent with the theory, the resonant width plays a very important role in determining the dynamic range of the NDR region and hence the peak-to-valley ratio, which is commonly refered as the figure of merit of an RTD.

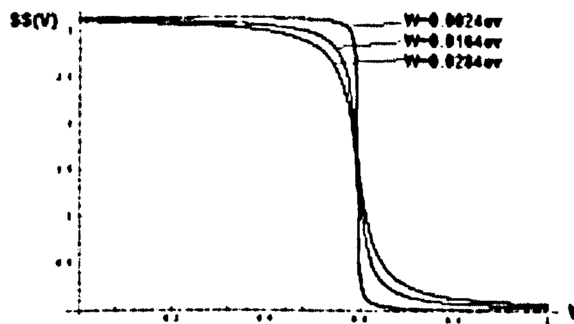

(a)

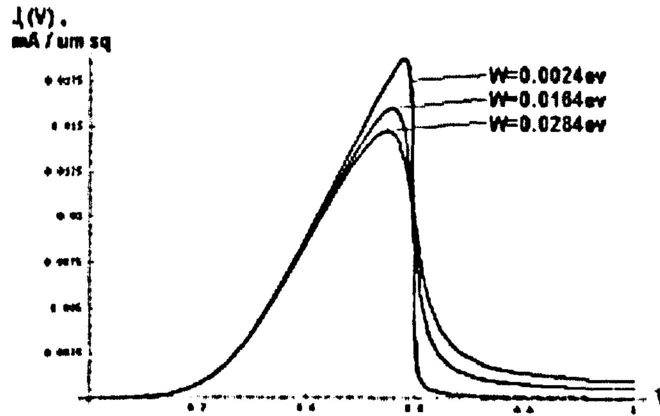

(b)

Fig. 2.3.1 (a) $SS(V)$ against different resonant width W 's. (b) $J_t(V)$ against different resonant width W 's

Consider Fig. 2.3.2, which shows a plot of $J_t(V)$ versus different E_F 's. The parameters being used in this illustration are $E_r = 0.2972eV$, $W = 0.0164eV$ and $n = 0.5$. It appears that the Fermi energy E_F can affect not only the value of the peak current, but also the nonlinearity around the origin of the current-voltage characteristic of an RTD. The Fermi energy E_F is dependent on the materials used for the double barrier structure, i.e. doping levels, temperature, and local band structure.

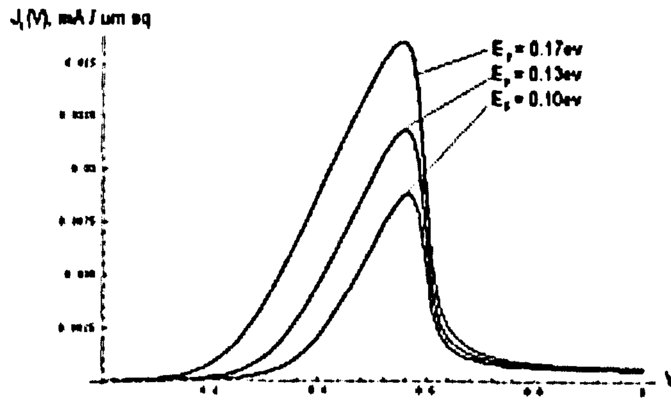

Fig. 2.3.2 Current density $J_t(V)$ against different E_F 's

2.3.2 CURRENT DUE TO INELASTIC SCATTERING

As mentioned previously, the current in an RTD consists of the coherent tunneling current, which accounts for the NDR regions of the RTD, and the incoherent tunneling current, which is believed to be caused by the inelastic scattering of electrons. Being incoherent in nature, the current due to inelastic scattering give rises to the non-zero valley current that disadvantageously makes the RTD lossy. Some published articles, including Reference [6], attempt to explain the inelastic scattering process in terms of classical mechanics, whereby an electron is perfectly defined by its position x and momentum p= Σ k. Thus, the current due to inelastic scattering is the carrier distribution function, f(x,k,T), which, at temperature T, gives the number of carriers located at the position x that have momentum p. This appears to be the reason why the authors of [6] approximated the inelastic scattering current $J_e(V)$versus voltage using the Boltzmann transport equation as follows:

$$J_e(V) = H\left(\exp\left(\frac{n_e eV}{k_B T}\right) - 1\right) \tag{2.3.2.1}$$

where H is a constant to be fit by nonlinear regression. Since the scattering current $J_e(V)$ is subject to the existence of the thermal energy in the RTD, the decrease in the temperature will modify the value of n_e of Equation (2.3.2.1), thereby suppressing both the peak current and the valley current.

However, according to one of our experiments, as illustrated by the plots in Fig. 2.3.2.1, the valley current drops as the temperature decreases, while the peak current slightly increases as the temperature increase. In other words, the peak-to-valley ratio increases as the RTD is cooled down. This result supports the findings in Ref [21], which suggests that the incoherent tunneling process (or the scattering of electrons) resizes the NDR. Thus, modeling the scattering current using the classical Boltzmann transport equation is not sufficient.

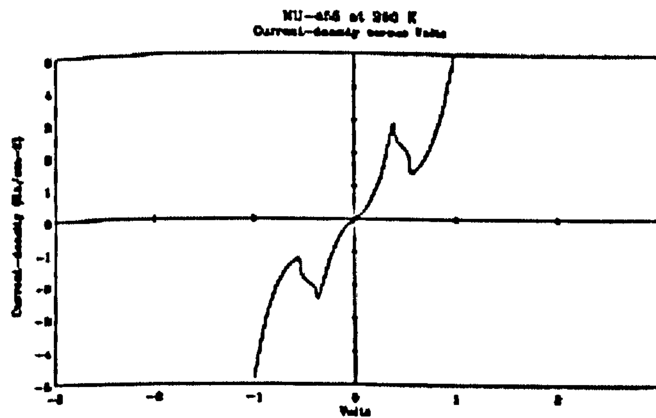

(a)

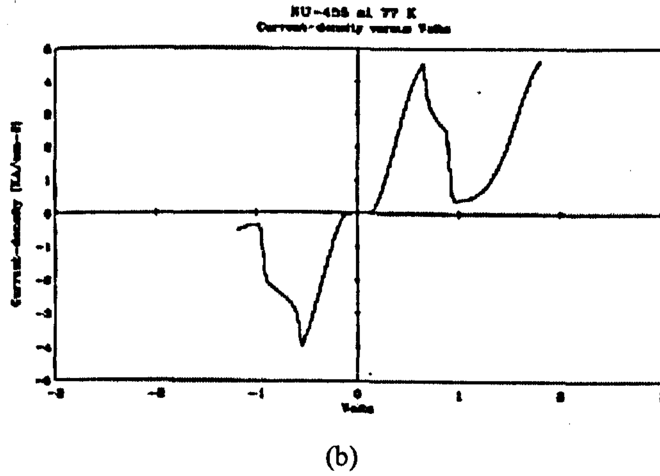

(b)

Fig. 2.3.2.1 Current-voltage relationship of a Quantum Barrier Device (a) at 290K, (b) at 77K.

2.3.3 CURRENT-VOLTAGE CHACTERISTIC OF RTD

The final expression that models the current-voltage relationship of the device is just a sum of the tunneling current and the scattering current (i.e. the tunneling current through the next higher resonant state), respectively given in Equation (2.3.1.5) and (2.3.2.1), and can be written as:

$$
\begin{aligned}
J(V) &= J_t(V) + J_e(V) \\
&= \frac{em^* k_B T}{2\pi^2 \hbar^3} \log\left[\frac{1+\exp\left(\frac{E_F - E_r + eVn}{k_B T}\right)}{1+\exp\left(\frac{E_F - E_r - eVn}{k_B T}\right)}\right]\left[\frac{\pi}{2} + \tan^{-1}\left(\frac{E_r - eVn}{\frac{W}{2}}\right)\right] + H\left(\exp\left(\frac{n_e eV}{k_B T}\right) - 1\right)
\end{aligned}
\qquad (2.3.3.1)
$$

Fig. 2.3.3 demonstrates a current-voltage relationship calculated from a real device ($E_F = 0.06eV$, $E_r = 0.08eV$, $W = 0.0012eV$, $n_1 = 0.5$, $n_2 = 0.1101$, and

$H = 0.3011mA$).

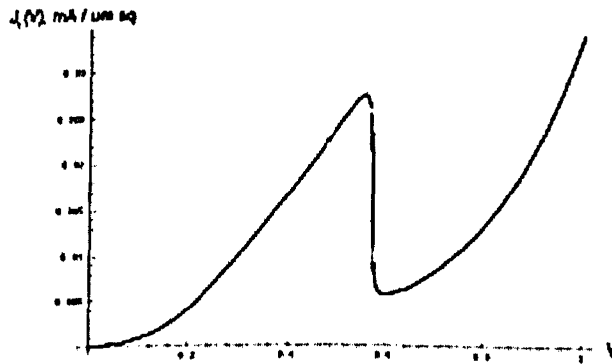

Fig. 2.3.3 Calculated current-voltage characteristic of a real RTD

2.3.4 SKIN-RESISTANCES AT THE EMITTER AND THE COLLECTOR

One of the very important aspects of this work is to investigate the high frequency behavior of a typical RTD. Apart from the current-voltage and the capacitance-voltage characteristic, the frequency domain performance of an RTD is also critically dependence on the skin-effect associated with the collector and the emitter. The collector (or the emitter) can be thought as a round wire of a finite conductivity (which is a function of the doping level). At lower frequencies, electromagnetic waves penetrate the entire cross section of a round wire to carry current. Hence, the resistance of the collector or the emitter may not be measurable, because, as the operating frequency increases, the penetration depth of the electromagnetic field into the collector (and emitter) decreases. Hence, the high frequency resistance of the collector (and emitter) increases, while the inductance decreases because of the decrease in flux in the collector (and the emitter). The impedance of an isolated round wire with current return at infinity is one of the few known analytical solutions for skin effects in two dimensions. Mathematically, the impedance is given by:

$$Z(\omega)=\frac{\zeta}{2\sigma\pi R^2}\frac{J_0(\zeta)}{J_1(\zeta)}$$

(2.3.4.1)

where R is the radius of the wire, and σ is the dc conductivity. The $J_o(\zeta)$ and $J_l(\zeta)$ respectively represents the Bessel functions of the first kind and the second kind. ζ is the nomalized frequency variable defined as follows:

$$\zeta=\exp\left(j\frac{3\pi}{4}\right)R\sqrt{\omega\mu\sigma}$$

(2.3.4.2)

The square root term is commonly recognized as the inverse of the skin depth of an infinite planar conductor. At frequencies beyond 100 Ghz, skin depth is generally not an issue for a round wire with diameter greater than one micron. But the collector (or the emitter) is ohmic semi-conductor heavily doped with n-type (or p-type) impurities, and its conductivity is nowhere near that of copper. Because of the fact that the skin resistance varies with the square root of the conductivity σ, it is important to ensure that the doping levels of the collector and the emitter are reasonably high in order to minimize the effective skin depth or that the metal contacts to be emitter and collector regions are as close as possible.

In mixer design, the parasitic conversion loss can be expected to be larger both for a small device diameter, when the skin resistance increases, and for a large device diameter when the barrier capacitance dominates. Thus the conversion loss is a function of device diameter and should be minimized for some optimum device diameters at a given frequency. At a given frequency the capacitance dominates the parasitic losses for larger diameters but when the diameter decreases below the optimum, skin losses begin to dominate and the conversion rises again. In some cases, it is better to have a device whose diameter is greater rather than smaller than optimum. It is not sufficient to simply reduce device diameter by using electron beam lithography, in order to obtain enhanced high frequency performance, without taking steps to bring high conductivity contacts as close as possible to the active regions of the device. This illustrates the design of a planar device structure with low parasitic device interconnects.

2.3.5 BARRIER CAPACITANCE OF AN RTD

The analytical treatment of the barrier capacitance taken from Ref [21] is included here for completeness. To start with, consider Fig. 2.3.5.1 which shows the band diagram of the tunneling structure and the small-signal model. Assuming that the thickness of each barrier is approximately zero, C_L and C_R, which respectively represent the capacitance measured from left barrier and the right barrier to the middle of the well are given as

$$C_L = \frac{\varepsilon_o \varepsilon_r A}{4\pi\left(d_L + \frac{d_W}{2}\right)}$$

(2.3.5.1)

and

$$C_R = \frac{\varepsilon_o \varepsilon_r A}{4\pi\left(d_R + \frac{d_W}{2} + d_{depletion}\right)}$$

(2.3.5.2)

In this approach, the quantum capacitance C_q is obtained from Luryi's definition of quantum capacitance [21], and is given without proof as follows:

$$C_Q = \sum_i \frac{\frac{m^* e^2}{\pi \hbar^2} A}{1 + \exp\left(\frac{E_i - \mu_3}{kT}\right)}$$

(2.3.5.3)

where μ_3 is the quasi-Fermi level in the well and m^* is the effective electron mass in the well. E_i is the energy level i related to the conduction band edge φ_3, so that the C_Q can be expressed as function of V_Q.

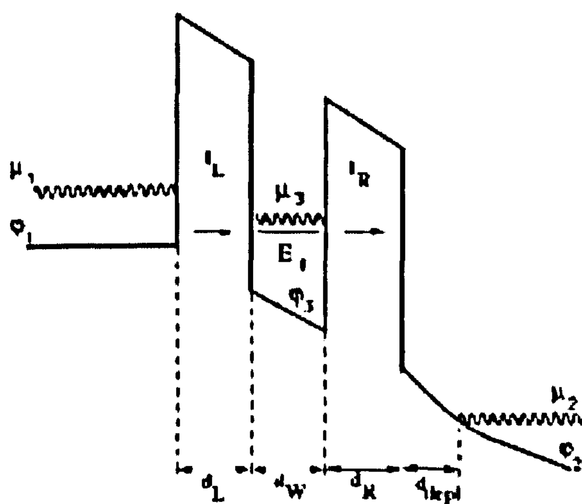

(a)

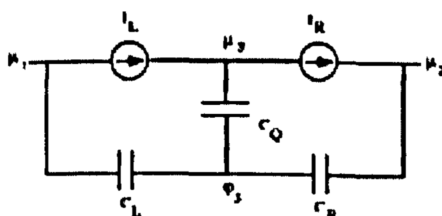

(b)

Fig. 2.3.5.1 (a) Band diagram of the tunneling structure; (b) the small-signal equivalent circuit modeling the band diagram in (a).

2.3.6 PROBLEMS OF CHACTERIZATION BASED ON THE PHYSICAL MODELS

The physics-based modeling approach is not without disadvantages. To some extent, modeling the electrical behavior at a fundamental physical level undenibly generates engineering insights

that bridge the gap between the circuit simulation model and the quantum physics. However, there remains a number of issues that cannot be resolved using the physical model given in Equations (2.3.3.1 - 2.3.4.2) . Some of these issues are listed as follows:

1. In many occasions, the peak in current-voltage characteristic appears to be over-smoothened when the NDR region becomes less abrupt (i.e. larger resonant width). The over-smoothened peak is probably due to the fact that the transmission coefficient has been inappropriately assumed to be neglibible in arriving Equation (2.3.1.3). This unavoidably leads to incorrect guess of n_l in the data-fitting process.
2. In the current-voltage characteristic, the sharpness of the peak and that of the valley are controlled by the step function $SS(V)$ given in Equation 2.3.1.6. Fig. 2.3.1 (a) suggests that this step function is anti-symmetric about the threshold voltage. This implies that the sharpness of the peak and that of the valley must be equal, as opposed to what is observed in many measured current-voltage characteristics.
3. It has been demonstrated that scattering introduces a broadening of the total transmission coefficient [20]. This broadening reduces the NDR and increases the valley current. However, scattering current in Equation (2.3.2.1) will not resize the NDR. This suggests that the Boltzmannian approximation of electronic scattering may not be appropriate and that other issues need to be considered.
4. The physical model for the skin effect given in Equation (2.3.4.2) is not readily usable as a time-domain simulation model, because of its square-root dependency of the operating frequency. In order for the skin effect to be taken into consideration during circuit simulation, it is necessary to convert the physical skin effect model into an lumped-element equivalent model with a frequency dependence. The technique to simulate skin effect will be discussed in next section.

Issue (2) can be resolved by using another more simplified model from [8], which does not employ the Lorentzian approximation as was used in Equation (2.3.1.2), thus taking care of the peak and the valley differently. The added freedom of this simplified model characterizes the

peak and valley more accurately in the current-voltage characteristic, although the final expression yields less physical insight. For readers' convenience, the tunneling current density is analytically given without proof as follows:

$$I(V) = C_1 V^i \{\tan^{-1}[C_s(V - V_T)] - \tan^{-1}[C_2(V - V_N)]\} + C_3 V^j + C_4 V^k \tag{2.3.6.1}$$

where C_1, C_2, C_3 and C_4 are the numerical constants to be obtained by curve fitting. i, j and k are integer exponents ≥ 2. V_T is the threshold voltage, and V_N is the voltage of the steepest part of the NDR region. The last two terms of Equation (2.3.6.1) are used to model the incoherent valley current due to inelastic scattering of electrons, while the first term represents the tunneling current in the RTD.

2.4 MEASUREMENT BASED CHARACTERIZATION OF CURRENT-VOLTAGE RELATIONSHIP OF RTD

In spite of numerous efforts to develop analytical models during the last few decades, accurately predicting the current-voltage characteristic of RTDs remains a formidable task. One obvious reason, as mentioned previously, is that the existing quantum mechanically based models fail to characterize accurately the sharp discontinuities along the current-voltage characteristic. On the other hand, a device characteristic such as this cannot not be accurately modeled using conventional curve-fitting algorithms, including polynomial regression, spline, etc. Few published articles on modeling of Resonant Tunneling Diodes address the nonlinear effects associated with such sharp discontinuities. Failure to model the sharp discontinuity in a device characteristic implies a failure to model the sub-threshold current in the NDR regions, also leading to potential inaccurate frequency domain simulations.

Nevertheless, no matter how abrupt the transitions in the device characteristic are, the device characteristic can still be split into multiple weakly nonlinear segments. Each of these

segments can then be either empirically fitted to the appropriate physical models or curve-fitted using conventional regression algorithms. This process continues until we end up with a complete set of equations defining every aspect of the dc behavior. All these disconnected equations are finally connected together using a chain of continuity functions. In doing so, the whole electrical behavior of the device can be accurately modeled into a closed-form expression. In the sections that follow, the said technique of modeling is first demonstrated through an example. Results of simulation and measurement are finally given to substantiate this presentation.

2.4.1 CONTINUITY FUNCTIONS

Continuity functions have been widely used in modeling pinch-off potential of FET devices [12, 13]. The most commonly used continuity function is the one in Log-form [12, 13]. This kind of continuity function is infinitely differentiable and avoids the discontinuity in high-order derivatives that is typical of implementations using conditional functions. It was claimed in Ref [12] and Ref [13] that the smoothing nature of the Log-form continuity function "improve" convergence in circuit simulations.

However, as we will see later, the Log-form continuity function constantly suffers from convergence failures in simulating an overly sharpened discontinuity. Perhaps, quantum physicists, whose chief concern is explanation of the current-voltage characteristic using physical parameters, rarely consider these problems. As such, the commonly known issues associated with the continuity-function-based modeling technique are first outlined. But rather than repeating the previous work, this section suggests a newer approach: using step functions to smooth out the sharp discontinuity in an equally effective manner, but with better convergence handling capability in circuit simulation.

2.4.2 LOG-BASED CONTINUITY FUNCTION

There are many versions of continuity function for device modeling, the most common of which is perhaps the log-based version [12, 13] taking the following form:

$$I = \ln\left(\frac{\left(1+\exp\left(\frac{I_1 - I_2}{k}\right)\right)^{I_1}}{\left(1+\exp\left(\frac{I_2 - I_1}{k}\right)\right)^{I_2}}\right)^{\frac{k}{I_1 - I_2}}$$

(2.4.2.1)

where I is the function representing the device current. I_1 and I_2 are two different regional current functions having the following definitions:

$$I = \begin{cases} I_1 & \text{,if } I_1 < I_2 \\ I_2 & \text{,if } I_1 > I_2 \end{cases}$$

k is a smoothing factor that can be employed to adjust the sharpness of the transition between I_1 and I_2. Given that k is sufficiently small in magnitude, I of Equation (2.4.2.1) will converge to I_1 if $I_1 > I_2$, or vice versa. Equation (2.4.2.1) can potentially give rise to the numerical risks when $I_1 = I_2$. To avoid this problem, Equation (2.4.2.1) is further simplied, leading to the following expression:-

$$I = k\ln\left(\exp\left(\frac{I_1}{k}\right) + \exp\left(\frac{I_2}{k}\right)\right)$$

(2.4.2.2)

In theory, Equation (2.4.2.2) is valid for over the entire independent variable range. Knowledge of the exact intersection point when $I_1 = I_2$ is not necessary.

However, the continuity function used in Equation (2.4.2.2) is not without disadvantages.

First, modeling a single transition between I_1 and I_2 is not possible when I_1 and I_2 have multiple crossings with each other. To resolve this problem, the exact intersection point between I_1 and I_2 needs to be contained in the continuity function. Second, because of the floating point handling nature of most UNIX platforms, the exponential arguments must be restricted to the range ± 700. The simulation model employing Equation (2.4.2.2) constantly fails to behave as expected when the argument of any exponential function unrealistically goes beyond this range. This limit introduces a number of convergence problems in circuit simulation. In performing Agilent's ADS harmonic balance simulation with device models using Equation (2.4.2.2), for instance, the magnitude of k must be larger than 0.05 to avoid the infamous "arc-length continuation" problem. The only solution to this problem is to keep the value of k within the hardware-dependent thresholds. This implies a significant sacrifice of accuracy in modeling the sub-threshold current, i.e. the current at the transition between I_1 and I_2. Third, the log/exp arrangements in Equation (2.4.2.2) reduce the degree of freedom in algebraic manipulation. Hence, it is not easy to analyse intermodulation products using Equation (2.4.2.2).

2.4.3 STEP FUNCTION APPROACH

In order to characterize a strongly nonlinear characteristic without running into the problems as encountered in "Log-based" continuity function, one solution is to smooth out each abrupt transition in the characteristic using a step function that is without the log operator, i.e. Log-less step function [26]. Two functions, I_r and I_{r+1}, can be joined together using a step function in the following form,

$$I = I_r + \frac{(I_{r+1} - I_r)}{1 + \exp\left(\frac{V_r - V}{k}\right)} \tag{2.4.3.1}$$

where $V=V_r$ represents the exact voltage at which I_r and I_{r+1} cross each other. k is a positive

parameter that adjusts the sharpness of the transition at $V=V_r$. Equation (2.4.3.1) is equivalent to the following expression:

$$I=\begin{cases} I_r & ,\text{if } V<V_r \\ (I_r+I_{r+1}))/2 & ,\text{if } V=V_r \\ I_{r+1} & ,\text{if } V>V_r \end{cases}$$

(2.4.3.2)

Hence, to model an I-V characteristic with more than one discontinuous transition along the current-voltage characteristic, one can simply generalize the Equation (2.4.3.1) into the following algorithm:

$$I=I_0+\sum_{r=0}^{N}\frac{(I_{r+1}-I_r)}{1+\exp\left(\frac{V_r-V}{k}\right)}$$

(2.4.3.3)

where I and V represent the current and voltage respectively. V_r stands for the exact voltage at which the current segments I_{r+1} and I_r intersect.

Similar to the Log-based continuity function demonstrated in Equation (2.4.3.1), the step function approach can smooth the high order discontinuity equally well. On the other hand, the exponential terms in Equation (2.4.3.3) can be approximated into a power series, thus enabling the whole equation (Equation (2.4.3.3) to be expanded into a chain of rational functions. More importantly, the value of k in Equation (2.4.3.3) can go below 0.001 without running into convergence problems commonly encountered in circuit simulations with the models using the Log-based continuity functions.

2.4.4 DEMONSTRATION OF MODELING OF NONLINEAR CONDUCTANCE OF

LEEDS UNIVERSITY LIBRARY

RESONANT TUNNELING DIODE

The Resonant Tunneling Diode is an example of a nonlinear device with multiple sharp discontinuous transitions in the current-voltage characteristic that cannot be accurately modeled using conventional curve-fitting techniques. In order for the device characteristic to be modeled with the proposed technique, an algorithm was written to detect the sharp transitions in the data trace. In doing so, the whole characteristic is split into multiple weakly nonlinear sections. In this example, five sections have been allocated: Section 1, 2, 3, 4, and 5 (see Fig. 2.4.4.1). Each of these weakly nonlinear sections is then curve-fitted by polynomial regression, until the current function is well defined over the entire independent variable range. Finally, the whole set of disconnected equations is linked together using either log-based continuity function or log-less continuity function, ending up with a single analytical equation.

Using conventional polynomial regression technique, the regional current functions (I_1, I_2, I_3, I_4 and I_5) were obtained. I_1, I_2, I_3, I_4 and I_5, each respectively representing the curve-fit current of Section 1, 2, 3, 4 and 5, are given as follows:

$$
\begin{aligned}
I_1 &= -4.49187 - 12.4345*V - 13.2851*V^2 - 3.19277*V^3 \\
I_2 &= -5842.52 - 29728.4*V - 50436.8*V^2 - 28522.2*V^3 \\
I_3 &= 1.90923*V + 0.174362*V^2 + 17.4281*V^3 - 1.92381*V^4 - 36.4341*V^5 + 24.3843*V^7 \\
I_4 &= 338.451 - 1678.22*V + 2789.19*V^2 - 1547.23*V^3 \\
I_5 &= 2.73998 - 6.37916*V + 5.75243*V^2 - 0.15346*V^3
\end{aligned}
\tag{2.4.4.1}
$$

i) Model Based on Log-based Continuity Function:

Equation (2.4.4.1) represents the modeled I-V characteristic using the following log-based continuity function to connect five sections:

$$I = -k\ln\left(\frac{\dfrac{1}{\exp\left(\dfrac{I_4}{k}\right)+\exp\left(\dfrac{I_5}{k}\right)}+}{\dfrac{1}{\dfrac{1}{\exp\left(-\dfrac{I_1}{k}\right)+\exp\left(-\dfrac{I_2}{k}\right)}+\exp\left(\dfrac{I_3}{k}\right)}}\right)$$

(2.4.4.2)

ii) Model Based on Step Functions:

Equation (2.4.4.3) illustrates the I-V characteristic modeled using step functions. Here, the current $I_g(V)$ is expressed in mA:

$$I_g(V) = I_1 + \frac{I_2}{1+\exp\left(\frac{V_2 - V}{k}\right)} + \frac{I_3}{1+\exp\left(\frac{V_3 - V}{k}\right)} + \ldots \frac{I_5}{1+\exp\left(\frac{V_5 - V}{k}\right)}$$

(2.4.4.3)

where I_1, I_2, I_3, I_4 and I_5 are given in Equation (2.4.4.1) and V_1, V_2, V_3, *and* V_4 are defined as follows:-

$$V_1 = -0.62$$
$$V_2 = -0.57$$
$$V_3 = +0.57$$
$$V_4 = +0.62$$

Fig. 2.4.4.1 depicts the modeled I-V characteristic using Equation (2.4.4.3), where the value of k is limited to 0.005. The model represented by Equation (2.4.4.2) is not graphically shown, because it was found to be numerically coincident with that represented by Equation (2.4.4.3). No large numerical difference is observed between these two approaches. The modeled I-V

characteristic and the measured data have been compared and a plot of relative current error against voltage is shown in Fig. 2.4.4.2. It can be seen from Fig. 2.4.4.2 that the sharp transitions at Section 2 and Section 4 have been accurately modeled.

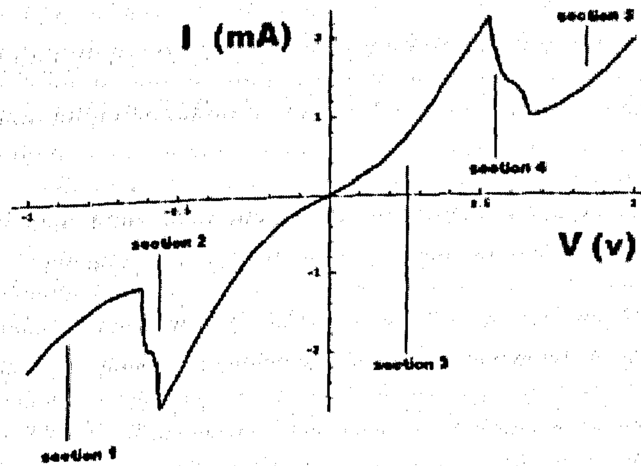

Fig. 2.4.4.1 Modeled I-V characteristic of the RTD, obtained from Equation 2.4.4.3.

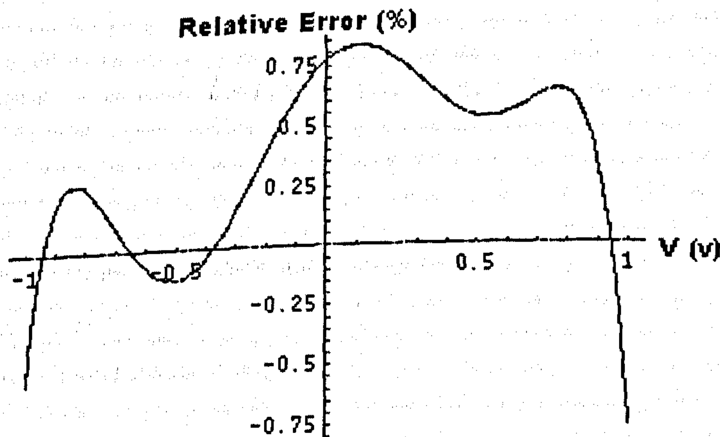

Fig. 2.4.4.2 Relative discrepancies (in percent) between the modeled IV characteristic and that measured.

It should be noted that the plateau in the sections of Section 4 and Section 2 are not real,

and result from low frequency oscillations in the devices and circuit that modify the instantaneous bias point.

2.4.5 HARMONIC CONTENTS RESULTING FROM THE SHARP DISCONTINUITIES IN THE I-V CHARACTERISTIC

As mentioned previously, sharp transitions in the characteristic can be smoothed out using log-based continuity functions or step functions. The step function approach can be algebraically simplified and hence facilitates hand-analysis of nonlinear distortion as a result of the discontinuities in the current-voltage characteristic. In this section, single tone analysis for one discontinuous transition is first developed so as to obtain a formula expressing the harmonic content.

As discussed previously, the continuity function that converts two dissimilar current functions , I_r and I_{r+1}, into a single closed form expression takes the following form,

$$I = I_r + \frac{(I_{r+1} - I_r)}{1 + \exp\left(\frac{V_r - V}{k}\right)}$$

(2.4.5.1)

where $V=V_r$ is the exact location in which the functions I_r and I_{r+1} transition and k is a positive parameter that determines the sharpness of the transition at $V=V_r$. In general, the smaller the magnitude of k, the sharper the transition is.

The nonlinear voltage, V, in Equation (2.4.5.1) can be regarded as a linear sum of multiple harmonics:

$$V = \sum_{m=-N}^{N} V_m \exp(j\omega_m t)$$

(2.4.5.2)

with a result that Equation (2.4.5.1) can be rewritten as:

$$I = I_r + \frac{(I_{r+1} - I_r)}{1 + K\exp\left(\frac{-\sum_{m=-N}^{N} V_m \exp(j\omega_m t)}{k}\right)}$$

(2.4.5.3)

where $K = \exp\left(\frac{V_r}{k}\right)$.

By direct inspection of Equation of (2.4.5.3), the increase in the value of V_r will lead to greater dependency of the current function I upon I_{r+1}. Given that a nonlinear device is used as a mixing device, the value of V_r should be minimized if I_{r+1} favours nonlinear mixing more than I_r. By way of example, if the I-V characteristic of an unbiased quantum barrier device is very weakly nonlinear around the origin, efficient subharmonic mixing cannot be attained when the voltage swing across the device fails to cover the NDR regions. In such a situation, it is advantageous to have the NDR regions drawn as close to the current axis as possible. This can be achieved by either application of a suitable bias to the device when using the device as a mixer or increasing the well width coupled with a suitable layer profile when designing the device.

The role of k in Equation 2.4.5.1 is to determine the sharpness of the transition between I_r and I_{r+1}. Equivalently, the sharpness of the transition between I_r and I_{r+1} can be fully expressed using the following Equation:

$$I = I_r + \frac{(I_{r+1} - I_r)}{\left(1 + \exp\left(\frac{V_r - V}{k'}\right)\right)^n}$$

(2.4.5.4)

In Equation (2.4.5.4), the sharpness of the transition between I_r and I_{r+1} is to be determined by the value of n. The increase in n will similarly lead to a sharper transition between I_r and I_{r+1}. The main difference between Equation (2.4.5.4) and Equation (2.4.5.1) lies in the value of I when $V = V_r$. That is, substituting $V = V_r$ gives $I = (I_{r+1} + I_r)/2$ in Equation (2.4.5.1) and $I = I_r + (I_{r+1} - I_r)/2^n$ in Equation (2.4.5.4).

Suppose, by substitution of Equation (2.4.5.2) into Equation (2.4.5.4), we have:

$$\frac{1}{\left(1+\exp\left(\frac{V_r - V}{k'}\right)\right)} = \sum_{m=-M}^{M} A_m \exp(jm\omega t) \tag{2.4.5.5}$$

Then, the current function of (2.4.5.4) can be rewritten as:

$$I = I_r + (I_{r+1} - I_r)\left(\sum_{m=-M}^{M} A_m \exp(jm\omega t)\right)^n \tag{2.4.5.6}$$

Obviously, the sharper the transition between I_r and I_{r+1}, as reflected by smaller value of k in Equation (2.4.5.1) or larger magnitude of n in Equation (2.4.5.4), leads to larger higher order harmonics.

The analysis in this section can be concluded by the following observations:

a) The total harmonic content of the current is the sum of the harmonics resulting from each transition taken one at a time;
b) The threshold voltage that divides two current functions determines which of these current functions is going to play a dominant role in the nonlinear operation. In the case of quantum barrier mixer under an unbiased condition, the voltage at which the current peaks can be considered as the threshold voltage that divides the nonlinearities around the origin and the NDR region. Under an unbiased condition, the mixing behavior of a quantum

barrier device depends not only on the nonlinearities around the origin but also the nonlinearities of the NDR regions. If the nonlinearities around the origin of the characteristic is too weak, the well width should be optimized in a way that the NDR regions in the current-voltage characteristic be drawn closer to the current axis; and

c) The sharper each transition along the current-voltage characteristic leads to larger higher order harmonics;

2.5 MEASUREMENT BASED CAPACITACE CHARACTERIZATION OF NONLINEAR DEVICE IN FREQUENCY DOMAIN

The nonlinear capacitance of a device can critically affect system performance at microwave frequencies and above. For example, a non-crynogenic nonlinear device with a zero-biased capacitance of 1 pF will not be operational in frequencies at W-band or above in the absence of any bias or tuning. Knowledge of the capacitance-versus-voltage characteristic of a device can help in understanding the correct bias voltage that makes the device functional at certain frequencies. The particular focus of this section is the capacitance characterization of a device with very low capacitance.

The frequency dependent behavior of the device is normally characterized as a nonlinear capacitance or nonlinear inductance connected in parallel with the nonlinear conductance. Rough measurement of capacitance-versus-voltage characteristic can be conducted with a commercial C-V meter at a frequency below 1 Ghz. In most situations, however, the zero-biased capacitance can be no more than a few hundred femto-farads. Conventional C-V meters are capable of accurately measuring capacitances down to 10 fF – but not if there is a large conductance in parallel. Hence, data obtained from the C-V meter will not yield any reliable model for high frequency circuit analysis.

One solution is to use a vector network analyzer (VNA) to perform measurements on a device that is mounted in an appropriate fixture and under different bias conditions. The

parasitics attached to the device terminals are first isolated using standard de-embedding technique. The capacitance of the device is then extracted from the measured S-parameters. VNA measurement is well-known for its accuracy. But some devices, such as resonant tunneling diodes, can self-oscillate across the whole frequency spectrum when the device is biased to certain conditions, presenting instability to the VNA. For this category of devices, the resulting capacitance as extracted from VNA measurement may appear non-physical if the device is at resonance. This phenomenon is particularly troublesome if the device has a very high-Q factor. There are two main techniques to compensate for these measurement based artifacts:

1) simply use the data either side of the oscillation to refine the model in ADS; and

2) By using a junction with a deliberate resistance in parallel with the junction which can be thoroughly characterized at high frequencies and then removed later during the modeling stage – this approach is similar to what many people did at low frequency but more care must be taken to characterize this component at millimeter wave frequencies.

The purpose of this section is to propose a technique that yields a first order estimate of the voltage-dependent capacitance without running into instrument-specific problems as encountered in VNA measurement. While the proposed methodology does not serve to replace the traditional VNA measurement technique, it is recommended as a tool to estimate certain behavioral effects due to the voltage dependent capacitance. The proposed method of solution is based on the theories discussed in [23, 24, 25] for calculating the steady-state frequency response of nonlinear systems, but here the technology is used to develop an extraction technique for nonlinear capacitance modeling which is applicable to devices with very small capacitance. Unlike the traditional approach, which uses direct capacitance measurement at various bias voltages, the proposed technique [9] generates a large signal model for the device capacitance directly from the harmonic distribution and the known I-V characteristic. Experimental characterization of a highly abrupt device is used to demonstrate the procedures.

2.5.1 METHOD OF SOLUTIONS

Fig. 2.6.2.1 illustrates the experimental setup used for extracting nonlinear device capacitance. The nonlinear device is excited by a single tone signal V_s through the source impedance R_s=50 ohm and the transmission line TL1. Multiple harmonics generated by the nonlinear device DUT are distributed through TL1 and TL2, both of which are short in electrical length and therefore assumed to be identical. Extraction of the nonlinear device capacitance is based on the voltage harmonics across R_{Load} using a transition analyzer. The process of capacitance extraction involves two steps: A) de-embedding the linear elements using first-order approximation; B) resolving the nonlinearity of the device with the given harmonic voltages and currents. What follows is an analytical description of these two steps.

2.5.1.1 De-embedding the linear elements by first-order approximation:

From Fig. 2.6.2.1, the n-th harmonic of the device current and voltage phasors can be respectively expressed as follows:

$$I_{d,n} = \left(-I_{out,n}\cos(\beta l_2) + I_{in,n}\cos(\beta l_1)\right) + j\left(\frac{V_{out,n}\sin(\beta l_2)}{Z_2} + \frac{V_{in,n}\sin(\beta l_1)}{Z_1}\right) \tag{2.5.1.1}$$

and

$$V_{d,n} = V_{out,n}\cos(\beta l_2) - jZI_{out,n}\sin(\beta l_2) \tag{2.5.1.2}$$

The index n indicates the harmonic number. Since both arms of the T-junction connecting to the device are very short and roughly identical, it is reasonable to assume that $l_1 = l_2 = l$ and $Z_1 = Z_2 = Z$. Equation (2.5.1.1) and (2.5.1.2) can be rewritten as:

$$I_{d,n} = \left(I_{in,n} - I_{out,n}\right)\cos(\beta l) + j\left(V_{out,n} - V_{in,n}\right)\frac{\sin(\beta l)}{Z}$$

(2.5.1.3)

and

$$V_{d,n} = V_{out,n} \cos(\beta l) - jZI_{out,n} \sin(\beta l)$$

(2.5.1.4)

Equation (2.5.1.3) and (2.5.1.4) respectively represents device current and voltage for the n-th harmonic. If the device is operating in a quasi-linear or weakly nonlinear region, its nonlinear conductive current and capacitance can be respectively approximated using Taylor expansion as

$$I_g(t) = \sum_{k=0}^{\infty} a_k V(t)^k$$

(2.5.1.5)

and

$$C_d(t) = \sum_{k=0}^{\infty} C_k V(t)^k$$

(2.5.1.6)

where $V(t)$ is the time-domain voltage across the device. When the device is weakly excited to such an extent that only the fundamental component is observable at the output, all the higher order nonlinear effects can be ignored without significantly sacrificing accuracy. In such a situation, the intrinsic conductance of the device can be approximated to the first order as:

$$I_d(t) \approx a_0 + a_1 V(t)$$

(2.5.1.7)

Similarly, the voltage-dependent capacitance is virtually constant at C_0 when the voltage across the device is sufficiently small.

$$C(t) \approx C_0$$

(2.5.1.8)

Assuming that the zero-bias current is negligible, i.e. a_0=0, with $I_d(t)$ of Equation (2.5.1.7) being roughly equal to a_1 $V(t)$, the overall embedding impedance of the device at the fundamental becomes:

$$\frac{V_{d,1}(\omega)}{I_{d,1}(\omega)} = \frac{1}{a_1 + j\omega C_0} + R_p + j\omega L_p$$

(2.5.1.9)

$V_{d,1}$ and $I_{d,1}$ of Equation (2.5.1.9) respectively represent the fundamental device voltage and current in the frequency domain and, with the help of Equation (2.5.1.3) and (2.5.1.4), can be obtained from the measured values of V_{out} and I_{out}. C_0 of Equation (2.5.1.9) represents a combination of zero-bias capacitance of the device and the stray parasitic capacitance due to imperfect bonding. Equation (2.5.1.9) has four unknown variables (a_1, C_0, R_p and L_p) that needs at least four equations (i.e. four frequency points) to resolve.

In the analysis which follows, it is assumed that all the parasitic elements, such as the lead inductance and resistance, have been taken care using Equation (2.5.1.9), meaning that the $V_{d,n}$ and $I_{d,n}$ are readily available for all n 's.

2.5.1.2 Resolving the nonlinearity of the device in Frequency domain

To start with, it is assumed that the frequency-independent resistive current of the device are given as follows:

$$I_g(V) = G(V)$$

(2.5.1.10)

where $G(V)$ stands for the I-V characteristic which may or may not be expressible in power series. Knowledge of the frequency-domain behavior necessitates a conversion of $G(V)$ from

the dc to the time domain, i.e. from $G(V)$ to $G(V(t))$, and from the time- to the frequency-domain, i.e. from $G(V(t))$ to a summation of sinusoids.

Assuming that, by de-embedding the network of Fig. 2.6.1.1 using the technique described previously, the measurements read at the load leads to the following equations expressing the device voltage in the time-domain:

$$V(t)=\sum_{n=1}^{N} V_{d,n}\cos(n\omega t+\psi_n)$$

(2.5.1.11a)

$$I(t)=\sum_{n=1}^{N} I_{d,n}\cos(n\omega t+\lambda_n)$$

(2.5.1.11b)

The resistive current, as shown in Fig. 2.6.1.1, can be obtained by substituting Equation (2.5.1.11a) into Equation (2.5.1.10), which gives:

$$I_g(t)=I_g(V(t))=G\left(\sum_{n=1}^{N} V_{d,n}\cos(n\omega t+\varphi_n)\right)$$

(2.5.1.12)

The I-V characteristic, $G(V)$, may be smooth and continuous in dc-domain, in which case both the voltage-dependent conductance and capacitance can be expanded into power series using Taylor explanation, i.e. Equation (2.5.1.5a) and (2.5.1.5b). Frequency-domain expression can then be obtained by rigorous algebraic expansion. But most microwave devices are highly

nonlinear with sharp discontinuities along their characteristic. The I-V characteristic with sharp discontinuities may either be expressed approximately as a rational function [1] or accurately in a chain of continuity functions. Direct algebraic manipulation to the I-V characteristic as such is technically not practical. To be able to manipulate in frequency domain, it is necessary to apply Fourier Series Decomposition, or the like, to resolve the time domain equivalence of Equation (2.5.1.10) into a running summation of sinusoids or cosinusoids or a combination of both. In the sections that follow both techniques (i.e. rigorous algebraic expansion and by Fourier Series Decomposition) are analytically derived to obtain voltage-dependent capacitance.

2.5.1.2.a) Fourier Series Decomposition

Fourier-Series Decomposition is a common method of converting from time- to the frequency-domain for most situations. The Fourier-based techniques are robust and suited to most strongly nonlinear problems. In Fourier Series Decomposition, the continuous current waveform as given in Equation (2.5.1.12) is first converted into a chain of weighted discrete impulses by direct sampling over a complete fundamental cycle, i.e. $I_g(\omega t)$ is to be evenly sampled over ωt = 0 to π. Each impulse then undergoes a Fast Fourier Transform. Mathematically, the Fast Fourier Transform of the n th sample is expressed as:

$$F\{I_g(n\Delta t)\} = I(n\Delta t)\sum_{n=0}^{n_e/2} b_n \sin\left(n\omega(t - \psi_n) + \frac{\pi}{2}\right) \tag{2.5.1.11}$$

where n_e is the total number of the samples, Δt is the sampling period, and:

$$b_0 = b_{n_e/2} = \frac{1}{n_e} \text{ ; and } b_1 \ldots\ldots b_{n_e/2-1} = \frac{2}{n_e} \tag{2.5.1.12}$$

Then, the Fourier Series expressing $I_g(t)$ is simply the sum of the Fourier Transforms of all the samples over a complete cycle:

$$\begin{aligned} I_g(\omega t) &= \sum_{n=0}^{N} F\{I_g(n\Delta t)\} \\ &= \sum_{n=0}^{N} \left\{ I(n\Delta t) \sum_{n=0}^{ne/2} b_n \sin\left(\frac{nf_e}{ne} (t - \psi_n) + \frac{\pi}{2} \right) \right\} \\ &= \sum_{n=0}^{N} I_{d,n}(\omega t) \end{aligned}$$

(2.5.1.13)

Equation (2.5.1.9b) and Equation (2.5.1.13) respectively give the total device current and the resistive current in time domain. Then, the net reactive current as a result of the intrinsic nonlinear capacitance becomes:

$$I_c(t) = \sum_{n=0}^{M} I_{d,n}(\omega t) - I_{g,n}(\omega t)$$

(2.5.1.12a)

Noting that the reactive current as given in Equation (2.5.1.12a) is also a time derivative of charge accumulated in the device:

$$\frac{d}{dt}(CV(t)) = I_c(t) = \sum_{n=0}^{M} I_{d,n}(\omega t) - I_{g,n}(\omega t)$$

(2.5.1.12b)

, the voltage dependent capacitance can be numerically resolved using either: -

$$C = \frac{1}{\omega V} \int_0^t \left(\sum_{n=0}^{M} I_{d,n}(\omega) - I_{g,n}(\omega) \right) dt$$

(2.5.1.13a)

, or equivalently,

$$C = \frac{1}{\omega V}\int_0^V \frac{\left(\sum_{n=0}^{M} I_{d,n}(\omega) - I_{g,n}(\omega)\right)}{\frac{dV(t)}{dt}} dV$$

(2.5.1.13b)

The integral of Equation (2.5.1.13a) is in time-domain, while the end result is required to be in dc-domain. Similarly, the integrand of Equation (2.5.1.13b) is in time-domain, whereas the integral is to be evaluated in dc-domain. The integral of Equation (2.5.1.13a) or the integrand of (2.5.1.13b) needs to be adaptively sampled in the time-domain from $\omega t = 0$ to $\omega t = \pi$ and converted into the dc-domain, with the variable t removed from Equation (2.5.1.1.3a) or Equation (2.5.1.13b).

2.5.1.2.b) Rigorous Algebraic Expansion.

Rigorous algebraic expansion, though simple, is not suitable for an I-V or the C-V characteristic which contains abrupt discontinuities. However, for a weakly nonlinear cases, Rigorous Algebraic Expansion offers an easier solution to the harmonic-matching problem. It is first assumed that the current and the capacitance can be characterized into a power series, as given in Equation (2.5.1.5). Then, by summing the resistive part and the reactive part independently, the total device current becomes:

$$I_d(t) = \sum_{k=0}^{\infty} a_k V(t)^k + \frac{d}{dt}\left(V(t)\sum_{k=0}^{\infty} c_k V(t)^k\right)$$

(2.5.1.14)

With some algebraic rearrangements, Equation (2.5.1.14) can be rewritten as:

$$I_d(t) = \sum_{k=0}^{\infty}\left(a_k + (k+1)C_k \frac{dV(t)}{dt}\right)V(t)^k$$

(2.5.1.15)

The time-domain voltage across the device, as given in Equation (2.5.1.11a), is then converted into exponential form, that is:

$$V(t) = \sum_{n=0}^{N} V_n \exp(jn\omega t)$$

(2.5.1.16)

where V_n represents the phasor for the n th harmonic and is of the following complex quantity:

$$V_n = \frac{V_{d,n}\exp(j\psi_n t)}{2}.$$

Each $V(t)^k$ term of Equation (2.5.1.15) is then flattened into the following form:

$$V(t)^k = \sum_{n=-kN}^{kN} A_{k,n} \exp(jn\omega t)$$

(2.5.1.17)

where the coefficients $A_{k,n}$ for all n's are numerically resolved using the following algorithm: -

for (r=1; r<=N; r++)

*for (i=-(r-1)*M; i<=(r-1)*M; i++)*

for (j=-M;j<=M; j++)

$$A_{r,i+j} = A_{r,i+j} + A_{r-1,i} * V_j$$

(2.5.1.18)

Here, N stands for the maximum order of the nonlinearity and M the number of the data points. Substituting Equation (2.5.1.17) into Equation (2.5.1.15) gives the expression for the total current as:-

$$I(t)=\sum_{i=0}^{\infty}\left(a_i+(k+1)C_i\sum_{m=-N}^{N}jm\omega V_m\exp(jm\omega t)\right)\sum_{n=-iN}^{iN}A_{i,n}\exp(jn\omega t)$$

(2.5.1.19)

Following algebraic re-arrangement of Equation (2.5.1.19), the expression for the total device current can be written as:

$$I_n=\sum_{k=0}^{\infty}\left(a_kA_{k,n}+j\omega(k+1)C_k\sum_{m=-kN}^{kN}(n-m)V_{n-m}A_{k,m}\right)\exp(jn\omega t)$$

(2.5.1.20)

Dividing Equation (2.5.1.20) by $V_n(t)$, we obtain another Equation expressing the embedding admittance for the n-th harmonic:

$$Y_n=\frac{I_{d,n}(t)}{V_{d,n}(t)}=\frac{I_n}{V_n}=\sum_{k=0}^{\infty}\left(\frac{a_kA_{k,n}}{V_n}+j\omega C_k\frac{(k+1)}{V_n}\sum_{m=-kN}^{kN}(n-m)V_{n-m}A_{k,m}\right)$$

(2.5.1.21)

Equivalently, Equation (2.5.1.21) can be rewritten as:-

$$\frac{I_{d,n}(t)}{V_{d,n}(t)}-\sum_{k=0}^{N}\frac{a_kA_{k,n}}{V_n}=\sum_{k=0}^{\infty}\left(j\omega C_k\frac{(k+1)}{V_n}\sum_{m=-kN}^{kN}(n-m)V_{n-m}A_{k,m}\right)$$

(2.5.1.22)

C_k's of Equation (2.5.1.22) represent the coefficients of the power series (or Equation (2.5.1.5)) expressing the nonlinear capacitance, and can be resolved by Singular Value Decomposition, given that the I-V characteristic in power series and the frequency-domain measurements (i.e. $I_{d,n}(t)$ and $V_{d,n}(t)$) are known beforehand.

In general, the Fourier Series Decomposition technique can be accurately applied to most strongly nonlinear single-tone applications, while the rigorous algebraic expansion is better suited to weakly nonlinear systems and can be approximately extended to multi-tone applications.

2.5.2 DEMONSTRATION: CHARACTERATION OF RESONANT TUNNELING DEVICE CAPACITANCE

Table 2.5.1.1 shows an example set of measurements obtained when the source was pumped at Power=9.5 dbm and Freq=2 Ghz. Based on the I-V behavioral model given in Equation (2.4.3.2) and the frequency-domain measurement as given in Table 1, the voltage-dependent capacitance characteristic was obtained using previously described Fourier Series Decomposition. Rigorous Algebraic Expansion was not used because of the highly nonlinear nature of the Quantum Barrier Device. Fig. 2.6.2.2. illustrate the C-V characteristic modeled respectively using Equation (2.5.1.13).

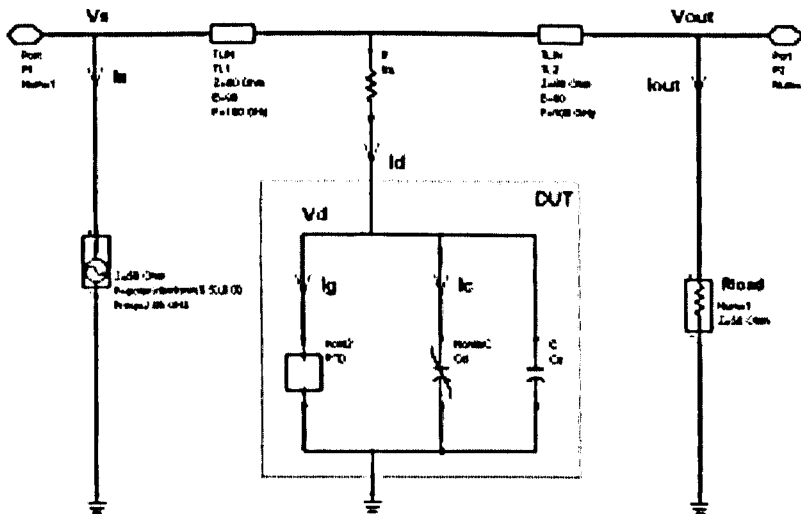

Fig.2.6.2.1 Schematic of Experimental Setup for CV Measurement.

(here, the skin resistance was modeled using the method described in Section 2.6.)

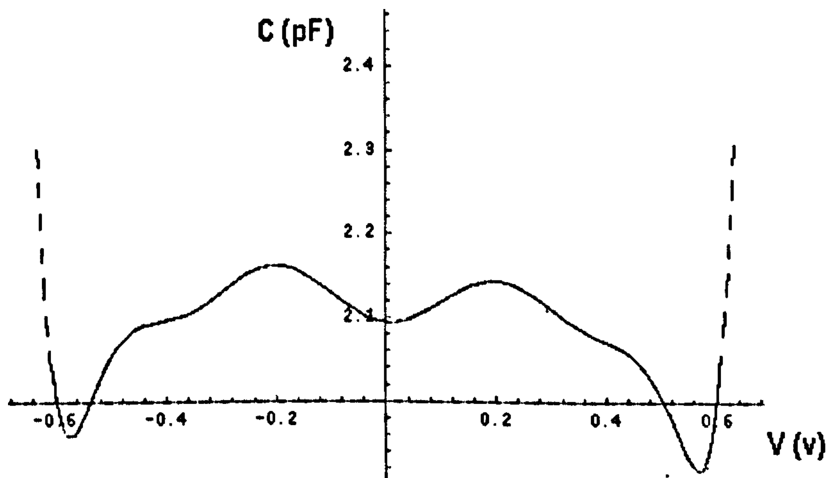

Fig. 2.6.2.2 C-V characteristic of the RTD, modeled using Fourier Series Decomposition.

Frequency (Ghz)	Measured Power of R_L (dBm)	Simulated Power of R_L (dBm)
2.0	2.73	2.66
4.0	-40.17	-43.646
6.0	-30.17	-29.225
8.0	-48.33	-48.918
10.0	-40.83	-38.745
12.0	-55.43	-55.071
14.0	-45.67	-48.980
16.0	(not visible)	-62.188
18.0	-44.67	-59.158

Table 2.5.1.1 Measured and simulated output harmonics at Rload, when the source was fundamentally driven at Power=7.5 dbm and frequency = 2 Ghz.

The power measurement at Rload was carried out using a spectrum analyzer which gives amplitude but not the phase. However, this measurement is preferably done using a Transition Analyzer which gives amplitude and phase.

The variation of capacitance shown in Fig. 2.1.2.2 was unusually small. This capacitance was obtained using the circuit of Fig. 2.6.2.1 where the C-V relationship was modeled using Fourier Series Decomposition and where the value of R_s was obtained using the skin-resistance to be discussed in Section 2.6. The simulated harmonics are somewhat in agreement with the measured harmonics. But this observation has not been independently verified.

2.6. SIMULATION MODEL OF SKIN LOSSES

This section discusses the modeling approach for the skin resistance at the device terminals. The skin effect, which may not be noticeable below microwave frequencies. However, as the operating frequency increases, the skin effect in the device terminals causes not only attenuation of signals but also the distortion [17,18,19]. Most existing modeling methods fail to describe the time domain behavior of these effects. The problem lies in the fact that many physics-based models for skin-effect loss and dielectric loss exhibit a non-causal behavior that can be observed in time-domain simulation. In incorporating the skin-effects into circuit simulations, some microwave EDA tools use a frequency domain description in the model and use Fourier-like Transforms to convert the calculated signal to the time-domain [16]. But due to the "non-causal" description of the $\sqrt{frequency}$ dependency [16], the overly simplified skin effect description in the frequency domain constantly leads to "non-physical" transient simulations.

Fortunately, there exist a number of public domain models that approximate the $\sqrt{frequency}$ dependency using a frequency-independent lump-element network. In general, the lump-element model is very easy to compute without running into the "non-causal" problem in transient simulations. Although the lumped element model tends to be accurate only for a limited frequency range, the accuracy of the model improves as the complexity of the lumped-element model increases. The lumped-element model containing 12 elements can adequately describe the inductance and the resistance due the skin effect up to 10 Thz.

One classical technique to realize a lumped element network modeling the skin loss is the LR ladders proposed by Yen et al [17]. In this technique, a round wire is regarded as a cascade of multiple concentric shells, as illustrated in Fig. 2.6.1 (a), each of which is considered as a step. The LR ladder network modeling the picture in Fig. 2.6.1 (a) is illustrated in Fig. 2.6.1.b, where R_l and L_l respectively correspond to to the resistance and inductance of the l-th shell in Fig. 2.6.1 (a). Yen proposed the use of step such that the resistance ratio X from one

step to the next is constant, i.e. $X = R_i / R_{i+1}$, where X is a constant determined by equating the total resistance at DC. Given that r is the radius of the round wire, the radius of the i -th shell is then:

$$r_i = r\sqrt{\sum_{j=i+1}^{M}\left[\sum_{n=1}^{M} X^{M-j-n+1}\right]^{-1}}$$

(2.6.1)

where M denotes the maximum number of current-carrying shells modeling in a round wire shown in Fig. 2.6.1.(a). For the i-th shell, the resistance and the inductance is given respectively as:

$$R_i = \frac{1}{\sigma\pi r^2}\sum_{j=0}^{M-1} X^{M-j-i}$$

(2.6.2)

and

$$L_i = \frac{\mu(r_{i-1} - r_i)}{2\pi r_i}$$

(2.6.3)

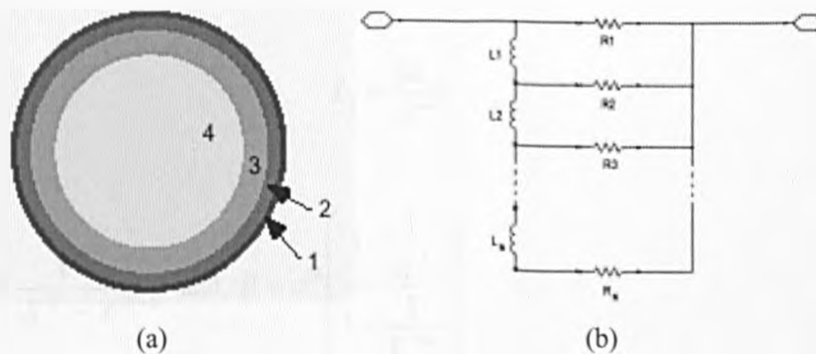

(a) (b)

Fig. 2.6.1 (a) Cross-sectional view of a round wire with 4 current carrying shell; and (b) The equilivent ladder network modeling the skin effect of the round wire. Here R_i and L_i

respectively represents the resistance and the inductance of the i-th shell.

Yen's approach is not without disadvantages. In most cases, this approach requires an excessively large ladder network to approximate the $\sqrt{frequency}$ dependency with reasonable accuracy. It has been identified by Kim and Neikirk[18] that the resulting model tends to underestimate the overall inductance and resistance.

Fortunately, many newer approaches were developed enhanceing Yen's proposed technique. One example is the approach proposed by Sen [19], who used an entirely different topology to approximate the $\sqrt{frequency}$ dependency. Here, the ratio from one shell to another is first fixed at $X=\sqrt{10}$. The original reference [19] does not contain any general formula to calculate the skin loss, although consideratble written descriptions were provided to the author. For this reason, the resistance and the inductance of the i- th shell is given without proof as follows:

$$R_i = \alpha R_{dc} X^{i-1} \tag{2.6.4}$$

and

$$L_i = \frac{\beta L_{dc}}{X^{i-1}} \tag{2.6.5}$$

where $\alpha = \dfrac{X^N - 1}{X^N - X^{N-1}}$ and $\beta = \alpha^2 \left(\dfrac{1 - \dfrac{1}{X^3}}{1 - \dfrac{1}{X^{3N}}} \right)$.

Fig. 2.6.2 illustrates the network topology adopted by Sen [19].

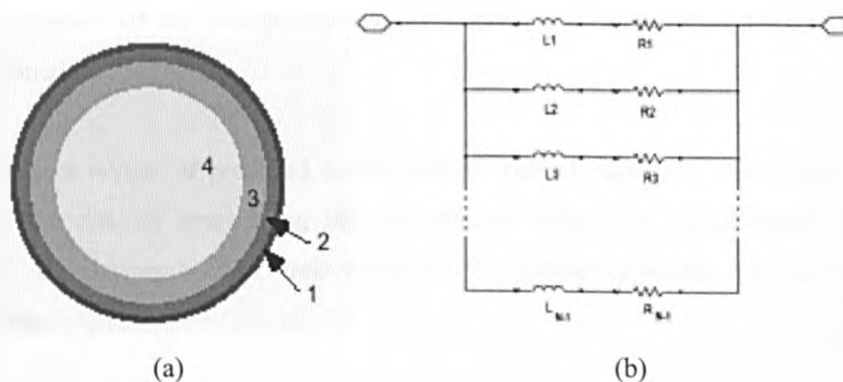

Fig. 2.6.2 (a) Cross-sectional view of a round wire; (b) Sen et al [19] equilivent network modeling the skin effect of the round wire. Here R_i and L_i respectively represents the resistance and the inductance of the i-th shell.

Equation (2.6.4) and (2.6.5) were used to derived a lumped-element model for Rs in the schematic of Fig. 2.6.2.1. In 1~10 Ghz, the value of Rs is in the neighbourhood of 6 Ohm.

2.7 CONCLUSIONS

In conclusion, this chapter has presented an analytical review on the physics-based models of Resonant Tunneling Diode (RTD), covering the treatment of the current-voltage characteristic, capacitance-voltage characteristic and the skin effect impedance of the device terminals. Although the existing physics-based models bridge the gap between the quantum mechanics and simulation models, there exist several unresolved issues that justify the use of measurement based modeling approaches. In this chapter, the development of the following measurement-based techniques were presented: -

characterization of the current-voltage relation of a Quantum Barrier Device using

continuity-function-approach and step-function-based approach; and

b) characterization of the voltage-dependent capacitance of a Quantum Barrier Device in frequency domain.

In addition, a review of proposed causal lumped element models of skin effect has been given with the aim of overcoming the convergence difficulties encountered in circuit simulations in microwave EDA tools which use the frequency domain physics-based skin effects models.

REFERENCES

[1] L. Esaki, "New Phenomenon in Narrow Germinium P-N Junctions", *Physical Review*, Vol. 109, pp. 603, 1958

[2] R.Tsu and L. Esaki, "Tunneling in a Finite Superlattice," *Applied Physics Letters*, Vol. 22, pp. 562-564, 1973

[3] L.L. Chang, L. Esaki, and R. Tsu, "Resonant Tunneling in Semiconductor Double Barriers," *Applied Physics Letters*, Vol. 24, no. 12, pp.593-595, June 1974

[4] T.C.L.G. Sollner, W.D. Goodhue, P.E. Tannenwald, C.D. Parket, D.D. Peck, and H.Q. Le, "Resonant Tunneling Through Quantum Wells up to 2.5 THz," in Conference Digest – 8th *International Conference on Infrared and Millimeter Waves*, 1983

[5] E. R. Brown, J. R. Soderstrom, C. D. Parker, L. J. Mahoney, K. M. Molvar, and T.C. McGill, "Oscillations up to 712 GHz in InAs/AlSb resonant-tunneling diodes," *Appl. Phys. Lett.*, Vol. 58, pp. 2291-2293, May 1991

[6] J.N. Schulman, H.J. De Los Santos, and D.H. Chow, "Physics-Based RTD Current-Voltage Equation", *IEEE Electron Device Letters*, Vol. 17, no. 5, May 1996

[7] Gerjuoy, E., and COON, D. D.: "Analytic S-matrix considerations and time delay in resonant tunneling', *Superlattices Microstruct.*, 5, (3), pp. 305-315, 1989

[8] E.R. Brown, O.B. McMahon, L.J. Mahoney and K.M.Molvar, "SPICE model of the rresonant-tunneling diode', *Electronics Letter*, Vol.32, No.10, May 1996

[9] W. Y. Liu, M. B. Steer, D. P. Steenson, "Characterization of Nonlinear Device Capacitance

in Frequency Domain," 8th *IEEE International Symposium on High Performance Electron Devices for Microwave and Optoelectronic Applications.*, pp. 253-258, Nov. 2000.

[10] Yuming Hu and Shawn P. Stapleton, "Double-Barrier Resonant Tunneling Transport Model" *IEEE Journal Of Quantum Electronics.*, Vol. 29, No. 2, pp. 327-339, Feb. 1993.

[11] D. L. Woolard, F. A. Buot, D. L. Rhodes, X Lu, and B. Sperlman, "An Assessment of Potential Nonlinear Circuit Models for the Characterization of Resonant Tunneling Diodes", *IEEE Trans. on Electron. Devices.*, Vol. 43, No. 2, pp. 332

[12] Anthony E Parker, "A Realistic Large-Signal MESFET Model for SPICE", *IEEE MTT-S Digest.*, Vol. 3, pp. 1763, 1996

[13] A. E. Parker, "Implementing high-order continuity and rate dependence in SPICE models", *IEE Proc-Circuits Devices Syst.*, Vol. 141, No.4, August 1994

[14] T.R. Arabi, A. T. Murphy, T. K. Sarkar, R. F. Harrington and A. R. Diordjevic, "On the Modeling of Conductor and Substrate Losses in Multiconductor, Multidielectric Transmission Line Systems", *IEEE Trans. On Microwave Theory and Techniques*, Vol. 39, pp. 1099-1237, July 1991

[15] J. I. Alonso, J. Borja and F. Perez, "A Universal Model for Lossy and Dispersive Transmission Lines for Time Domain CAD of Circuits", *IEEE Trans. On Microwave Theory and Techniques*, Vol. 40, pp. 938-947, May 1992

[16] "Transient Convolution Circuit Simulation", Agilent ADS, 2001

[17] C. S. Yen, Z. Fazarinc, and R.L. Wheeler, "Time Domain Skin Effect model for Transient Analysis of Lossy Transmission Lines", *Proceeding of the IEEE*, Vol 70, pp 750-767, 1982

[18] Kim S, and Neikirk D.P. , "Compact Equivalent Circuit Models for the Skin Effect", *Microwave Symposium Digest, IEEE MTT-S International*, Vol 3, pp 1815-1818, 1996

[19] B.K. Sen and R. L. Wheeler, "Skin Effects models for Transmission Line Structures using Generic SPICE Circuit Simulators", *Electrical Performance of Electronic Packaging, 1998, IEEE* 7th *Topical Meeting, 98*, pp 128-131, 1998

[20] Jan Genoe, C.V. Hoof, W.V. Roy, J.H.Smet, K. Fobelets, R. P. Mertens and G. Borghs, "Capacitances in Double-Barrier Tunneling Structures", *IEEE Trans. On Electron Devices*, Vol. 38, No. 9, Sep 1991

[21] S.Luryi, "Quantum capacitance devices," *Appl. Phys. Lett.*, Vol. 52, pp. 501-503, 1988

[22] D. P. Steenson, "High Frequency Applications of Quantum Barrier Devices," Doctor Dissertation, University of Leeds, 1994

[23] G.W.Rhyne, M.B.Steer, and B.D.Bates, " Frequency domain nonlinear circuit analysis using generized power series," *IEEE Trans. Microwave Theory Tech.*, Vol. 36, pp. 379-387, Feb. 1988

[24] C. R. Chang, M. B. Steer, and G. W. Rhyne, " Frequency domain spectral balance using the artithmetic operator method," *IEEE. Trans. Microwave Theory Tech.*, Vol. 37, pp. 1681-1688, Nov. 1988

[25] A. Ushida and L. O. Chua, " Frequency domain analysis of nonlinear circuits driven by multi-tone signals," *IEEE Trans. Circuits Syst.*, Vol. CAS-31, pp. 766-779, Sept. 1984

[26] W.Y. Liu, D.P. Steenson, " Frequency-domain characterization of conductance and capacitance of Resonant Tunnelling Diode," *2001 International Symposium on Electron Devices for Microwave and Optoelectronic Applications*, EDMO 2001, Nov. 2001

Chapter 3: Theory of Subharmonic Mixing

3.1 INTRODUCTION

The overall focus of this dissertation is the development of the technology for Quantum Barrier Subharmonic mixers at microwave and millimeter wave frequencies under the condition of weak excitation of local oscillator pump. Subharmonic mixer has been identified as a key technology to achieve this and, as we demonstrate in this chapter, Quantum Barrier Devices (QBD's) have a unique characteristic leading to particularly attractive performance when used as the active device in a microwave subharmonic mixer.

This chapter addresses general theoretical aspects of subharmonic mixing, with particular reference given to subharmonic mixing using a double barrier resonant tunneling diode. Like many other devices, double barrier devices have a non-Schottky like nonlinear characteristic that accordingly offers non-exponential mixing behavior. Analytical evidence, together with experimental proof-of-principle results, are presented for a non-schottky mixer in order to demonstrate how the intrinsic effects can effectively control the device nonlinearities and, therefore, the mixing performance. Such behavior is not found with Schottky junctions, and can be used to provide efficient subharmonic operation at microwave and low millimeter-wave frequencies with the significant advantage of permitting the use of very low levels of local-oscillator power.

3.2 DOUBLE BARRIER DEVICE AS A MIXING DEVICE

Subharmonic mixers are widely employed as down-converters operating at microwave to terahertz frequencies, with the advantages of broadband performance. The most useful characteristic generally attributed to subharmonic mixers is that less local oscillator power is required to drive a subharmonic mixer than to multiply a lower frequency source and drive a direct mixer. The most common type of subharmonic mixers are realized with a pair of Schottky diodes connected in antiparallel, the purpose of which is to generate an anti-symmetric current-voltage characteristic which has the effect of suppressing the odd-order mixing that can otherwise reduce the power available for higher frequency even-order mixing products. Although two diodes connected in antiparallel is conceptually simple, any mismatch in the physical and electrical characteristics between the two diodes will potentially waste the LO power that could otherwise be used for the desired harmonic components. It becomes particularly difficult to achieve required matching at submillimeter-wave and terahertz frequencies. A much more attractive alternate solution is to replace the pair of antiparallel diodes with a single quantum barrier device (QBD) [5], [6], [8], [9], [11], [12] which has a highly non-linear and anti-symmetric current-voltage characteristic intrinsic to the device. This is just one of the advantages that justify the use of a single QBD in realization of a subharmonically pumped mixer.

Another advantage attributed to the QBD is that the zero-bias capacitance of a QBD can be effectively offset by an additional depletion layer adjacent to the double-barrier well. Susceptance at the frequencies that are concerned with can easily dominate device conductance. Thus, the unbiased capacitance normally contributes negative effects to the overall mixing performance. In a mixer operating at upper millimeter-wave frequencies and beyond, at which the unbiased capacitance easily becomes a dominant factor, QBD's appear to be a more flexible device than the Schottky junctions in this respect.

Additionally, barriers of a QBD can be tailored during fabrication in such a way that the

nonlinearities associated with the device can be tailored for optimal performance given the available LO power. It is also possible to choose different layer structures for a device of the same diameter to obtain optimum resistive nonlinearities. Flexibility to modify the nonlinearities at a device level or in terms of the transmission coefficient resulting from quantum interference effects, together with the flexibility to modify the electron distribution in the emitter (i.e., the supply function) means a flexibility to tailor the nonlinear behavior to favor different operating conditions. This is the primary advantage identified for using QBD's as microwave subharmonic mixers. The excellent intrinsic mixing performance has been reported previously in References [6], [8], and [9]. Tait [8] has also identified other advantages of a heterojunction barrier device suitable for millimeter-wave mixer design, including the opportunities to fabricate low-barrier-height structures that reduce the LO power requirements and to improve device reliability under both continuous-wave and pulsed-power operation. This has been experimentally demonstrated by the authors using a QBD in an another similar experiment [9], in which a conversion less than 9 dB was achieved for an 18–1-GHz subharmonic mixer using a double barrier device in the absence of any dc bias. Mixing with conversion gain at 12 GHz has also been demonstrated as being possible when biased negatively or positively to the negative dynamic resistance region [8]. These results show that superior mixing performance of a QBD at microwave frequencies can be expected but this has not been analytically justified.

For readers' convenience, a table for comparison of Quantum Barrier Performance with Schottky performance is included as follows:

Table 3.1.1 Comparison between Quantrum Barrier performance and Schottky performance

	Unbiased Quantum Barrier Mixer	Biased Self-oscillating Quantum Barrier Mixer	Schottky-based Mixer
Maximum RF Frequency (GHz)	20 [9,11,12]	18 [6]	2500 [19-21]
Minimum LO Power (dbm)	-20	N/A	+5
Bias Requirement	N/A	Bias to the NDR region	N/A
Conversion Gain (dB)	-5.5 [9,11,12]	+10 dB at 12 Ghz [6] +40 dB at 18 Ghz [12]	-5.5 [14-18]
Remarks	* Unstable over frequencies; * Subharmonically pumped at the 2nd harmonic	* Unstable over frequencies;	* Stable over frequencies; * Can work in fundamental or higher order subharmonic mode

3.2 DOUBLE BARRIER DEVICE AS A MIXING DEVICE

A discussion of an original approach to this problem was presented in Chapter 2. In the following sections, the general theories of harmonic mixing in a nonlinear network is reviewed, with particular reference given to the electrical behavior of a QBD. A more qualitative treatment is then given to identify the essential differences between the barrier and Schottky diodes. It is analytically shown that subharmonic mixers using QBDs can have superior performance and the circuit and device configurations when this is achieved are identified.

3.3. QUALITATIVE TREATMENT

In this section, the frequency-conversion mechanism of a generic two-terminal mixing device, as shown in Fig. 3.2.1, is qualitatively reviewed, before discussing the specific aspects related to QBD's. Most of the materials given in this Section are taken from Reference [11] and [12]. The analysis is focused on the intrinsic nonlinearities that can be modeled as a contribution of a nonlinear capacitor C_j and a nonlinear resistor, G_j connected in parallel (see Fig. 3.2.1). The series lead resistance R_s and other parasitic capacitance C_p attached to the device are temporarily assumed to be incorporated into the external network.

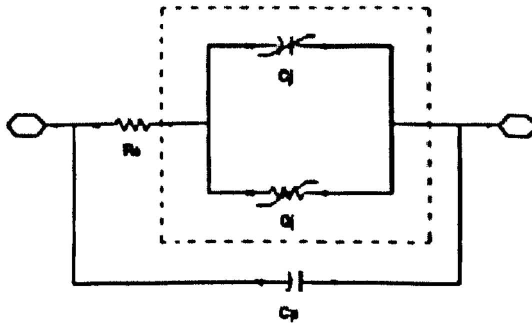

Fig. 3.2.1 Equivalent circuit of a nonlinear diode.

Under two-tone modulation, a nonlinear device is simultaneously excited by the two time-dependent sinusoidal signals, namely, the RF signal and the LO pump. In the presence of nonlinear operation, the voltage across the diode junction is given by Ref [15] as

$$V(t) = \sum_{m=1}^{\infty} v_{lo_m} \cos(m\omega_{lo}t + \varphi_m) + \sum_{k=-\infty}^{\infty} v_k \cos((\omega_{rf} - k\omega_{lo})t + \psi_k) \qquad (3.2.1.a)$$

where $v_{lo_m} \cos(m\omega_{lo}t + \varphi_m)$ stands for the mth harmonic of local oscillator voltage and

$v_k \cos((\omega_{rf} + k\omega_{lo})t + \psi_k)$ represents the mixing product for the kth harmonic. Equation (3.2.1.a) is valid only under the assumption that the diode is shorted at the harmonics of the RF, say by the virtual ground of the RF signal path. Converting Equation (3.2.1.a) into exponential form, we have:

$$V(t) = \sum_{\substack{m=-\infty \\ m\neq 0}}^{\infty} V_{lo_m} \exp(jm\omega_{lo}t) + \sum_{k=-\infty}^{\infty} V_k \exp(j(\omega_{rf} - k\omega_{lo})t)$$

(3.2.1.b)

where V_{lo_m} and V_k are given as:

$$V_k = \frac{v_k \exp(j\psi_k)}{2}$$

(3.2.1.c)

and

$$V_{lo_m} = \frac{v_{lo_m} \exp(j\varphi_m)}{2}$$

(3.2.1.d)

3.3.1 DECOMPOSITION OF RESISTIVE CURRENT INTO HARMONIC SUM (WEAKLY NONLINEAR CASE)

If the nonlinear resistance of a diode is weakly nonlinear, the nonlinearity can be modeled as a voltage-controlled current generator, with the nonlinear relationship given by Ref [12] as a power series:

$$i_g(t) = \sum_{i=0}^{\infty} a_i V(t)^i$$

(3.2.2)

Lets make two assumptions to simplify the frequency conversion analysis: a) As in the normal situation, the LO voltage is very much greater in magnitude than the RF signal and the

mixing products; b) the mixing products are band-limited. Under a resistive mixing condition, where conversion loss is a norm, it is reasonable to assume that

$$\sum_{m=1}^{\infty} v_{lo_m} \cos(m\omega_{lo} t + \varphi_m) >> \sum_{k=-\infty}^{\infty} v_k \cos((\omega_{rf} - k\omega_{lo})t + \psi_k) \tag{3.2.3}$$

Applying Taylor expansion on (3.2.2) about, and because of the assumption made in (3.2.3), the resistive current can be expressed in complex terms through a sequence of approximations:

$$I_g(t) \approx \sum_{i=0}^{\infty} a_i \left(\sum_{m=-\infty}^{\infty} V_{lo_m} \exp(jm\omega_{lo} t) \right)^i + \sum_{i=0}^{\infty} i a_i \left(\sum_{\substack{m=-\infty \\ m \neq 0}}^{\infty} V_{lo_m} \exp(jm\omega_{lo} t) \right)^{i-1} \sum_{k=-\infty}^{\infty} V_k \exp(j(\omega_{rf} - k\omega_{lo})t) \tag{3.2.4}$$

In Equation (3.2.4), the higher order effects of the mixing products are assumed to be negligible. The first term in the right hand side of Equation (3.2.4) is totally independent of any mixing products and RF signal. In mixer analysis, this term does not contribute to any effect on mixing performance. Hence, only the last term of Equation (3.2.4) needs to be considered and defined as:

$$I_{g_M}(t) \approx \sum_{i=0}^{\infty} i a_i \left(\sum_{\substack{m=-\infty \\ m \neq 0}}^{\infty} V_{lo_m} \exp(jm\omega_{lo} t) \right)^{i-1} \sum_{k=-\infty}^{\infty} V_k \exp(j(\omega_{rf} - k\omega_{lo})t) \tag{3.2.5}$$

where $I_{g_M}(t)$ is the time domain resistive mixing current. It is not possible to manually expand the bracketed term when the maximum harmonic order is too high. Instead, this term in Equation (3.2.5) is formulated into the following expression:

$$\sum_{i=0}^{\infty} ia_i\left(\sum_{m=-\infty}^{\infty} V_{lo_m}\exp(jm\omega_{lo}t)\right)^{i-1} = \sum_{i=0}^{N}\sum_{k=-N}^{N} ia_i A_{k,i}\exp(jk\omega_{lo}t)$$

(3.2.6)

where N is the maximum order of the polynomial given in Equation (3.2.1) and $A_{k,i}$ is a function of the local oscillator voltage V_{lo}. Manually expanding Equation (3.2.6) will show that

$$\sum_{i=0}^{\infty} ia_i\left(\sum_{m=-\infty}^{\infty} V_{lo_m}\exp(jm\omega_{lo}t)\right)^{i-1} \approx$$

$$a_1 + 2a_2\left(\sum_{m=-\infty}^{\infty} V_{lo_m}\exp(jm\omega_{lo}t)\right) +$$

$$3a_3\left(\sum_{m=-\infty}^{\infty}\sum_{n=-\infty}^{\infty} V_{lo_m}V_{lo_{m-n}}\exp(jm\omega_{lo}t)\right) + \ldots.$$

(3.2.7)

Here, a_1 is independent of the LO signal. Hence, in Equation (3.2.6), we have

$$A_{0,1} = 1 \text{ and } A_{m,2} = V_{lo_m}$$

(3.2.8.a)

If the I-V characteristic is anti-symmetrical, and if the C-V characteristic is symmetrical, it is not likely that the nonlinear operations of the LO will yield any DC component. Hence, it is reasonable to assume that, for a device with anti-symmetrical I-V characteristic and symmetrical C-V characteristic,

$$A_{0,m} \approx 0 \quad \text{, for } m \neq 1.$$

(3.2.8.b)

Symbolically expanding Equation (3.2.6) is tedious. Instead, $A_{k,i}$ can be numerically calculated using the following algorithm:

```
for  (r=1; r<=N; r++)
        for (i=-(r-1)*N; i<=(r-1)*N; i++)
```

$$for\ (j=-N;\ j<=N;\ \ j++)$$
$$A_{r,i+j} = A_{r,i+j} + A_{r-1,j} \times V_{lo}$$

where N is the maximum number of allowable harmonics under consideration.

Substituting Equation (3.2.6) into Equation (3.2.5) gives:

$$\begin{aligned} I_{g_M}(t) &\approx \sum_{m=N}^{N}\sum_{i=0}^{N} ia_i A_{m,i} \exp(jm\omega_{lo}t)\sum_{k=-\infty}^{\infty} V_k \exp(j(\omega_{rf}+k\omega_{lo})t) \\ &= \sum_{k=-N}^{N}\sum_{m=N}^{N}\sum_{i=0}^{N} ia_i A_{m,i} V_k \exp(j(\omega_{rf}+(k+m)\omega_{lo})t) \end{aligned} \tag{3.2.9}$$

Replacing $(k+m)$ by n in Equation (3.2.7):

$$I_{g_M}(t) = \sum_{m=N}^{N}\sum_{n=-N}^{N}\sum_{i=1}^{N} ia_i A_{m,i} V_{n-m} \exp(j(\omega_{rf}+n\omega_{lo})t) \tag{3.2.10}$$

Defining $\sum_{i=1}^{N} ia_i A_{m,i}$ as G_m,

$$I_{gM}(t) = \sum_{m=N}^{N}\sum_{n=-N}^{N} G_m V_{n-m} \exp(j(\omega_{rf}+n\omega_{lo})t) \tag{3.2.11}$$

3.3.2 DECOMPOSITION OF CAPACITANCE CURRENT INTO HARMONIC SUM (WEAKLY NONLINEAR CASE)

Similarly to the weakly nonlinear resistor, the weakly nonlinear capacitance of a pair of Schottky diodes connected antiparallel can be equally generalized into a power series to

describe any theoretical or experimentally observed capacitance versus voltage behavior (as demonstrated in Chapter 2):

$$C(t) = \sum_{i=0}^{\infty} c_i V(t)^i$$

(3.2.12)

The barrier current can be determined by the time derivative of the instant charge accumulated in the barriers. Since the instant charge accumulated in the junction is given as

$$Q(t) = C(t)V(t) = \sum_{i=0}^{\infty} c_i V(t)^{i+1}$$

(3.2.13)

Defining $b_{i+1} = c_i$, Equation (3.2.13) can be rewritten as:

$$Q(t) = C(t)V(t) = \sum_{i=0}^{\infty} b_{i+1} V(t)^{i+1} = \sum_{i=0}^{\infty} b_i V(t)^i$$

(3.2.14)

where $b_0 = 0$. Since Equation (3.2.14) and Equation (3.2.2) are similar in their forms, we can expand Equation (3.2.14) in the same manner, leading to the following expression for the charge,

$$Q_u(t) = \sum_{m=N}^{N} \sum_{n=-N}^{N} \sum_{i=1}^{N} i b_i A_{m,i} V_{n-m} \exp(j(\omega_{rf} + n\omega_{lo}))$$

(3.2.15)

Equivalently, since we have already defined $b_{i+1} = c_i$,

$$Q_u(t) = \sum_{m=N}^{N} \sum_{n=-N}^{N} \sum_{i=1}^{N} i c_{i-1} A_{m,i} V_{n-m} \exp(j(\omega_{rf} + n\omega_{lo}))$$

(3.2.16)

Here, c_0, which denotes the zero-bias capacitance, is independent of the LO signal. Likewise, defining $\sum_{i=1}^{N} i c_{i-1} A_{m,i}$ as B_m, we have

$$Q_M(t) = \sum_{m=N}^{N} \sum_{n=-N}^{N} B_m V_{n-m} \exp(j(\omega_{rf} + n\omega_{lo})t)$$

(3.2.15)

The reactive mixing current as a result of a change of charge can be determined simply by:

$$I_{bM}(t) =$$

$$\frac{d}{dt} Q_M(t) = \sum_{m=N}^{N} \sum_{n=-N}^{N} j(\omega_{rf} + n\omega_{lo}) B_m V_{n-m} \exp(j(\omega_{rf} + n\omega_{lo})t)$$

(3.2.16)

3.3.3 OVERALL MIXING EQUIVALENT

The total current flowing into the mixing device is the sum of the capacitive current due to the intrinsic nonlinear capacitance and the resistive current in the non-linear resistance. Adding Equation (3.2.11) and (3.2.16) together, we get:

$$i(t) = i_{bM}(t) + i_{gM}(t)$$

$$= \sum_{m=-N}^{N} \sum_{n=-N}^{N} (G_m + j(\omega_{rf} + n\omega_{lo}) B_m) V_{n-m} \exp(j(\omega_{rf} + n\omega_{lo})t)$$

(3.2.17)

It follows from (3.2.17) that the mixing product for the n th harmonic is related as:

$$I_n \exp(j(\omega_{rf} + n\omega_{lo})t)$$

$$= \sum_{m=-N}^{N} (G_m + j(\omega_{rf} + n\omega_{lo}) B_m) V_{n-m} \exp(j(\omega_{rf} + n\omega_{lo})t)$$

(3.2.18)

Equivalently, Equation (3.2.18) can be rewritten concisely as:

$$I_n = \sum_{m=-N}^{N} (G_m + j(\omega_{rf} + n\omega_{lo}) B_m) V_{n-m}$$

(3.2.19)

Equation (3.2.19) represents the general relationship between the harmonic voltages and currents under an open condition; that is, all harmonic components are short-circuited. Let's assume that each mixing product I_n and V_n is associated with an embedding admittance Y_{e_n} in the form of Equation (3.2.20), see Fig. 3.2.2:

$$I(n) = I_n + V_n Y_{e_n}$$

(3.2.20)

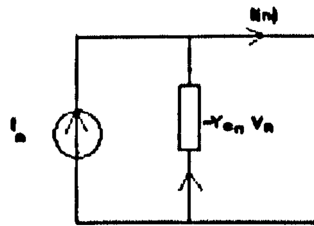

Fig. 3.2.2 Equivalent circuit of the embedding impedance for harmonic *n*.

where I (n) is the measurable current of the n th harmonic mixing product. Then, Equation (3.2.19) becomes:

$$I(n) = \sum_{\substack{m=-N \\ m \neq n}}^{N} \left(G_m + j\left(\omega_{rf} + n\omega_{lo}\right)B_m\right)V_{n-m} + \left(\left(G_0 + j\left(\omega_{rf} + n\omega_{lo}\right)B_0\right) + Y_{e_n}\right)V_n$$

(3.2.21)

Here, n indicates the harmonic number and the index $n = 0$ denotes the RF signal. In the following analysis, we let the p th harmonic of the local oscillator voltage mix with the RF signal to form an IF product at frequency $\omega_{rf} - p\omega_{lo}$. All harmonics other than the RF, the IF and the LO are considered short-circuited to ground. Because $G_m = G_{-m}$ and

$B_m = B_{-m}$, the whole mixing system can be expressed using an admittance-parameter matrix representation as:

$$\begin{bmatrix} I(0) \\ I(-p) \end{bmatrix} = \begin{bmatrix} Y_{00} & Y_{0p} \\ Y_{p0} & Y_{pp} \end{bmatrix} \begin{bmatrix} V_0 \\ V_{-p} \end{bmatrix}$$

(3.2.22)

where

$$Y_{00} = G_0 + j\omega_{rf} B_0 + Y_{e_0}$$

$$Y_{0p} = G_p + j\omega_{rf} B_p$$

$$Y_{p0} = G_p + j(\omega_{rf} - p\omega_{lo})B_p$$

$$Y_{pp} = G_0 + j(\omega_{rf} - p\omega_{lo})B_0 + Y_{e_p}$$

(3.2.23)

Alternatively, we can express Equation (3.2.22) using "2-port" S-parameters by replacing $I(-n)$ and V_{-n} with $\sqrt{Y_{e_n}}(a_n - b_n)$ and $(a_n + b_n)/\sqrt{Y_{e_n}}$ respectively, with n being a generic harmonic index, so that equation (3.2.22) becomes

$$\begin{bmatrix} \sqrt{Y_{e_0}}(a_0 - b_0) \\ \sqrt{Y_{e_p}}(a_p - b_p) \end{bmatrix} = \begin{bmatrix} Y_{00} & Y_{0p} \\ Y_{p0} & Y_{pp} \end{bmatrix} \begin{bmatrix} (a_0 + b_0)/\sqrt{Y_{e_p}} \\ (a_p + b_p)/\sqrt{Y_{e_p}} \end{bmatrix}$$

(3.2.24)

Rearranging Equation (3.2.24) gives:

$$\begin{bmatrix} b_0 \\ b_p \end{bmatrix} = \begin{bmatrix} \sqrt{Y_{e_0}} - Y_{00}/\sqrt{Y_{e_0}} & -Y_{0p}/\sqrt{Y_{e_0}} \\ -Y_{p0}/\sqrt{Y_{e_0}} & \sqrt{Y_{e_p}} - Y_{pp}/\sqrt{Y_{e_p}} \end{bmatrix}^{-1} \times \begin{bmatrix} \sqrt{Y_{e_0}} + Y_{00}/\sqrt{Y_{e_0}} & -Y_{0p}/\sqrt{Y_{e_0}} \\ -Y_{p0}/\sqrt{Y_{e_0}} & \sqrt{Y_{e_p}} + Y_{pp}/\sqrt{Y_{e_p}} \end{bmatrix} \begin{bmatrix} a_0 \\ a_p \end{bmatrix} \tag{3.2.25}$$

and the frequency domain S-parameter matrix is then:

$$[S] = \begin{bmatrix} \dfrac{(Y_{e_0} - Y_{00})(Y_{e_p} - Y_{pp}) + Y_{0p}Y_{p0}}{(Y_{e_0} - Y_{00})(Y_{e_p} - Y_{pp}) - Y_{0p}Y_{p0}} & \dfrac{2Y_{0p}\sqrt{Y_{e_p}Y_{e_0}}}{(Y_{00} - Y_{e_0})(Y_{pp} - Y_{e_p}) - Y_{0p}Y_{p0}} \\ \dfrac{2Y_{p0}\sqrt{Y_{e_p}Y_{e_0}}}{(Y_{00} - Y_{e_0})(Y_{pp} - Y_{e_p}) - Y_{0p}Y_{p0}} & \dfrac{(Y_{e_0} - Y_{00})(Y_{e_p} - Y_{pp}) + Y_{0p}Y_{p0}}{(Y_{e_0} - Y_{00})(Y_{e_p} - Y_{pp}) - Y_{0p}Y_{p0}} \end{bmatrix} \tag{3.2.26}$$

The conversion loss is just the square of 1/S[2,1]:

$$L_c = \frac{\left|\left(Y_{00} - Y_{e_0}\right)\left(Y_{pp} - Y_{e_p}\right) - Y_{0p}Y_{p0}\right|^2}{4\left|Y_{p0}\right|^2 \left|Y_{e_0}Y_{e_p}\right|}$$

$$= \frac{\left|\left(G_0 + j\omega_{rf}B_0 - Y_{e_0}\right)\left(G_0 + j\left(\omega_{rf} - p\omega_{lo}\right)B_0 - Y_{e_p}\right) - Y_{p0}Y_{0p}\right|^2}{4\left|G_p + j\left(\omega_{rf} - p\omega_{lo}\right)B_p\right|^2 \left|Y_{e_0}Y_{e_p}\right|}$$

(3.2.27)

Since in Equation (3.2.11) and (3.2.15), $\sum_{i=1}^{N} ia_i A_{m,i}$ was defined as G_m and $\sum_{i=1}^{N} ic_{i-1}A_{m,i}$ as B_m, Equation (3.2.27) can now be rewritten as:

$$L_c =$$

$$\frac{\left|\left(\sum_{i=1}^{N}\left(ia_i + j\omega_{rf}ic_{i-1}\right)A_{0,i} - Y_{e_0}\right)\left(\sum_{i=1}^{N}\left(ia_i + j\left(\omega_{rf} - p\omega_{lo}\right)ic_{i-1}\right)A_{0,i} - Y_{e_p}\right) - Y_{p0}Y_{0p}\right|^2}{4\left|\sum_{i=1}^{N}\left(ia_i + j\left(\omega_{rf} - p\omega_{lo}\right)ic_{i-1}\right)A_{p,i}\right|^2 \left|Y_{e_0}Y_{e_p}\right|}$$

(3.2.27.a)

Equation (3.2.27) gives an approximate formula to estimate the performance of a general p th harmonic mixer, and will be employed in Section 3.4 to demonstrate the factors that that favor the use of Quantum Barrier Device as a subharmonic mixing device.

3.3.4 IF VOLTAGE

As before, we assume that the voltage spectrum in the system contains only the IF, the RF and the LO components. Regardless of any embedding impedance that was assumed previously for

derivation of the conversion loss, let us suppose that the IF is passively terminated by Y_{if}. Then, by allowing the RF and IF components only in Equation (3.2.21), we obtain:

$$I(n) = -Y_{if}V_n$$
$$\left(G_0 + j(\omega_{rf} - n\omega_{lo})B_0\right)V_n + \left(G_n + j(\omega_{rf} - n\omega_{lo})B_n\right)V_0$$

(3.2.28)

With some algebraic rearrangement, Equation (3.2.28) can be rewritten as:

$$V_n = \frac{\left(G_n + j(\omega_{rf} - n\omega_{lo})B_n\right)V_0}{\left(Y_{if} + G_0 + j(\omega_{rf} - n\omega_{lo})B_0\right)}$$

(3.2.29)

The magnitude of the IF voltage becomes:

$$V_n = V_0\sqrt{\frac{\left|G_n\right|^2 + \left|(\omega_{rf} - n\omega_{lo})B_n\right|^2}{\left|\mathrm{Re}\{Y_{if}\} + G_0\right|^2 + \left|\mathrm{Im}\{Y_{if}\} + (\omega_{rf} - n\omega_{lo})B_0\right|^2}}$$

(3.2.30)

Since in Equation (3.2.11) and (3.2.15), $\sum_{i=1}^{N} ia_i A_{m,i}$ was defined as G_m and $\sum_{i=1}^{N} ic_{i-1} A_{m,i}$ as B_m, Equation (3.2.30) can now be rewritten as:

$$V_n = V_0\sqrt{\frac{\left|\sum_{i=1}^{N} ia_i A_{n,i}\right|^2 + \left|(\omega_{rf} - n\omega_{lo})\sum_{i=1}^{N} ic_{i-1} A_{n,i}\right|^2}{\left|\mathrm{Re}\{Y_{if}\} + \sum_{i=1}^{N} ia_i A_{0,i}\right|^2 + \left|\mathrm{Im}\{Y_{if}\} + (\omega_{rf} - n\omega_{lo})\sum_{i=1}^{N} ic_{i-1} A_{0,i}\right|^2}}$$

(3.2.31)

3.4 IMPLICATIONS FOR QBD-BASED SUBHAMONIC MIXER WITH LIMITED LOCAL OSCILLATOR PUMP

In the discussion that follows, the subtle features of the second harmonic mixer using a QBD will be qualitatively derived from the previously described analysis. It is assumed that the mixer is pumped with limited local oscillator power, which means that the device characteristic to be considered is weakly nonlinear.

3.4.1 VOLTAGE-INDEPENDENT ADMITTANCE AND UNBIASED CAPACITANCE

It is well known that the unbiased capacitance has a negative effect on the mixing performance. But there remains another parameter in the nonlinear resistance that potentially forms a parasitic burden to a mixer in the similar manner and that is due to discussed in this Section. To begin with, the expression of the conversion loss given in Equation 3.2.27.a is examined. For a p th harmonic mixer, the conversion loss derived in Equation 3.2.27.a can be rewritten:

$$L_c = \frac{\left| \left((a_1 + j\omega_{rf} i c_0) A_{0,1} + \sum_{i=2}^{N} (i a_i + j\omega_{rf} i c_{i-1}) A_{0,i} - Y_{e_0} \right) \times \left((a_1 + j\omega_{rf} i c_0) A_{0,1} + \sum_{i=2}^{N} (i a_i + j(\omega_{rf} - p\omega_{lo}) i c_{i-1}) A_{0,i} - Y_{e_p} \right) - Y_{p0} Y_{0p} \right|^2}{4 \left| \sum_{i=1}^{N} (i a_i + j(\omega_{rf} - p\omega_{lo}) i c_{i-1}) A_{p,i} \right|^2 \left| Y_{e_0} Y_{e_p} \right|} \tag{3.2.32}$$

It has already been proven in Equation (3.2.8.a) that $A_{0,1} = 1$. Also, by direct inspection of

Equation (3.2.6) and Equation (3.2.5), we have $A_{p,1} = 0$ for $p \neq 0$. Equation (3.2.32) can be simplified as:

$$L_c = \frac{\left| \left((a_1 + j\omega_{rf} ic_0) + \sum_{i=2}^{N} (ia_i + j\omega_{rf} ic_{i-1}) A_{0,i} - Y_{e_0} \right) \times \left((a_1 + j\omega_{rf} ic_0) + \sum_{i=2}^{N} (ia_i + j(\omega_{rf} - p\omega_{lo}) ic_{i-1}) A_{0,i} - Y_{e_p} \right) - Y_{p0} Y_{0p} \right|^2}{4 \left| \sum_{i=1}^{N} (ia_i + j(\omega_{rf} - p\omega_{lo}) ic_{i-1}) A_{p,i} \right|^2 \left| Y_{e_0} Y_{e_p} \right|} \tag{3.2.33}$$

The first two bracketed terms in the numerator of Equation (3.2.33) contains a_1 and c_0. Like the parasitic burden to a linear network, the effect of these two coefficients is to reduce the power of the mixing product when the p th harmonic of the LO is to mix with the RF signal. These two coefficients are essentially independent of the LO power. Hence, it is impossible to counter-balance the effect of these two coefficients by varying other parameters. In this regard, we can immediately conclude that minimizing a_1 in current-voltage characteristic, or c_0 in the capacitance-voltage characteristic, directly favors the mixing product at $\omega_{rf} - p\omega_{lo}$.

The coefficient a_1 represents the linear but voltage-independent conductance of the device, as graphically illustrated in Fig. 3.4.1.1, and this component has the effect of reducing the non-linear device current that could otherwise contribute to the mixing process. The slope around the origin, which corresponds to the value of a_1, should be minimized. Similarly, the coefficient c_0 represents the unbiased capacitance, which will in act to "shunt" off a proportion of the device current that would otherwise be used for mixing. In other words, both the voltage-independent conductance and the unbiased capacitance will significantly

impair the frequency conversion efficiency of a mixer and as such, should be minimized. The voltage-independent conductance, a_1, can also be minimized by cooling the device, without changing the peak current.

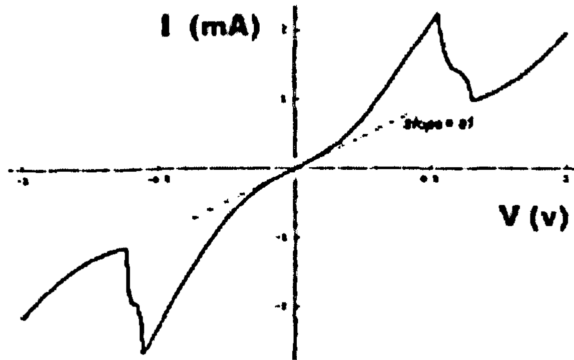

Fig. 3.4.1.1 Illustration of Voltage-independent Conductance, a_l

Mathematically, for very small value of $|V|$, a polynomial $I(V) = a_0 + a_1 V + ... + a_n V^n$ will behave like $I(z) = a_0 + a_1 V$ or $I(V) = a_0 + a_m V^m$, with $m \geq 1$, where the first order coefficient a_1 is referred to here as the linear conductance that makes no contribution to the mixing process. When a mixer is sub-harmonically pumped at a low LO power, the effect of the linear conductance a_l is especially significant in increasing the conversion loss. In this case, it is expected that, for a_2 and c_l are both negligible (i.e. anti-symmetric I-V characteristic and symmetric C-V characteristic), the IF voltage given by Equation (3.2.31) will behave like Equation (3.2.34):

$$V_n \approx V_0 \sqrt{\frac{\left|a_1 + 3a_3\left(\sum_{m=-\infty}^{\infty}\sum_{k=-\infty}^{\infty} V_{lo_k} V_{lo_{m-k}}\right)\right|^2 + \left|\left(\omega_{rf} - n\omega_{lo}\right)\left(c_0 + 2c_2 \sum_{m=-\infty}^{\infty}\sum_{k=-\infty}^{\infty} V_{lo_k} V_{lo_{m-k}}\right)\right|^2}{\left|\mathrm{Re}\{Y_{if}\} + a_1 + 3a_3 \sum_{m=-\infty}^{\infty}\sum_{k=-\infty}^{\infty} V_{lo_k} V_{lo_{m-k}}\right|^2 + \left|\mathrm{Im}\{Y_{if}\} + \left(\omega_{rf} - n\omega_{lo}\right)\left(c_0 + 2c_2 \sum_{m=-\infty}^{\infty}\sum_{k=-\infty}^{\infty} V_{lo_k} V_{lo_{m-k}}\right)\right|^2}}$$

(3.2.34)

If the capacitance effect is suppressed, say by using a relatively low IF frequency, Equation (3.2.34) can be further reduced to:

$$V_n \approx V_0 \frac{a_1 + 3a_3\left(\sum_{m=-\infty}^{\infty} \sum_{k=-\infty}^{\infty} V_{lo_k} V_{lo_{m-k}} \right)}{\mathrm{Re}\{Y_{if}\} + a_1 + 3a_3 \sum_{m=-\infty}^{\infty} \sum_{k=-\infty}^{\infty} V_{lo_k} V_{lo_{m-k}}}$$

(3.2.35)

While the presence of a_1 reduces the IF voltage, V_n, the role of a_3 is to scale up the effect of the LO power, which monotonically increases the IF voltage until it reaches the NDR region. This phenomenon can be illustrated graphically by Region A of Fig. 3.4.2.2.

In the case of the double-barrier QBD, the voltage-independent conductance is most likely non-zero, due to the effects of inelastic scattering of electrons. However, the device non-linearity around the origin can be "tailored" by adding an appropriate depletion layer next to one of the barriers, by changing the barrier height or by increasing the well width. This depletion layer not only suppresses the first order linearity at low LO power, but also offsets the zero-bias capacitance. In doing so, more of the resultant current is contributed by the higher order nonlinearities, thus improving conversion loss at higher harmonic numbers. While the zero-bias conductance should be minimized, the current peak at the NDR regions should be maximized to make sure that the decrease in conductance is not due to the parasitic series resistance attributed to the device terminals. High peak current in an NDR region also implies that the high-order device nonlinearities become dominant over the low-order ones. This conclusion supports the theoretical prediction by Reference [16], in which the authors postulated that the I-V characteristic with large peak-to-valley ratio can substantially improve subharmonic mixing efficiency.

3.4.2 FIRST MINIMUM CONVERSION LOSS

If the LO power is further increased beyond the negative differential resistance (NDR) regions of the I–V characteristic, the approximation of (3.2.34) and (3.2.35) will no longer be valid. The conversion loss does not reach saturation in a conventional manner as commonly observed in Schottky mixing. Instead, it reaches the first minimum in the conversion loss versus LO power, as graphically illustrated in Fig. 3.4.2.2. After the first minimum, the IF power drops again until it reaches a valley.

For the sake of prediction of the mixing behavior at low LO application, we can still apply the appropriate approximation to describe the behavior to the first few orders, without over sacrificing accuracy. In order to visualize this effect mathematically, we can approximate (3.2.35), say, by incorporating the next higher order effect into the equation, as

$$V_2 \approx \frac{3a_3\left(\sum_{m=-\infty}^{\infty} V_{lo_m} \exp(jm\omega t)\right)^2 + 5a_5\left(\sum_{m=-\infty}^{\infty} V_{lo_m} \exp(jm\omega t)\right)^4}{\left(\mathrm{Re}\{Y_{if}\} + a_1\right) + 3a_3\left(\sum_{m=-\infty}^{\infty} V_{lo_m} \exp(jm\omega t)\right)^2 + 5a_5\left(\sum_{m=-\infty}^{\infty} V_{lo_m} \exp(jm\omega t)\right) V_{lo}^4} \tag{3.2.35}$$

Equating $dV_2 / d\left(\sum_{m=-\infty}^{\infty} V_{lo_m} \exp(jm\omega t)\right)$ to zero, we obtain the condition leading to the first minimum IF voltage shown in (3.2.35):

$$\sum_{m=-\infty}^{\infty} V_{lo_m} \exp(jm\omega t) \approx \frac{-80\left(a_1 + \mathrm{Re}\{Y_{if}\} + \sqrt{400\left(a_1 + \mathrm{Re}\{Y_{if}\}\right)^2 - \dfrac{90a_3^2\left(a_1 + \mathrm{Re}\{Y_{if}\}\right)}{a_5}}\right)}{30a_3}$$

(3.2.36)

In Equation (3.2.36), if a_5 is negative such that it accounts for the existence of the NDR regions in the *I–V* characteristic, a greater magnitude of a_5 will result in lower LO voltage required to attain the first minimum in the IF voltage. Mathematically speaking, the greater the magnitude of any negative coefficient of the lowest order of a polynomial, such as in this instance, implies that the NDR regions will be closer to the current axis of the current-voltage characteristic. The lower LO power will be required to reach the first minimum in conversion loss if the NDR regions are drawn closer to the vertical-axis of the current-voltage characteristic. This observation, though may not be qualified as a formal proof of any kind, is consistent with the findings from the analysis given in Section 2.4.5. This can be achieved by growing the double barrier layers structure with wider quantum well. The high order of nonlinearities can be achieved during device fabrication by ensuring the barriers are sufficiently thin, that is, with large the transmission coefficients, and further enhanced by quantum confinement (quasi-2D) of the electron distribution in the emitter contact adjacent to the emitter barrier.

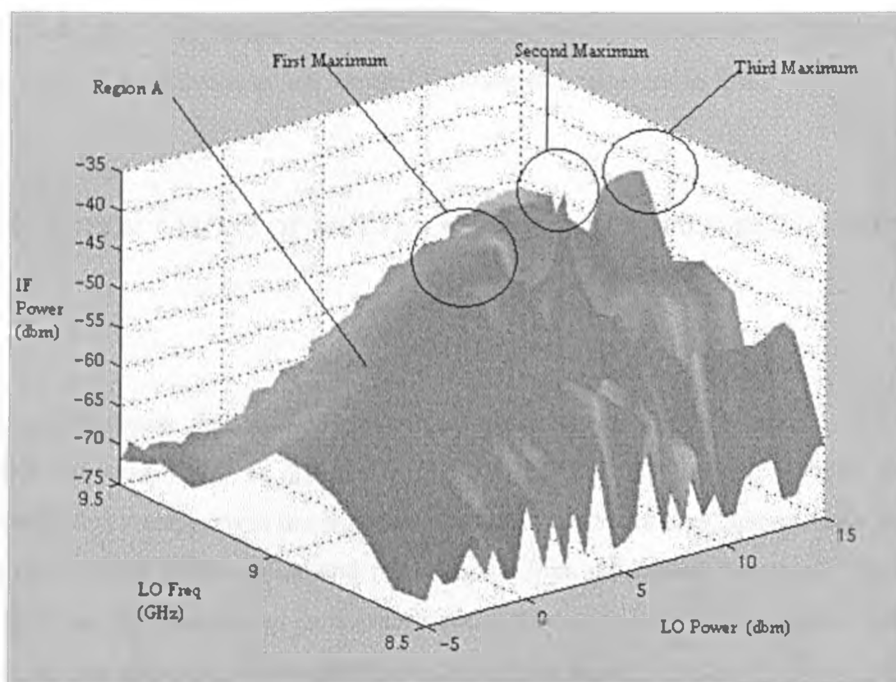

(a)

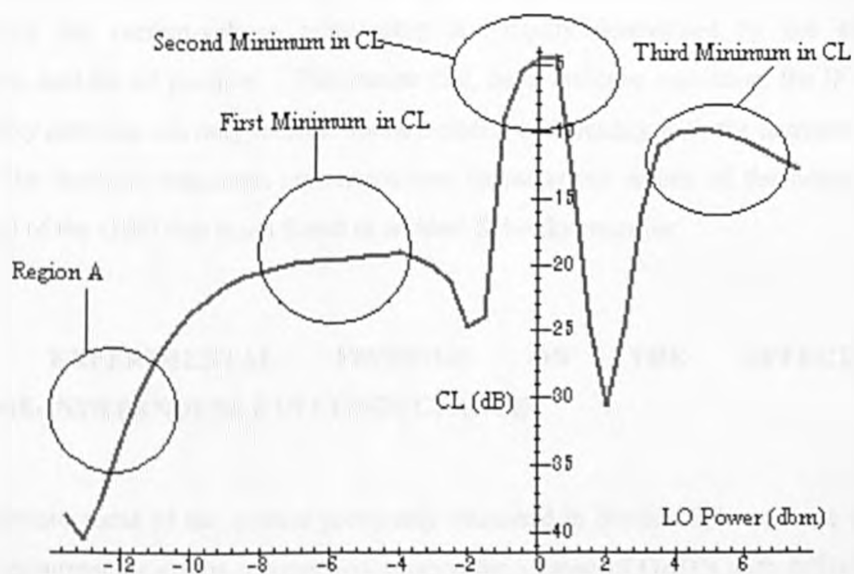

(b)

Fig. 3.4.2.2 (a) Measured IF power versus LO power characteristic. (b) Simulated conversion loss versus LO power (CL=conversion loss).

3.4.3 IMPLICATIONS OF MULTIPLE MINIMA (MAXIMA) IN CONVERSION LOSS

Another phenomenon that was observed from measurement and simulation is the multiple minima in conversion loss, as depicted in Fig. 3.4.2.2. The first, second and third minima in conversion loss corresponds to the regions of the QBD current-voltage characteristic, before the current peak, in the NDR region, and following on from the current minimum. Beyond the third minimum, the conversion loss characteristic is thought to saturate in a similar manner as a Schottky device, although this was not measured experimentally.

For Schottky junctions, however, the sign of the coefficients of their power series representing the current-voltage relationship are rigidly determined by the exponential relationship and are all positive. This means that, for a two-tone excitation, the IF voltage in the Schottky junction can only increase monotonically and steadily with the increase in the LO voltage. The multiple–minimum conversion-loss characteristic is one of the unique features (problems) of the QBD that is not found in an ideal Schottky junction.

3.5 EXPERIMENTAL FINDINGS ON THE EFFECTS OF VOLTAGE-INDEPENDENCE IN CONDUCTANCE

To substantiate some of the aspects previously discussed in Section 3.4, we have performed various measurements on the mixing performance for a range of QBD's with different device characteristics taken from molecular-beam-epitaxial layer alternatives. The results from two different devices and layers with different I-V characteristics are used to illustrate the

voltage-independent conductance. By comparison to the first layer structure, the second device features two 1.7 nm AlGaAs barriers and a 4.3nm GaAs well, and as previously mentioned the devices have the same diameter at 10 μm. Because the cross-sectional areas of these two devices are equal, and the doping adjacent to the barriers are roughly similar, it is expected that their zero-bias capacitances are largely similar. The test fixture employed for this investigation was a sub-harmonically pumped down-converter [9, 10, 11], which is schematically shown in Fig. 3.5.1. This mixer was originally designed to down-convert an RF signal at 20 GHz to an IF of around 1 GHz, with the LO input being subharmonically driven at around 8.5–9.5 GHz.

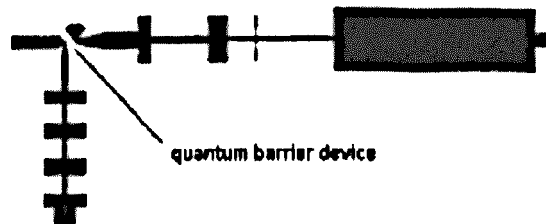

Fig. 3.5.1 Layout of the Test Fixture

Case 1: Device of 10 μ m in Diameter (Calculated Voltage-In-dependent Conductance=0.0016 **mho).**

Fig. 3.5.2 (a) shows the measured *I–V* characteristic of the QBD of 10 μ m in diameter based on a device featuring two 4.3-nm AlGaAs barriers separated by a 5.1-nm GaAs well. By calculation, the voltage-independent conductance was found to be 0.0016 mho. The best conversion loss was around 5 dB, when the LO power was subharmonically pumped 0.8 dBm. This conversion loss corresponds to the second minimum in Fig. 3.5.2 (b). When the LO power is reduced to around 2 dBm, the conversion loss is still less than 10 dB, which is

equivalent to the first minimum in Fig. 3.5.2 (b).

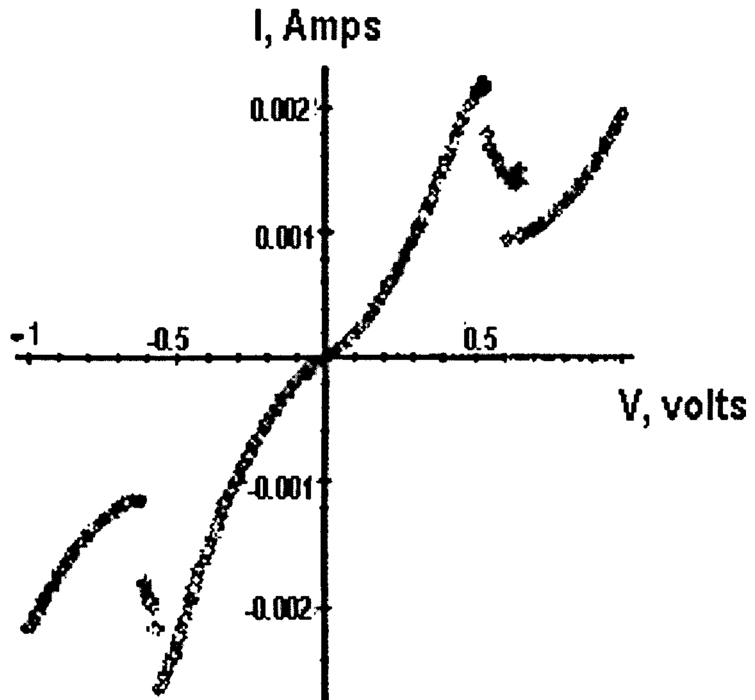

(a)

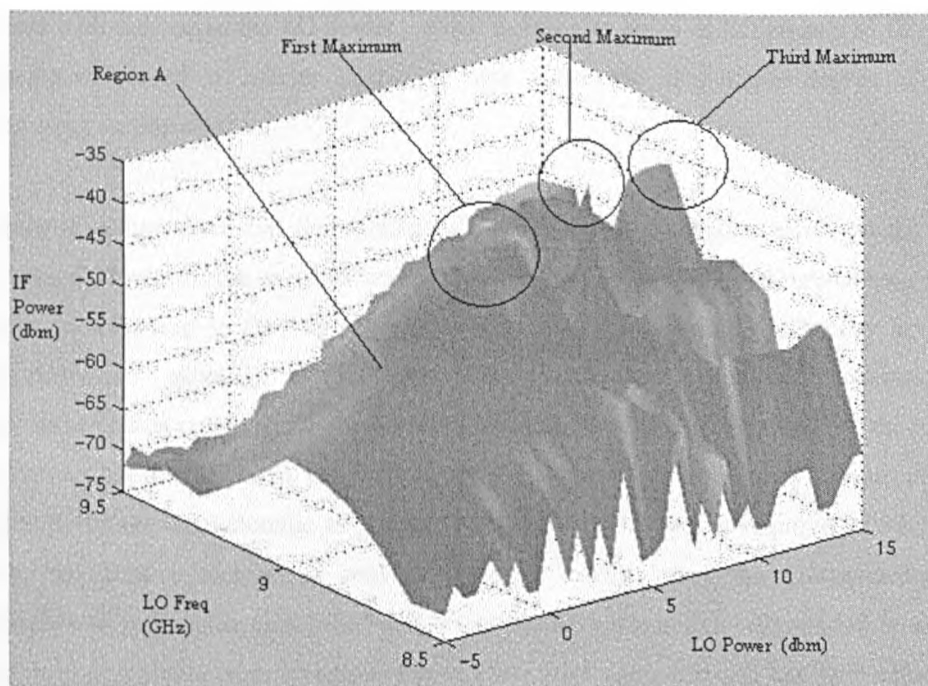

(b)

Fig. 3.5.2 (a) Measured I–V characteristic of QBD of 10 μm in diameter (voltage-independent conductance = 0.0016). (b) Measured IF power against LO frequency for LO power = 0 dBm, RF frequency = 20 GHz, RF power = -20 dBm.

***Case 2: Device of 10 μm in Diameter (Calculated Voltage-In-dependent Conductance = 0.024* mho).**

Fig. 3.5.3 (a) shows the measured I–V characteristic of the device featuring two 1.7-nm AlAs barriers separated by a 4.3-nm GaAs well. The device diameter is the same as that in case 1, but the current densities are different. The I–V characteristic of this device differs from the one in case 1 in that the NDR region of this case is much further away from the origin. The measured IF power versus LO frequency is shown in Fig. 3.5.3 (b) for different LO powers. The device is clearly operating below the NDR regions, where the conversion loss monotonically

decreases with the rise in the LO power. Over the similar range of LO powers to Case 1, the conversion efficiency is inferior to that in Case 1 because of a higher degree of voltage independence in this device.

There is no question that the unbiased capacitance has a negative effect on the mixing performance. However, the previous analysis, coupled with the actual measurements, generates a further hint leading to the improvement of the intrinsic conversion efficiency or the LO requirement. To maintain a reasonable LO efficiency for low LO operation, the voltage-independent conductance should be minimized, in addition to minimizing the unbiased capacitance. On the other hand, the NDR region should be drawn as close to the current-axis of the current-voltage characteristic as possible so that less LO power is required to reach, or go beyond, the first minimum in conversion loss. The lower the voltage-independent conductance as well as the closer the NDR regions to the current–axis will need to be achieved by selection of suitable layer structures during fabrication. This can and has been achieved by structures with increased well widths and with series-connected quantum wells.

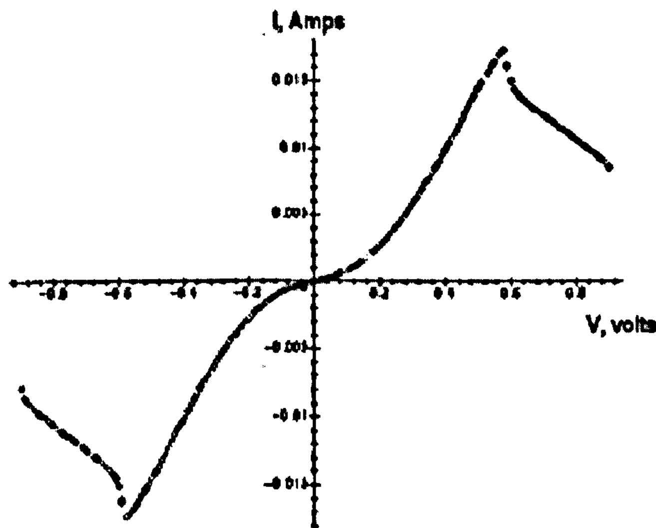

(a)

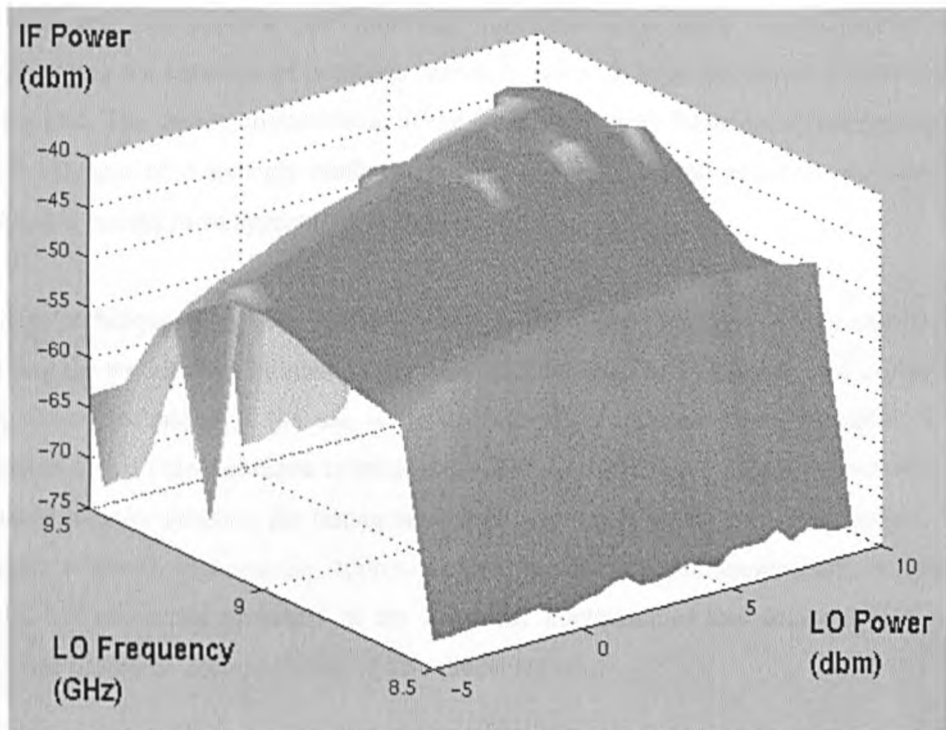

(b)

Fig. 3.5.3 (a) Measured I–V characteristic of QBD of 10 μm in diameter (voltage-independent conductance = 0.024). (b) Measured IF power against LO frequency for different LO power, RF frequency = 18 GHz, RF power =-23 dBm.

3.6. THE DEVICE WITH STRONGLY NONLINEAR CHARACTERISTIC

The analysis given in the Section 3.2 is based on an assumption that the nonlinear characteristic of the device can be described by a polynomial of limited degree. Power series or polynomials of limited degree are the simplest and most common means of approximating weakly nonlinear functions. Although the existence and uniqueness of polynomial modeling

of arbitrary data can be proven using the Weierstrass approximation theorem, polynomial functions are not suitable for modeling functions with sharp discontinuities or for approximating the behavior of functions near their poles, as large number of polynomial terms are required. The device characteristic of the Quantum Barrier Resonant Tunneling diode is a typical example of a strongly nonlinear device, for which power series or polynomial-type modeling is not the most appropriate form.

Many techniques have been studied for analysis of strongly nonlinear device characteristics, including the well-known rational interpolation techniques. The underlying idea of the rational interpolation technique is the use of rational function approximations in partial fractions expansion form. This technique is particularly useful in generating causal models of a highly nonlinear transfer function for timing simulation. However, when used in frequency domain analysis, whereby higher-order approximations of sharp discontinuities are required, the method has numerical problems in the low-order nonlinearities and is not appropriate for multi-tone harmonic decomposition of a nonlinear signal.

Many nonlinear applications, such as subharmonic mixing, are based on high order nonlinearities. It is important, in these applications, to accurately model the distortion, intermodulation, and transient behavior of the device. An accurate mathematical description of the device harmonic behavior is necessary to adequately capture the nonlinearities due to the sharp discontinuities in the electrical characteristic of the device. In characterizing the large signal behavior, the use of step-functions as described in Chapter 2 of this thesis is recommended to avoid the discontinuity in high-order derivatives. By way of example, consider the conditional statement of Equation (3.2.38), which is to be characterized. The step-function type modeling connecting the functions I_r and I_{r+} takes the form of Equation (3.2.37).

$$I = I_r + \frac{(I_{r+1} - I_r)}{1 + \exp\left(\frac{V_r - V}{k}\right)}$$

(3.2.37)

$$I = \begin{cases} I_r & ,\text{if } V < V_r \\ (I_r + I_{r+1}))/2 & ,\text{if } V = V_r \\ I_{r+1} & ,\text{if } V > V_r \end{cases}$$

(3.2.38)

Similarly, with more than one discontinuous transition along the current-voltage characteristic, we have:

$$I_G = I_0 + \sum_{r=0}^{N} \frac{(I_{r+1} - I_r)}{1 + \exp\left(\frac{V_r - V}{k}\right)}$$

(3.2.39)

where each I_r is a function of the voltage across the diode, V. V_r denotes the exact voltage at which the current segments I_{r+1} and I_r intersect. To find the time-domain expression of the current, we can simply substitute Equation (3.2.1), that is

$$V(t) = \sum_{m=1}^{\infty} v_{lo_m} \cos(m\omega_{lo}t + \varphi_m) + \sum_{k=-\infty}^{\infty} v_k \cos((\omega_{rf} + k\omega_{lo})t + \psi_k)$$

into Equation (3.2.39). Suppose that the time domain description obtained following this substitution is

$$I_G = I_g(V(\omega_{lo}t, \omega_{rf}t))$$

(3.2.40)

In order for Equation (3.2.30) to be usable in frequency domain, a 2-dimensional Fast Fourier Transform is employed to decompose Equation (3.2.40). The procedure begins by converting the time domain description of current into discrete form, by replacing $\omega_{lo}t$ with $2\pi n_{lo}/N_{lo}$ and $\omega_{rf}t$ with $2\pi n_{rf}/N_{rf}$, where N_{lo} and N_{rf} respectively represent the

maximum number of samples for the LO frequency and the RF frequency. Similarly, n_{lo} and n_{rf} of Equation (3.2.40) respectively denote the index of the discrete samples for the LO and the RF frequencies. The discrete form of Equation (3.2.41) is then:

$$I_G = I_G\left(V\left(\frac{2\pi n_{lo}}{N_{lo}}, \frac{2\pi n_{rf}}{N_{rf}}\right)\right)$$

(3.2.41)

Denote the LO harmonic m_{lo}, and the RF harmonic index, m_{rf}. Our goal in this exercise is to decompose the resistive current expression (3.2.41) into a sum of harmonic components, that is:

$$I_G = \sum_{m_{lo}=0}^{N_{lo}} \sum_{m_{rf}=0}^{N_{rf}} I_g\left(m_{lo}, m_{rf}\right) \exp\left(j\left(m_{lo}\omega_{lo} + m_{rf}\omega_{rf}\right)\right)$$

(3.2.42)

where $I_g\left(m_{lo}, m_{rf}\right)$ denotes the harmonic resistive current for $m_{lo}\omega_{lo} + m_{rf}\omega_{rf}$. The harmonic current of the device characteristic, $I_g\left(m_{lo}, m_{rf}\right)$ can then be obtained directly by Fast Fourier Transform of Equation (3.2.41):

$$I_g\left(m_{lo}, m_{rf}\right) =$$
$$\frac{1}{N_{lo}N_{rf}} \sum_{n_{rf}=0}^{N_{rf}-1} \sum_{n_{lo}=0}^{N_{lo}-1} q\left(m_{lo}, m_{rf}\right) I_G\left(V\left(\frac{2\pi n_{lo}}{N_{lo}}, \frac{2\pi n_{rf}}{N_{rf}}\right)\right) \times$$
$$\exp\left(j2\pi\left(\frac{m_{lo}n_{lo}}{N_{lo}} + \frac{m_{rf}n_{rf}}{N_{rf}}\right)\right)$$

(3.2.43)

where $q\left(m_{lo}, m_{rf}\right)$ is defined as:

$$q\left(m_{lo}, m_{rf}\right) = \begin{cases} 2 & \text{when } m_{lo} \neq N_{lo} \text{ and } m_{rf} \neq N_{rf} \\ 0.5 & \text{when } m_{lo} = 0 \text{ and } m_{rf} = 0 \\ 1 & \text{when } m_{lo} = N_{lo} \text{ or } m_{rf} = N_{rf} \end{cases}$$

(3.2.43)

Similarly, a 2-dimensional Fast Fourier Transform can be employed to decompose the charge equation. Suppose that the charge is nonlinearly related with voltage as follows:

$$Q_B = Q_0 + \sum_{r=0}^{N} \frac{(Q_{r+1} - Q_r)}{1 + \exp\left(\frac{V_r - V}{k}\right)}$$

(3.2.44)

where V_r denotes for the exact voltage at which the segments Q_{r+1} and Q_r intersect. Suppose that, following a substitution of the time domain voltage into Equation (3.2.44), the charge causing the reactive current in time domain is:

$$Q_B = Q_B\left(V\left(\omega_{lo}t, \omega_{rf}t\right)\right)$$

(3.2.45)

The discrete form of Equation (3.2.45) is:

$$Q_B = Q_B\left(V\left(\frac{2\pi n_{lo}}{N_{lo}}, \frac{2\pi n_{rf}}{N_{rf}}\right)\right)$$

(3.2.46)

Denote the harmonic index for the LO as m_{lo}, and the RF harmonic index, m_{rf}. As before, our goal in this exercise is to decompose the charge given in expression (3.2.46) into its harmonic components, that is:

$$Q_B = \sum_{m_{lo}=0}^{N_{lo}} \sum_{m_{rf}=0}^{N_{rf}} Q_c\left(m_{lo}, m_{rf}\right) \exp\left(j\left(m_{lo}\omega_{lo} + m_{rf}\omega_{rf}\right)\right)$$

(3.2.47)

where $Q_c\left(m_{lo}, m_{rf}\right)$ denotes the harmonic charge for $m_{lo}\omega_{lo} + m_{rf}\omega_{rf}$ and can directly be obtained by Fast Fourier Transform of Equation (3.2.46):

$$Q_c(m_{lo}, m_{rf}) = \frac{1}{N_{lo}N_{rf}} \sum_{n_{rf}=0}^{N_{rf}-1} \sum_{n_{lo}=0}^{N_{lo}-1} q(m_{lo}, m_{rf}) Q\left(V\left(\frac{2\pi n_{lo}}{N_{lo}}, \frac{2\pi n_{rf}}{N_{rf}}\right)\right) \times \exp\left(j2\pi\left(\frac{m_{lo}n_{lo}}{N_{lo}} + \frac{m_{rf}n_{rf}}{N_{rf}}\right)\right)$$

(3.2.48)

where $q(m_{lo}, m_{rf})$ can be found from Equation (4.2.43). The reactive current due to the nonlinear operations of the device capacitance can be determined by the time-derivative of Equation (3.2.47).

$$I_c = \sum_{m_{lo}=0}^{N_{lo}} \sum_{m_{rf}=0}^{N_{rf}} j(m_{lo}\omega_{lo} + m_{rf}\omega_{rf}) Q_c(m_{lo}, m_{rf}) \exp(j(m_{lo}\omega_{lo} + m_{rf}\omega_{rf})t)$$

(3.2.49)

Combining Equation (3.2.49) and Equation (3.2.42), we obtain the total current as:

$$I_T = I_G + I_c$$
$$\sum_{m_{lo}=0}^{N_{lo}} \sum_{m_{rf}=0}^{N_{rf}} \left[I_g(m_{lo}, m_{rf}) + j(m_{lo}\omega_{lo} + m_{rf}\omega_{rf}) Q_c(m_{lo}, m_{rf})\right] \times \exp(j(m_{lo}\omega_{lo} + m_{rf}\omega_{rf})t)$$

(3.2.50)

Now, to simplify our analysis, the higher order harmonics of the RF signal are assumed to be negligible in magnitude. Then Equation can similarly be simplified as:

$$I_T = I_G + I_c$$
$$\sum_{m_{lo}=0}^{N_{lo}} I_g(m_{lo}, 1) + j(m_{lo}\omega_{lo} + \omega_{rf}) Q_c(m_{lo}, 1) \exp(j(m_{lo}\omega_{lo} + \omega_{rf})t)$$

(3.2.51)

The conversion loss for a k th harmonic mixing in this instance can be approximately

determined by the ratio of IF power to the RF power, that is:

$$L = \left| \frac{Q_c(k,1)\left(I_g(k,1) + j\left(\omega_{rf} - k\omega_{lo}\right)Q_c(k,1)\right)V_k}{\left(I_g(1,1) + j\omega_{rf}Q_c(1,1)\right)V_0} \right| \tag{3.2.52}$$

To facilitate estimation of the mixing performance of a nonlinear device, a program to calculate the harmonic conductance and reactance has been developed in C++.

3.7. DISCUSSIONS AND CONCLUSIONS

In this chapter a general theory of sub-harmonic resistive mixing was presented. A qualitative treatment has been given to identify the significant effect of the location of the negative dynamic resistance regions; the voltage-independent conductance and capacitance intrinsic to a Quantum Barrier Device on weakly nonlinear harmonic mixing. Measurements of the mixing performance based on two devices of different current densities and layer structures have been given to substantiate our theoretical findings from this study. The experimental results, coupled with the analysis given in Section 3.4, reveals a hint on the figure of merits of a mixing device and also a number of factors for improving the intrinsic mixing performance of Quantum Barrier Devices. Namely, the linear conductance and the unbiased capacitance, both of which are voltage-independence, negatively affect the intrinsic mixing performance. At the device level, the conversion efficiency can be optimized by choosing a layer configurations that yield minimum voltage-independent conductance. Also, the NDR region should be drawn as close to the current-axis as possible if the intention is to minimize the LO power required to attain a minimum conversion loss.

The position of the NDR region is a function of the well width in the Quantum Barrier Device. It is possible to increase the well width during layer growth, thus drawing the NDR

region closer to the current-axis of the device I-V characteristic. On the other hand, the depletion layer, which is commonly employed to offset the unbiased capacitance, can also be used to control the device nonlinearities around the origin in the I-V characteristic. More research is recommended to perform further measurements to identify the effect of the device level nonlinearities, which are required for high-order sub-harmonic mixing with an optimal conversion efficiency and to understanding the layer structure factors that alter the carrier supply function. It is the author's impression that the Quantum Barrier Devices used in this work are still very far from Schottky devices in terms of linear efficient frequency-conversion. Nevertheless, the outcome of the research discussed herein should be highly beneficial to terahertz engineering, and pathe the way for further work into the use of the Quantum Barrier devices as efficient harmonic mixers.

REFERENCES

[1] N. F. Mott, "Note on the contact between a metal and an insulator or semiconductor," in *Proc. Cambridge Philosophical Soc.*, 1938, p. 568.

[2] J.-D. Buchs and G. Begemann, "Frequency conversion using harmonic mixers with resistive diodes," *IEEE J. Microwave Opt. Acoust.*, Vol. 2, pp. 71–76, May 1978.

[3] M. Cohn, J. E. Degenford, and B. A. Newman, "Harmonic mixing with an antiparallel diode pair," *IEEE Trans. Microwave Theory Tech.*, Vol. 23, pp. 667–673, Aug. 1975.

[4] S. A. Maas, *Microwave Mixers*, 2nd ed. Norwood, MA: Artech House, 1993.

[5] R. J. Malik and S. Dixon, "A subharmonic mixer using a planar doped barrier diode with symmetric conductance," *IEEE Electron Device Lett.*, Vol. 3, pp. 205–207, July 1982.

[6] G. Millington, R. E. Miles, R. D. Pollard, D. P. Steenson, and J. M. Chamberlian, "A resonant tunneling diode self-oscillating mixer with conversion gain," *IEEE Microwave Guided Wave Lett.*, Vol. 1, pp. 320–321, Nov. 1991.

[7] S. A. Mass, *Microwave Mixers*. Norwood, MA: Artech House, 1993, pp. 226–227.

[8] G. B. Tait, "Microwave mixers employing multiple-barrier semicon-ductor heterostructure

devices," *IEEE Trans. Microwave Theory Tech.*, Vol. 42, pp. 1596–1601, Sept. 1994.

[9] W. Y. Liu and D. P. Steenson, "18-to-1 GHz subharmonically pump downconverter using a quantum barrier device with symmetric conductance," *PREP*, Inst. Elect. Eng., U.K., Jan. 1999.

[10] R. A. Kiehl, T. C. L. G. Sollner, and H. C. Liu, "High-frequency resonant-tunneling devices in high-speed heterostructure devices," in *Semiconductors & Semimetals*, R. K. Willardson, A. C. Beer, and E. R. Weber, Eds. New York: Academic, 1994.

[11] W. Y. Liu and D. P. Steenson, "Investigation of Subharmonic Mixer Based on a Quantum Barrier Device," *IEEE Trans. On Microwave Theory and Techniques*, Vol., 48, No. 4, pp 757-763, April, 2000.

[12] W. Y. Liu and D. P. Steenson, "Demonstration of a Millimeter-Wave Sub-harmnonically excited Quantum Barrier Mixer," *SPIE, Terahertz Spectroscopy and Applications II*, pp 426-434, Jun, 1999.

[13] M. V. Schneider and W.W. Snell, Jr., "Harmonically pumped stripline-downconverter," *IEEE Trans. Microwave Theory Tech.*, Vol. MTT-23, pp. 271-275, Mar. 1975

[14] T. F. McMaster, M. V. Schneider, and W. W. Snell, "Millimeter-wave receivers with subharmonic pump," *IEEE Trans. Microwave Theory Tech.*, vol. MTT-24, no. 12, Dec. 1976

[15] E. R. Carlson and M. V. Schneider, "Subharmonically pumped millimeter-wave receiver," in *Dig. 4th Int. Conf. Infrared Millimeter Waves*, Dec. 10-15, 1979, pp. 82-83

[16] C. M. Mann, D. N. Matheson, and M. R. B Jones, "183 GHz double diode subharmonically pumped mixer," *Int. J. Infrared Millim. Waves*, vol. 10, no. 9, 1989

[17] P.H. Ostdiek, T. W. Crowe, and I. Galin, "Integration of an antiparallel pair of Schottky barrier diodes in millimeter wave mixers," in *Dig. 15th Int. Conf. On Infrared and Millimeter Waves*, Orlando, FL, Dec. 1990, pp. 401-403

[18] P. H. Siegel, R. J. Dengler, I. Mehdi, J. E. Oswald, W. L. Bishop, T.W. Crowe, and R. J. Mattauch, "Measurements on a 215-GHz subharmonically pumped waveguide mixer using planar back-to-back air-bridge Schottky diodes," *IEEE Trans. Microwave Theory Tech.*, vol. 41, no. 11, Nov. 1993

[19] D. G. Hayes, A. W. Higgs, P. J. Wilding and G. W. Smith, "CONVERSION GAIN AT 18 GHZ FROM RESONANT TUNNELLING DIODE MIXER OPERATED IN FUNDAMENTAL MODE", *Electronics Letters, IEE*, vol. 29, No. 15, 22nd July, 1993

[20] P.H. Siegel, R.P. Smith, S. Martin and M. Gaidis, "2.5 THz GaAs monolithic membrane-diode mixer", *IEEE Trans. Microwave Theory and Tech.*, Vol. 47, No. 5, May 1999, pp. 596-604.

[21] Michael C. Gaidis, Herbert M. Pickett, C. D. Smith, Suzanne C. Martin, R. Peter, and Peter H. Siegel, "A 2.5 THz receiver front end for spaceborne applications, " *IEEE Trans. Microwave Theory and Tech.*, Vol. 48, No. 4, April 2000, pp. 733-739.

[22] S.W. Moon, C.M. Mann, B.J. Maddison, I.C.E. Turcu, U. Allot, S.E. Hug, N. Lisi, "Terahertz waveguide components fabricated using a 3D X-ray microfabrication technique", *Electronics Letters*, Vol. 32, No. 19, pp-1794-1795, 12 Sept. 1996

Chapter 4: Planar Circuit Technology

4.1 INTRODUCTION

The generally preferred solution for implementing upper frequency millimeter wave circuits, at higher frequencies, is to use E-plane or finline circuits. E-plane circuits are planar metallized circuits placed across a rectangular waveguide. The metallized circuits are supported on a substrate.

A core technology for realizing low cost submillimeter-wave and terahertz systems is a volume planar technology. The majority of components operating at millimeter wave frequencies and beyond utilize non-planar waveguide structures in some form. Waveguide has been well-known for its low transmission loss, and is historically a well-characterized transmission medium. In fact, due to their superior optical efficiency, lower transmission line loss, and tuning flexibility, waveguide mixers have been found to yield better performance than quasi-optical mixers at frequencies where both have been constructed. However, as the operating frequency of a circuit increases, the electrical wavelength becomes increasingly small and the physical dimensions of the circuit need to shrink accordingly. At frequencies above 150 GHz waveguide becomes so small (less than 1 mm) that fabrication utilizing conventional machining and electroforming techniques becomes technically difficult, extremely expensive, or even impossible for some less-equipped institutions. At the time of this writing, just milling a simple copper block supporting WR-5 flange using a conventional CNC machine priced at around US$11,000 per piece. Motivated by this concern, we developed a number of polymer-based micromachining techniques that utilize the photosensitive resin (i.e. SU-8) to cost-effectively realize electronic components operating beyond 100 Ghz.

Micromachining is now gaining attention in the field of terahertz engineering as well as RFICs. Indeed, many micromachining techniques are being commercially employed in production of submillimeter wave components. Most of the existing micromachining techniques are extremely costly to undertake. To challenge this weakness, this chapter proposed a low-cost photo-micromachining techniques, with particular reference given to the polymer-membrane-supported transmission lines. The techniques were originally intended for tackling some problems associated with our CNC machine, but was unknowingly developed to be a competitive micromachining technology. The proposed thin photoresist micromachining techniques are not only robust on its own, but also combine the merits of various established machining techniques. This approach was originally intended for implementation of the millimeter wave mixer. This effort is part of the central theme of this dissertation: the development of enabling technology for millimeter-wave Quantum Barrier Subharmonic mixers.

4.2 MICROMACHINING IN GENERAL

Among a handful of the micromachining techniques, the most commonly employed are silicon based micromachining techniques involving polycrystalline silicon (i.e. polysilicon). Silicon microfabrication processes can be categorized as either a surface or a bulk micromachining process. In general, surface micromachining involves the sequential deposition and removal of thin film materials, and bulk micromachining involves the removal of material from the bulk of a silicon wafer. In realization of micromechanical parts, for example, surface micromachined devices are frequently fabricated from alternating polysilicon and silicon dioxide (oxide) thin films. These films, which are typically less than several microns thick, are deposited on the substrate through chemical vapor deposition. Between the deposition steps, the layers are patterned and etched to form the components of the desired device. The oxide layers are used to create spaces between the polysilicon structural layers. Finally, a hydrofluoric acid

(HF) etch is used to dissolve the oxide and release the mechanical polysilicon devices.

In the field of millimeter-wave (or submillimeter-wave) engineering bulk micromachining is frequently used to fabricate rectangular waveguide. The process entails both wet and dry etching. In wet etching, diluted potassium hydroxide (KOH) or KOH/IPA solutions are most commonly used. Micro-features are two-dimensionally etched using KOH/IPA solutions until the full waveguides are structurally formed. This micromachining technique allows precise three-dimensional structuring, etched cavities, thin membranes, through holes with excellent surface finish. However, the waveguide geometry is limited by the orientation of the crystalline planes. For example, cavities etched into <100>-oriented wafers feature inward sloping walls at an angle of 54.7 degrees. Trenches with vertical sidewalls can be etched into <110>-oriented wafers, but the shape and orientation of the trenches are constrained.

The non-vertical sidewall problems with wet-etching can be resolved by plasma-assisted dry etching, which allows etching trenches of arbitary sharp and orientation with vertical sidewalls. This has developed into a widespread bulk micromachining method. Deep reactive ion etching can be used to etch high-aspect-ratio vertical trenches in silicon with depths exceeding several hundred microns. The underlying principle of deep reactive ion etching is silicon removal by ion bombardment using the reactive gas SF_6. Deep reactive ion etching is performed by alternating reactive ion etch steps with "passivation" steps. During each passivation step, gaseous C_4F_8 is used to deposit a protective polymer film on trench sidewalls. The subsequent etch step removes the film preferentially from trench bottoms. As etching continues, the sidewalls are protected, allowing the creation of very deep trenches.

However, silicon etching of a non-orthogonal structure by either of the silicon micromachining techniques, is not as straightforward as milling by a numerically controlled machine. Silicon-etching cannot readily be used to make waveguide structures in which the height of the waveguide is stepped down (e.g. in an impedance transformer) or tapered (either rectangular or circular). This severely limits the types of structures that can be produced.

These problems are partially resolved by the recently developed laser machining technique [20,21] which operates independently of the crystal plane orientation and thereby permits a wide variety of structures to be made.

Laser etching is supreme in its accuracy and indeed it is being used by a few technology giants already. However, as yet, it fails to attract much attention in this fast growing industry. The main disadvantage of laser etching is that the initial cost of laser-etching equipment is considerable. Fortunately, cheap but reliable polymer-based micromachining technologies focused here have the potential to replace silicon-based micromachining techniques. One of the polymer-based micromachining techniques is based on the use of a photosensitive polymer in realization of 2-D or 3-D objects. The photosensitive polymer is an epoxy but its chemical properties are changed upon exposure to ultra-violet light. The exposed portion of photosensitive polymer undergoes cross-linking or scission, that is, chemical changes which either inhibit or promote solubility, respectively. If ultra-violet light exposure inhibits solubility, the polymer is said to be negative-imaged. However, if the ultra-violet light promote solubility, the resin is said to respond positively. IBM's SU-8 and DuPont Pyralin photosensitive polyimide are typical examples of negative photosensitive resin, while DOW 7000 series photosensitive BCB, and AZ's thick-film photoresist can be positive- or negative-imaged.

IBM's SU-8 was chosen for this work, primarily because of its being relatively cheap, its extremely high viscosity and high-precision control of the thickness up to 2 mm. The viscosity and thickness are conducive to microfabrication of high-precision micro-structures using conventional photolithograhical facilities. To fabricate a rectangular freestanding waveguide operating beyond 100 GHz [8,9], for instance, an ultra-thick version of SU-8 is first spin-coated onto an optically smooth surface. The pattern of the waveguide channel is photolithographically defined in 2-D using a photomask. Upon exposure to ultra-violet light, the exposed portions undergoes crosslinking, which renders it insoluble. The unexposed regions remain relatively soluble and can be removed by solvent development. The final curing step hardens the exposed portions, resulting in a ceramic-like 3-D structures. Since SU-8 is not a conducting material, the

waveguide walls need be coated with a layer of a good conductor through thermal evaporation, ion-sputtering or other more appropriate metalization techniques.

This SU-8 processing approach [8,9] is essentially surface-micromachining. Like silicon micromachining, the surface-micromachining with the ultra-thick SU-8 suffers from many physical limitations. Despite the fact that the maximum allowable thickness of the ultra-thick SU-8 approaches full waveguide height at W-band frequencies, the poor stability and swelling of microstructures developed from a chemically amplified resin may limit the ultimate structure size. The runny and semi-liquid nature of the resin can be prematurely deformed by heat before exposure to ultra-violet light. Thickness control is another problem in processing and sometime requires surface grinding or polishing. More importantly, it is still difficult to fabricate a closed waveguide requiring flange-to-flange interface with the exteriors.

In addition to the realization cost and the flanging problem, there exist other concerns that narrows our choice of micromachining methodologies. These concerns typically include:

1) minimization of transmission attenuation: Attenuation of a transmission line can be caused by conductor loss, dielectric loss as well as radiation loss. Conductor losses, resulting from finite conductivity, become less important at high frequencies as circuit dimensions shrink faster (inversely proportional to frequency) than the skin effect resistance increases (roughly proportional to the square root of frequency) provided that surface smoothness is not an issue. However, radiation loss and substrate-related losses increase considerably, particularly at millimeter-wave and submillimeter-wave frequencies. In part these losses are due to dielectric loss, which can be minimized by reducing the substrate thickness, but a significant source of loss is due to the excitation of surface modes and radiation losses. The radiation loss can be suppressed by enclosing the transmission media with a cover and walls or by appropriate choice of transmission line configuration. Surface excitation modes can also be eliminated by reducing the surface roughness of the planar transmission media.

2) relaxation of dimensional tolerances: Fabrication errors and certain physical factors contribute to variations in the characteristic impedance and relative permitivity of a transmission media. This problem is particularly serious beyond millimeter wave frequencies, when the guided wavelength is comparable to dimensional tolerances. It is difficult to incorporate arrangements for post-fabrication adjustments in planar components so that good dimensional tolerancing is critical. The tolerancing issue is relaxed if the guide wavelength is allowed to approach the free space wavelength. Fortunately, in micromachining, there exist a handful of techniques to enhance the similarity between the guide wavelength and the free-space wavelength, which, in turn, relaxes the dimensional tolerances and improve the design accuracies.
3) feasibility of active device integration: One of the source of design uncertainties comes from device-mounting onto a transmission media. Regardless of how a device is mounted, the bond between the device terminal and the transmission media should never be assumed as a perfect conductor without AC parasitics. Apparently, Microwave-Integration-Circuit (MIC) technology remains the only reliable solution to this problem.
4) dispersion: Dispersion of a planar transmission line is an unwanted effect due to the non-TEM mode propagation. Transmission media with air as the main dielectric substrate are, in general, less dispersive that those with substrate in other materials.

4.3 FLOW OF THE CHAPTER

In this Chapter, our first version of polymer microfabrication methodologies for polymer-based embedded waveguides and ultra-thin E-plane circuits are first introduced in Section 4.4. In Section 4.5, the fabrication technique for ultra-thin E-plane circuits is then extended to realization of membrane-supported coplanar waveguide. The empirical formula is derived for characteristic impedance of membrane-supported coplanar waveguide, and followed by a brief discussion on the relation between the membrane thickness and the leaky mode due to the finite aptitude of the membrane from the ground plane. In Section 4.6, the membrane micromachining technique discussed in Section 4.5 is further extended to another technology

that features low cost and self-supporting membrane-supported E-plane circuits. In Section 4.7, we will develop a novel and economical Copper-on-Membrane broad technology, with which a membrane-supported submillimeter wave planar components can be rapidly realized in the absence of any thermal processing. Finally, the chapter concludes with some proposed extensions of our existing polymer micromachining technologies.

4.4 EMBEDDED SUBMILLIMETER WAVE COMPONENTS USING PHOTOSENSITIVE RESIN MICROMACHINING

The first version of our micromachining techniques [11, 12] described here tackles the problems of surface-micromachining of the freestanding waveguide [8, 9]. It entails the use of a thin version of SU-8 for realization of planar finline circuits and non-planar embedded waveguides.

Fig. 4.4.1 shows one version of polymer-based embedded waveguide that has its structure totally housed inside a metal block that is conventionally milled. The metal block supports a photolithographically defined (micromachined) polymer waveguide that has the required tight tolerancing. Micro-features that cannot be mechanically machined can be photolithographically patterned and developed onto the embedded waveguide during the fabrication process. The metal block itself has been milled with standard flanges, thereby allowing the embedded waveguide to interface with other components. The development of this structure will now be described.

Although rectangular waveguide is a low-loss transmission medium, it is also an inflexible medium for integrating active devices. Planar integration technologies are preferred. The approach taken here is to incorporate an E-plane printed circuit containing the active device(s) into a rectangular waveguiding system. Both the E-plane printed circuit and the waveguide

were first fabricated using the thin version of the photosensitive resin, SU-8. Following this, the devices to be integrated were wire-bonded directly to the printed circuit. Fig. 4.4.1 illustrates an example of the E-plane circuits fabricated by us for submillimeter wave applications. Later, devices could be integrated into the E-plane circuits either using beam lead or a fully integrated approach.

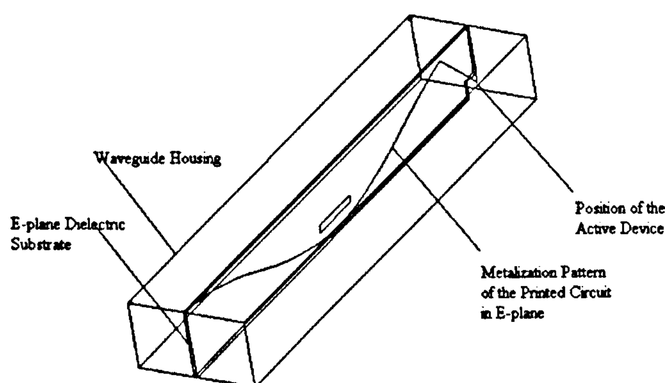

Fig. 4.4.1 An Example E-plane Circuit.

There are two components of this waveguiding system: a) microfabrication of the embedded rectangular waveguide; b) microfabrication of the E-plane circuit. The procedures for realizing these are described in the following sections.

4.4.1 MICROFABRICATION PROCEDURES OF EMBEDDED RECTANGULAR WAVEGUIDES

This section presents the procedures required to fabricate an SU-8 based waveguide for sub-millimeter applications. In realization of 3-D polymer structures such as rectangular waveguides, 2-D waveguide features are photolithographically defined and directly fabricated

onto an oversized waveguide channel in a metal block. In so doing, we can use the depth of the oversized channel to control the SU-8 layer thickness, thus avoiding any inaccuracy in thickness due to inaccurate spin speed and premature melting by heat. The support of the concave oversize channel also eliminates the need for an ultra-thick photoresist as opposed to the technique proposed in [8, 9]. In addition, since the metal block itself has been machined with all the standard flanges, it remains possible to maintain flange-to-flange interface to the exterior.

Basic Processing Procedures for a SU-8 Based Embedded-Waveguides

1. A metal block is first milled with the required flanges and an oversized waveguide channel (so-called pocket). See Fig. 4.4.2.1.
2. The SU-8 photoresist is then applied onto the oversized waveguide channel until the liquid form of the photoresist is just full, as shown in Fig. 4.4.2.2. The depth of the oversized waveguide channel as defined during the milling process determines the horizontal width of the SU-8 rectangular waveguide. (Further control of the depth of the oversized waveguide channel is feasible by pre-filling a layer of hardened SU-8 with predefined thickness.)
3. The whole metal block together with the SU-8 photoresist is prebaked, until the SU-8 liquid becomes sufficiently runny. Then let it cool down until the SU-8 photoresist changes to solid. With a solid SU-8 photoresist structure embedded into the oversized waveguide channel, the 2-D waveguide features are photolithographically defined and exposed to ultra-violet light for around 6 minutes, using a photomask. Then, the SU-8 filled metal block is post-baked for a few minutes to further harden the sample. Finally, unwanted SU-8 patterns are striped off with a standard SU-8 developer. After this step, the required waveguide features will be structurally formed, as shown in Fig. 4.4.2.3.
4. The metal block containing the fully developed waveguide structure is further baked for at least one hour
5. A layer of good conductor is ion-sputtered onto the inner lining of the waveguide channels.

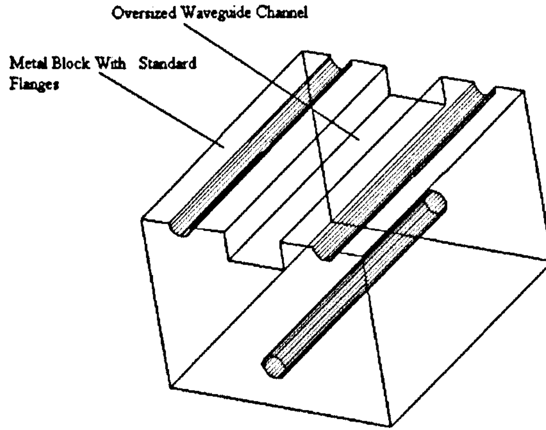

Fig. 4.4.2.1 A metal block, with an oversized waveguide channel.

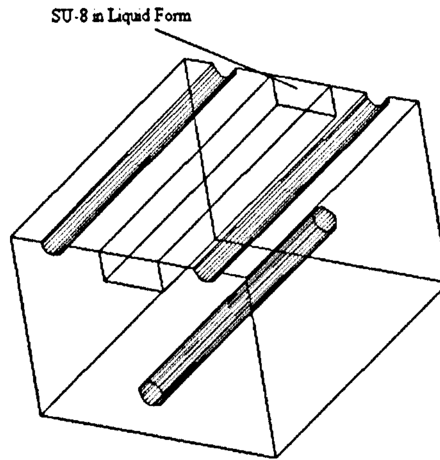

Fig. 4.4.2.2 Oversized waveguide channel filled with SU-8.

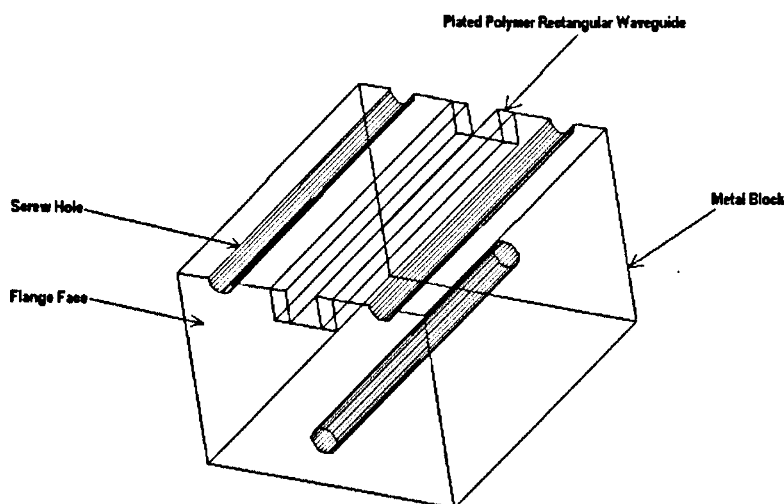

Fig. 4.4.2.3 Metal block with the required waveguide channel.

4.4.2 MICROFABRICATION PROCEDURES OF E-PLANE COMPONENTS

This section presents the procedures necessary to process an E-plane component using SU-8, which is to be incorporated into the waveguide realized in Section 4.4.1.

1. First a thin layer of silver is thermally evaporated as a sacrificial layer onto one side of a glass slide. This thickness of the sacrificial silver layer is not important. Then the metalization pattern of the printed circuit is evaporated directly onto the surface of sacrificial layer done in Step 2, preferably in gold or copper. See Fig. 4.4.3.1.
2. A layer of SU-8 is spun onto the surface with the metalization pattern. The spin-speed should be around 3500 rpm, such that the thickness of the SU-8 layer becomes no more than 50 microns. See Fig. 4.4.3.2.

3. The sample is pre-baked at 100 °C for around 10 minutes. Then, the substrate pattern is photolithographically defined and exposed using a photomask to ultra-violet light for about 2 minutes. Following the UV light exposure, the sample is post-baked for another 10 minutes at 100 °C. By soaking the sample in the SU-8 developer, the unexposed SU-8 photoresist pattern is striped off by soaking the sample in gamma-butyrolactone (GBL), leaving the sample as shown in Fig. 4.4.3.3.
4. The sample is finally soaked in iron III nitride solution, which etches away the silver sacrificial layer and removes the glass slide from the finline containing the printed circuit.

4.4.3 MEASUREMENTS OF WAVEGUIDE AND ULTRA-THIN POLYMER E-PLANE CIRCUITS AT W-BAND

S-parameter measurements of the SU-8 based waveguide have been carried out. S_{11}, which is used to quantify the electrical reflection of transmitted signal, was found to be below -20 dB for the whole frequency range of W-band (75 Ghz –110 Ghz).

The measured S-parameters, as shown in Fig. 4.4.3.4, suggest that the E-plane circuits realized with this technique are of very low transmission loss. The measured value of S_{21} (or S_{12}), which indicates the transmission attenuation between two ports, is no more than 1 dB, whereas the S_{11} (or S_{22}) is below -15 dB for the whole band. It is thought that the measured transmission attenuation was primarily due to the dielectric loss and because of the finite thickness of the substrate. The membrane work, discussed later, was aimed at further reducing such losses and would be necessary to increase the operating frequency further.

One of the promises of the technology developed here is that the very thin substrate layer on which the E-plane circuit is fabricated presents an effective permittivity which is very close to the free space permittivity. This can be examined by considering the relations of the guide wavelength to the free space wavelength. The guide wavelength was determined by measuring the resonant frequencies against different physical resonator lengths of the E-plane resonators

shown in Fig. 4.4.3.3.b. Fig. 4.4.3.5 shows a plot of guide wavelength versus free-space wavelength, which was obtained over a range of measurements on the finline resonators. For an SU-8 substrate of thickness=0.05 mm, the guide wavelength was found to be around 3/4 of the free-space wavelength.

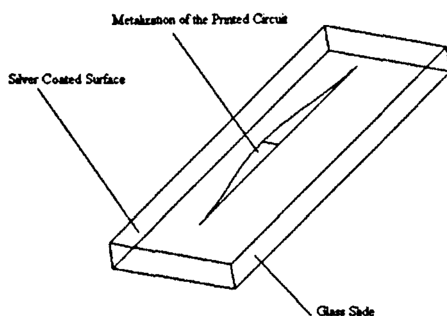

Fig. 4.4.3.1 A glass slide with metalization pattern on the silver coated surface.

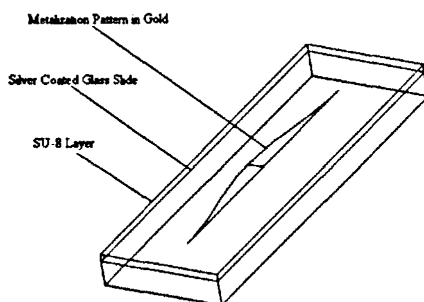

Fig. 4.4.3.2 Metalization pattern, topped with an SU-8 layer.

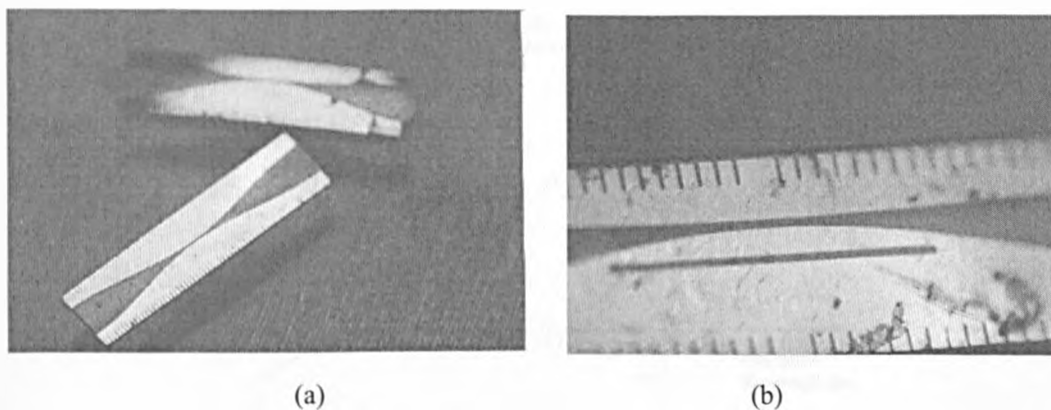

(a) (b)

Fig. 4.4.3.3 The finished samples after step 3: (a) Waveguide-to-finline transition; (b) Finline resonantor.

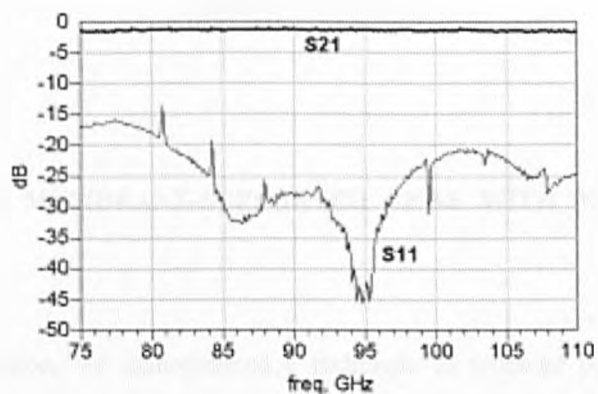

Fig 4.4.3.4 Measured performance of an E-plane transition realized on an SU-8 substrate with 0.05mm in thickness.

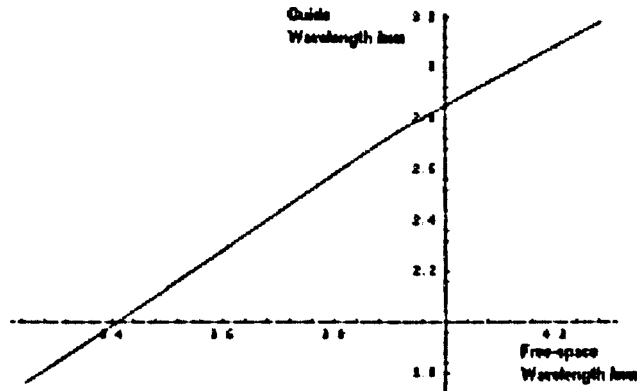

Fig 4.4.3.5 Measured guide wavelength versus free-space wavelength (SU-8 substrate thickness = 0.05 mm).

4.5 POLYMER MEMBRANE-SUPPORTED CPWS WITH MOUNTED ACTIVE DEVICES

In the previous section, we demonstrated a technique to fabricate polymer-based E-plane circuits with finite thickness of the dielectric substrate and polymer-based rectangular waveguides. This results in the effective permitivity being above the free-space permitivity, but the more important concern is that any thickness of the supporting membrane encourages surface modes. This section further extends the existing SU-8 micromachining technique in such a way that the guided wavelength of the E-plane circuit approaches to the free-space wavelength. Instead of having a printed circuit with finite SU-8 substrate thickness, the substrate thickness is minimized to its lowest limit in critical areas, ending up with a membrane-like dielectric substrate backing the printed circuit. Matching the guide-wavelength to free space wavelength enables the dimensional tolerance to be considerably relaxed in design of circuits operating at millimeter wave and sub-millimeter wave frequencies.

This section reports the fabrication of printed circuit lines on a 5 μm thick polymer membrane that minimizes dielectric loss and effectively eliminates surface modes, both of which are important for operation at millimeter-wave and submillimeter-wave frequencies. The relatively low-cost low-temperature process uses a photosensitive resin (SU-8) to form the polymer membrane and enables devices to be mounted on it at an earlier stage of the process.

4.5.1 LOSS AND DISPERSION CONSIDERATIONS

Loss in planar transmission media has metalic and substrate origins. Metallic losses, resulting from finite conductivity, become less important at high frequencies as circuit dimensions shrink faster (inversely proportional to frequency) than the rate at which the skin effect resistance increases (roughly proportional to the square root of frequency). However substrate-related losses increase considerably, particularly at millimeter-wave and submillimeter-wave frequencies. In part these losses are due to dielectric loss, but a significant source of loss is due to the excitation of surface modes. Dispersion is also a significant problem for some planar transmission line geometries. Dispersion and substrate-related losses are largely eliminated by fabricating the transmission lines on a silicon membrane [1–7]. These lines are also referred to as suspended stripline, or suspended coplanar waveguide (CPW), etc. This chapter demonstrates a technique that uses a thin polymer photosensitive resin to realize polymer-membrane-supported planar printed circuits to which active devices can be mounted. Measurements to 110 GHz show that CPW lines suspended on this membrane have low transmission losses in the millimeter-wave range.

4.5.2 POLYMER-MEMBRANE-SUPPORTED CPWS

Most membrane-supported transmission line fabrication uses micromachining of silicon [1–7]. Typically, a 3-layer $SiO_2/Si_3N_4/SiO_2$ supporting film is first deposited on to a high resistivity

bulk silicon substrate. The printed circuit is then photolithographically fabricated on the film. The bulk material underneath the film is then selectively etched and the supporting film is left as a membrane supporting the now suspended printed circuit. The performance of these membrane-based transmission lines is excellent [4–7, 19]. However, the processing approach based on the 3-layer $SiO_2/Si_3N_4/SiO_2$ film requires thermal oxidation and low pressure chemical vapor deposition (LPCVD). These approaches require extensive investment. The high temperature thermal processing also places restrictions on prior processing and on the materials used previously.

The low-cost process presented in this section eliminates the need for intensive thermal processing. The procedure uses a thin photosensitive polymer resin (EPON SU-8 or similar) [11, 12] spun on to a glass substrate to produce an polymer membrane that has been fabricated by us with a thickness of 5 μm and with an optically flat surface. The importance of our low-temperature thermal process is that it allows active devices to be mounted on an polymer membrane of controllable thickness before the final step removing the polymer membrane backing. The mechanical strength provided by the glass backing minimizes mechanical damage to the polymer membrane while the active device is mounted.

4.5.3 MICROFABRICATION PROCEDURES FOR POLYMER-MEMEBRANE-SUPPORTED CPWS

Realization of the structure has two parts: a) fabrication of the polymer membrane; and b) fabrication of a supporting frame.

A Fabrication of the Polymer Membrane

Metalization for the printed circuit is first patterned onto one side of a glass slide that is pre-coated with a sacrificial layer of silver. The active device to be integrated is then attached to the printed circuit face down. An ultra-thin layer of photosensitive resin (SU-8) is then formed (spun) on top of the printed circuit and this eventually becomes the supporting

membrane. A detailed description of the processing procedure, illustrated in Fig. 4.5.1, follows:

1. A microscope glass-slide, Fig. 4.5.1(a) is first coated with a layer of silver (or silver chloride), see Fig. 4.5.1(b). The silver layer (or the silver chloride layer) will be used as a sacrificial layer, and so the thickness is not important.
2. The printed circuit is then defined photolithographically and thermally evaporated with metal to a thickness satisfying skin depth requirements, see Fig. 4.5.1(c). The metalization is preferably gold for a silver sacrificial layer.
3. If a device is to be integrated with the printed circuit it is bonded directly onto the printed circuit using either chip-attach or, as in Fig. 4.5.1(d), wire bonding.
4. An ultra-thin layer of the photosensitive resin is sprayed on to the printed-circuit and the structure spun at high speed. Then, the whole wafer is pre-baked.
5. The membrane pattern is defined photolithographically and is annealed to form cross-linked polymers by exposure to ultra-violet light. The whole wafer is then post-baked to further harden the exposed dielectric membrane. The unwanted photo-sensitive resin pattern is striped off using polymer solvent γ -butyrolactone (GBL) leaving the patterned polymer membrane on top of the sacrificial layer.

If the polymer membrane is to be supported by a waveguide housing, for example, it can be released from the glass slide at this stage by wet-etching the sacrificial layer as shown in Fig. 4.5.1(e). Iron III nitride is used to etch a silver sacrificial layer and potassium hydroxide is used if the sacrificial layer is silver chloride.

B. Fabrication of the Membrane Supporting Frame

Under some circumstances it may be necessary to provide some mechanical support to the membrane. A supporting frame can be realized using a thickened region of resin. Below is a description of the processing procedure:

1. A thick layer (say 100 μm) of photosensitive resin (SU-8) is deposited on top of the polymer membrane.
2. On the top of this rectangular well is then assembled, see Fig. 4.5.2. The rectangular well serves as a container that maintains a bath of SU-8 of even depth.
3. A thin photosensitive resin (SU-8) is poured into the rectangular well and the whole structure is prebaked.
4. The supporting frame is then photolithographically patterned and the whole structure is post-baked until the resin is sufficiently hardened. An polymer solvent is used to remove the unexposed resin.
5. The membrane-based printed circuit together with the supporting frame is finally released from the glass slide by wet-etching the sacrificial layer.
6. The whole membrane-based printed circuit together with the supporting frame is finally removed from the glass slide by wet-etching the sacrificial layer.

Finally the printed circuit metal can be further thickened by electroplating, particularly if the evaporated metal fails to meet the skin depth requirements. The thickened metal strips also protect the polymer membrane from buckling.

4.5.4 EXPERIMENTAL RESULTS OF PLANAR MEMBRANE-SUPPORTED CPWS

A range of membrane-like printed circuits have been realized by us using the proposed methodology and Fig. 4.5.3 shows a range of membrane-supported CPWs. Fig. 4.5.4 illustrates one of the device-mounting techniques currently in use. Here the SU-8 layer underneath the device is deliberately thickened forming a pedestal. It was found that the weight of the device, silver-loaded epoxy and pedestal does not cause buckling of the polymer membrane for a span area up to 500 μm by 1000 μm. From S-parameter measurements, the membrane-supported CPW is found to be highly dispersive and the worst insertion loss is determined to be roughly 1.4 dB/mm under no cavity enclosure that suppresses the radiation loss to the free space. The attenuation measured in open-condition is not impressive, primarily

because the metalization thickness was only 200 nm, i.e. a thickness slightly below the skin depth of millimeter-wave frequencies. The dispersion and the losses as shown in this measurement will be explained qualitatively in next section.

The S-parameters shown in Fig. 4.5.5 are for an open 50 Ω. The line length was 1.55 mm, corresponding to a free-space half-wavelength of 93.55 Ghz. On the other hand, Despite the impedance mismatch due to the dielectric discontinuities at the ends of the 50 Ω line, the S_{11} was lowest around 93 GHz, suggesting that the relative dielectric constant is effectively close to unity.

4.5.5 QUALITATIVE TREATMENT OF MEMBRANE SUPPORTED CPWS

In this section, we qualitatively examine the losses and dispersion effects in membrane supported CPW, with the aim of developing an optimum membrane-based planar configuration. As will be demonstrated here, there is always a trade-off between the dispersion, dielectric loss and the radiation loss, which have not been considered in the beginning. Simply minimizing the membrane thickness to eliminate the dielectric-related losses can simultaneously increase the radiation loss due the leaky mode. To compromise the trade-off among all the effects, it is not sufficient to adopt the existing configuration of the membrane-supported CPW without modification. Thus, it is worthwhile to examine the available alternatives to optimize the overall transmission efficiency.

Quasi-static Transmission Line Characteristic of Membrane Supported CPW To understand the physical process involved in transmission losses of the membrane-supported CPW, a set of equations is derived for the quasi-static transmission characteristics. The most convenient approach is perhaps to apply the well-known analysis of multilayered CPW [14] to our membrane-supported CPW configuration. In this approach, the interface between two neighboring dielectric layer is treated as a magnetic wall that discourages the exchange of electric fields between these two dielectrics. An exact expression is then developed for the

characteristic impedance for C^a (when replacing all dielectric materials by air). With the expression for C^a, another expression is approximated for the effective dielectric constant ε_{re}.

The effective dielectric constant can be expressed as

$$\varepsilon_{re} = q_1\varepsilon_1 + q_2\varepsilon_2 + ... + q_n\varepsilon_n$$

(4.5.5.1)

with $q_1 + q_2 + ... + q_n = 1$. In Equation (4.5.5.1), q_1, $q_2 ... q_n$ represent respectively the filling factors for the dielectric region 1, 2, ... n and ε_1, ε_2...and ε_n are the relative dielectric constant of the materials used for region 1, 2, ... n. Using the notation of Fig. 4.5.6, the strip width of a coplanar waveguide under investigation is *2a*, and the gap is *b-a*. The general expression for q_i is

$$q_i = \frac{C^a_{si}}{C^a}$$

(4.5.5.2)

where C^a is the capacitance of the CPW configuration with air as dielectric and C^a_{si} is the capacitance of the substrate layer replaced by air as dielectric and is to be obtained using:

$$C^a_{si} = 2\varepsilon_o \frac{K(k_i)}{K^{'}(k_i)}$$

(4.5.5.3)

and

$$k_i = \begin{cases} \dfrac{a}{b} & \text{for the half plane} \\ \dfrac{\sinh(\pi a/2h)}{\sinh(\pi b/2h)} & \text{for a dielectric layer of thickness h} \\ \dfrac{\tanh(\pi a/2h)}{\tanh(\pi b/2h)} & \text{for a dielectric layer backed by a conductor} \end{cases}$$

(4.5.5.4)

$K(k_i)$ is the complete elliptic integral of the first kind of modulus k_i and $K'(k_i) = K(k'_i) = K\left(\sqrt{1-k_i^2}\right)$. The elliptic integral ratio $K(k_i)/K'(k_i)$ can be approximately expressed as [14]:

$$\frac{K(k_i)}{K'(k_i)} = \begin{cases} \dfrac{\pi}{\ln\left(2\left(1+\sqrt{\sqrt{1-k_i^2}}\right)/\left(1-\sqrt{\sqrt{1-k_i^2}}\right)\right)} & \text{for } 0 \le k \le 0.707 \\ \dfrac{1}{\pi}\ln\left(2\left(1+\sqrt{k}\right)/\left(1-\sqrt{k}\right)\right) & \text{for } 0.707 < k \le 0 \end{cases}$$

(4.5.5.5)

Consider Fig. 4.5.6, which illustrates the cross-section of our membrane-supported CPW configuration. In this case, C^a, the capacitance of the line with all the dielectric layers replaced by air, is exactly:

$$C^a = C^a_{s3} + C^a_{sx}$$

(4.5.5.6)

where $C^a_{s3} = 2\varepsilon_o \dfrac{K(a/b)}{K'(a/b)}$ and

$$C_{sx}^{a} = 2\varepsilon_o \frac{K\left(\dfrac{\tanh(\pi a/2(h_1+h_2))}{\tanh(\pi b/2(h_1+h_2))}\right)}{K'\left(\dfrac{\tanh(\pi a/2(h_1+h_2))}{\tanh(\pi b/2(h_1+h_2))}\right)}$$

(4.5.5.7)

The filling factor for the membrane is

$$q_2 = C_{s2}^{a} / C^{a} = \frac{C_{s2}^{a}}{C_{s3}^{a} + C_{sx}^{a}}$$

(4.5.5.8)

The filling factor for the upper half-plane is

$$q_3 = C_{s3}^{a} / C^{a} = \frac{C_{s3}^{a}}{C_{s3}^{a} + C_{sx}^{a}}$$

(4.5.5.9)

To calculate the filling factor of the space underneath the membrane, q_1, we make use of the relation that $q_1 + q_2 + \dots + q_n = 1$. For the membrane-supported CPW configuration, we have

$$q_1 = 1 - q_2 - q_3$$

(4.5.5.10)

Substituting Equation (4.5.5.8) and (4.5.5.9) into (4.5.5.10), we obtain:

$$q_1 = 1 - \frac{C_{s2}^{a}}{C_{s3}^{a} + C_{sx}^{a}} - \frac{C_{s3}^{a}}{C_{s3}^{a} + C_{sx}^{a}} = \frac{C_{sx}^{a} - C_{s2}^{a}}{C_{sx}^{a} + C_{s3}^{a}}$$

(4.5.5.11)

From Equation (4.5.5.1), the effective dielectric constant becomes:

$$\begin{aligned}\varepsilon_{re} &= \frac{C_{sx}^a - C_{s2}^a}{C_{sx}^a + C_{s3}^a} + \frac{C_{s2}^a}{C_{s3}^a + C_{sx}^a}\varepsilon_2 + \frac{C_{s3}^a}{C_{s3}^a + C_{sx}^a} \\ &= \frac{C_{sx}^a + C_{s3}^a - C_{s2}^a}{C_{sx}^a + C_{s3}^a} + \frac{C_{s2}^a}{C_{s2}^a + C_{sx}^a}\varepsilon_2 \\ &= 1 + \frac{C_{s2}^a}{C_{s2}^a + C_{sx}^a}(\varepsilon_2 - 1)\end{aligned}$$

(4.5.5.12)

where C_{sx}^a is given in Equation (4.5.5.7) and

$$C_{s2}^a = 2\varepsilon_o \frac{K\left(\frac{\tanh(\pi a/2h_2)}{\tanh(\pi b/2h_2)}\right)}{K'\left(\frac{\tanh(\pi a/2h_2)}{\tanh(\pi b/2h_2)}\right)}$$

(4.5.5.13)

Here, the effective dielectric constant ε_{re} is a function of the membrane thickness and the separation between the membrane and the ground plane. From Equation (4.5.5.12) the effective dielectric constant of the membrane-support CPW approaches to unity as the value of C_{sx}^a becomes dominant (or equivalently, the membrane is suspended far from the ground plane).

Dispersion The transmission characteristic derived in the previous section does not take the dispersion into account. The analysis in the previous section is strictly applicable at the lower end of microwave band. However, the membrane supported CPWs were found to be highly dispersive. The analysis in the previous section will not be valid if the condition that $h_1/\lambda << 1$ is not satisfied. Hence, Equation (4.5.5.12) alone cannot explain the measured S-parameters shown in Fig. 4.5.5. Fortunately, a simple expression to account for the effect of dispersion on the characteristic impedance and the dielectric constant is available [17]:

$$\sqrt{\varepsilon_{re}(f)} = \sqrt{\varepsilon_{re}} + \frac{\sqrt{\varepsilon_r} - \sqrt{\varepsilon_{re}}}{1 + \xi (f / f_{TE})^{-1.8}}$$

(4.5.5.14a)

where ε_{re} is the quasi-static value of ε_{re} and can be obtained directly from Equation (4.5.5.12). Other parameters of Equation (4.5.5.14a) are given as follows:

$$\xi = \exp(u \ln(2a/(b-a)) + v)$$

(4.5.5.14b)

$$u = 0.54 - 0.64p + 0.015p^2$$

(4.5.5.14c)

$$v = 0.43 - 0.86p + 0.54p^2$$

(4.5.5.14d)

$$p = \ln(2a/h)$$

(4.5.5.14e)

$$f_{TE} = \frac{c}{4h\sqrt{\varepsilon_r - 1}}$$

(4.5.5.14d)

f_{TE} given in Equation (4.5.5.14d) represents the cutoff frequency for the TE_0 surface wave mode for the substrate. For the membrane-supported CPW presented in this section, the equivalent values for h and ε_r can be respectively approximated as:

$$h = h_1 + h_2$$

(4.5.5.15)

and

$$\varepsilon_r = \sqrt{\frac{\varepsilon_{r2}(0)^2 h_2^2 + h_1^2}{h_2^2 + h_1^2}}$$

(4.5.5.16)

Hence, f_{TE} can be obtained by direct substitution of Equation (4.5.5.15) and Equation (4.5.5.16) into Equation (4.5.5.14d). Similarly, $\varepsilon_{re}(f)$ can be obtained by substituting Equation (4.5.5.16) and the newly obtained f_{TE} into Equation (4.5.5.14a). The simulated value of $\varepsilon_{re}(f)$ derived from this analysis was found to be in good agreement with the S-parameter measurement shown in Fig. 4.5.4, and, in fact, the agreement was found to be better than Agilent HFSS simulation. The author has also tested the derived $\varepsilon_{re}(f)$ by Agilent ADS simulation, although, at present, the analytical expression for the effect of dispersion on Z_0 is not available. As with conventional Coplanar lines, membrane-supported CPWs with smaller membrane height h_2 was found to be less dispersive due to the larger value of the cutoff frequency, f_{TE}.

Conductor Loss The attentuation of the above membrane-supported CPW can be due three origins: a) conductor loss; b) dielectric loss; c) radiation and surface losses. The metal thickness and the metal resistivity have direct impact on the conductor loss. Given that the CPW configuration is completely symmetric, the general formula of conductor loss of Ghione [15] is given here for completeeness as

$$\alpha_c = \frac{8.68 R_s \sqrt{\varepsilon_{re}}}{480\pi K(k_1) K'(k_1)(1-k_1)} \left\{ \frac{1}{a}\left[\pi + ln\left(\frac{8\pi a(1-k_1)}{t(1+k_1)}\right)\right] + \frac{1}{b}\left[\pi + ln\left(\frac{8\pi b(1-k_1)}{t(1+k_1)}\right)\right]\right\}$$

dB/unit length

(4.5.5.17)

where R_s and t are respectively the skin resistance and the metal thickness. ε_{re} can be obtained from Equation (4.5.5.12).

Dielectric Loss In the case of the membrane-supported CPW, the dielectric loss is mainly caused by the dielectric loss tangent of the membrane. The expression for the attenuation constant due to the dielectric loss in the membrane-supported CPW is the same as

that for a microstrip and the formula developed by Welch [18] is given here for completeness:

$$\alpha_d = 2.73 \frac{\varepsilon_r}{\sqrt{\varepsilon_{re}}} \frac{\varepsilon_{re}-1}{\varepsilon_r-1} \frac{\tan\delta}{\lambda_0}$$

(4.5.5.18)

Since the measured S-parameters clearly show that the effective guide wavelength is around unity, it is reasonable to assume that the dielectric constant is effectively unity and $\alpha_d \approx 2.73 \tan\delta / \lambda_0$. In this case, the attenuation constant due to the dielectric loss is mainly a function of the operating frequency and the loss tangent.

Radiation Loss and Surface Wave Loss One of the most important but neglected losses is the losses through the coupling of power to surface waves and through radiation from unwanted (parasitic) modes. Both of these losses contribute significantly to the total attenuation of the CPW beyond microwave frequencies. In a CPW with infinitely thick substrate, the parasitic mode refers to the odd mode but antiphase signals in the two slots. The parasitic mode can be excited at the waveguide discontinuities, leading to unwanted radiation loss. This problem can be lessened by maintaining symmetry of the discontinuities or by using air-bridges at regular intervals to equalize the parasitic mode in the circuit. In the conductor-backed CPW configuration, however, the parasitic mode is mainly the parallel plate waveguide mode. The parallel plate waveguide mode generates surface waves, which in turn leads to power leakage to the ground plane conductor. Theoretically, the power leakage occurs when the dominant waveguide mode of the CPW travels faster than the parasitic parallel plate waveguide mode, which is TEM in nature [10]. Hence, due to the negligible thickness of the membrane and a finite separation between the membrane and the ground plane, the present membrane-supported CPW configuration is unconditionally leaky.

Liu and Itoh [10] have demonstrated that leakage in a conductor-backed CPW can be controlled by adding another dielectric layer either as a superstrate on the top of the CPW metalization or as another substrate between the metalization plane and the original substrate. The dielectric constant and the dielectric thickness of this layer are chosen in such a manner

that the dominant CPW mode becomes slower than the parasitic parallel waveguide modes. As an example, consider Fig. 4.5.7, which shows an example non-leaky four-layered CPW structure recommended in [10]. In this configuration, the dielectric constants are intentionally chosen such that $\varepsilon_2, \varepsilon_3 >> \varepsilon_1, \varepsilon_4$. The dominant waveguide mode is largely dependent on the dielectric constants $\varepsilon_2, \varepsilon_3$, while the parasitic parallel plate modes on $\varepsilon_1, \varepsilon_4$. Because $\varepsilon_2, \varepsilon_3 >> \varepsilon_1, \varepsilon_4$, the effective dielectric constant of the dominant waveguide mode correspondingly becomes dominant over that of the parasitic parallel plate mode for certain dielectric thicknesses, h_2, h_3 and h_2, h_3. In this regard, the normalized phase constant of the dominant waveguide mode is much greater than that of the parallel plate mode, ending up with significantly less parallel plate wave excited at the discontinuity. In other words, the configuration shown in Fig. 4.5.7 becomes non-leaky.

Following on from the reasoning above, it is anticipated that a further improvement on the existing membrane-supported CPW is possible by converting it into a non-leaky configuration, as shown in Fig. 4.5.7. Instead of being left open, the existing membrane-supported CPW configuration can be covered with a upper ground plane, while the membrane suspending the metalization can be further coated with another layer of membrane on the top. The separation between the ground plane and the membrane can be adjusted to optimize the leaky mode loss and the dispersion effects. The required membrane thickness and the actual membrane separation from the ground can be obtained either by a computationally expensive full-wave analysis [10], which is somewhat beyond the scope of this chapter, or another more elegant approach [16].

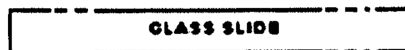

(a)

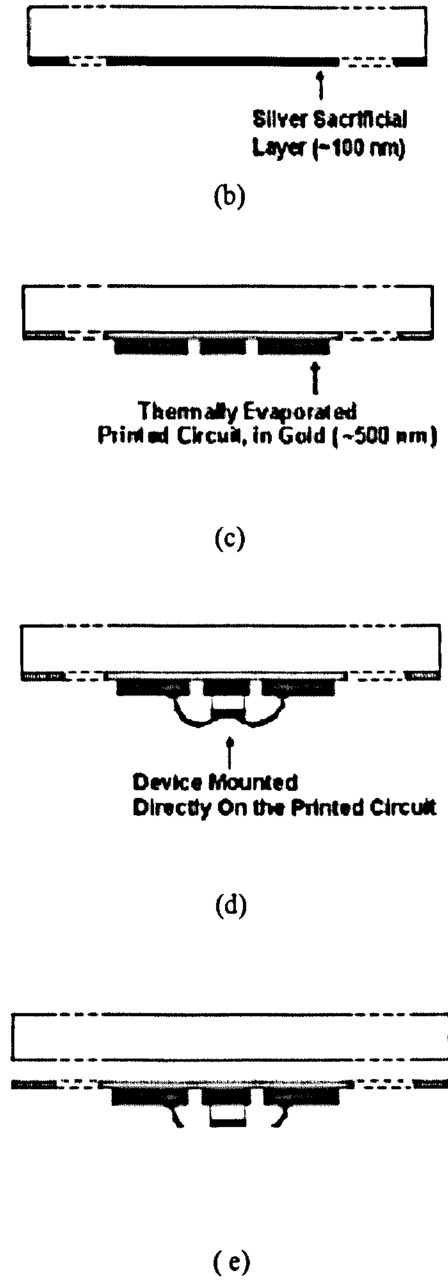

Fig. 4.5.1 Fabrication steps for a membrance-supported CPW with mounted active device.

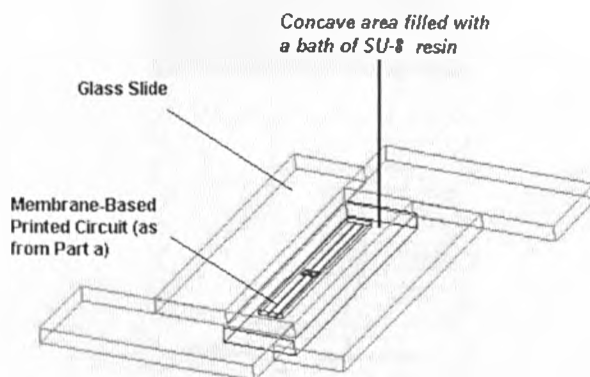

Fig. 4.5.2 A bath of thin photosensitive resin (SU-8), contained in a hand-assembled container formed using glass slides.

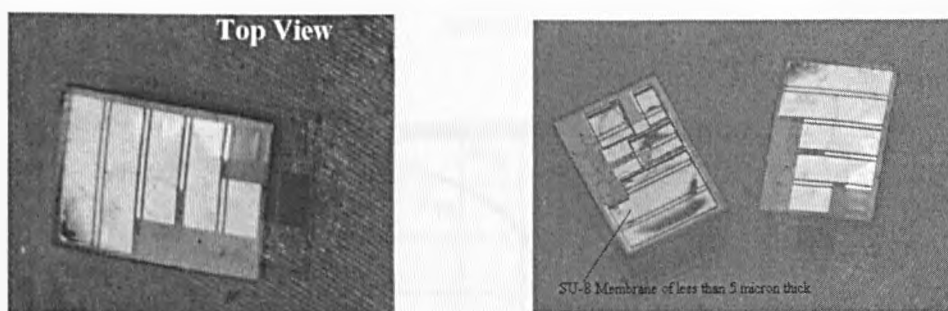

Fig. 4.5.3 Membrane-supported coplanar waveguides of different lengths (line width = 50 μm, gap = 40 μm, membrane thickness < 5 μm, membrane distance away from ground = 110 μm).

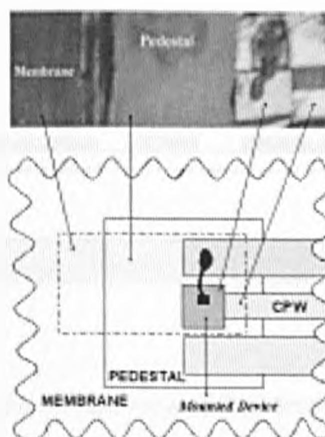

Fig. 4.5.4 Method of mounting a device onto a printed circuit supported by an polymer membrane (photo taken from the back-side of the membrane-supported coplanar waveguide test-set).

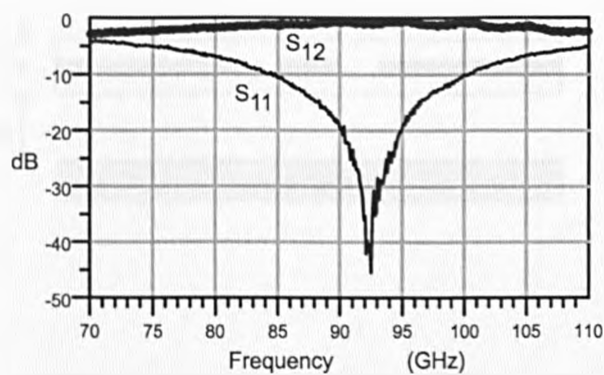

Fig. 4.5.5 Measured S-parameters for a 50 Ω membrane-supported CPW line. (metal thickness = 200 nm, line length = 1.55 mm).

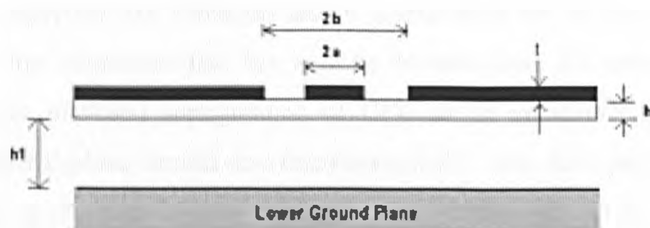

Fig. 4.5.6 Cross-sectional view of the Membrane-supported CPW.

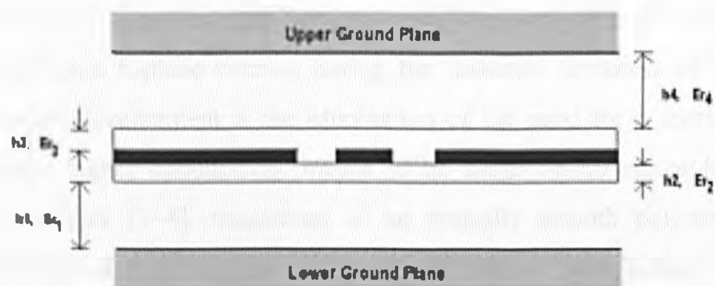

Fig. 4.5.7 Cross-sectional view of non-leaky CPW.($\varepsilon_2 = \varepsilon_3$, $\varepsilon_1 = \varepsilon_4$ and $\varepsilon_3, \varepsilon_2 > \varepsilon_4, \varepsilon_1$).

4.6 POLYMER-MEMBRANE-SUPPORTED COPPER E-PLANE CIRCUITS

In the previous section, polymer-membrane-supported CPW were demonstrated with

measurements and analytical treatments. Our measurement shows that membrane-supported CPW is highly dispersive and radiation loss is unavoidable for an open transmission line suspended on a thin membrane that has a finite distance from the ground plane. This section suggests an enclosed configuration of CPW as an improvement. We report the realization of copper E-plane circuits on a micromachined 5 μm thick polymer membrane. As the polymer membrane is both thin and optically smooth, dielectric loss and the excitation of surface modes are virtually eliminated. Unlike the previous approach, cheap and highly conductive copper is chosen for metalization with this process. Measured losses of lines are no more than 0.4 dB/cm at W-band. The relatively low-cost low-temperature process uses a photosensitive resin (SU-8) to form a self-supporting membrane to which devices can be mounted. The realization a finline resonator and an E-plane bandpass filter are presented.

In this section, we report here the further development of this process into another alternative technology: a process that features thick, low-cost silver or copper metalization yielding low resistance E-plane circuits having the dielectric thickness of no more than 5 microns. The major development is the elimination of the need for a sacrificial layer thus enabling relatively higher conductivity metals to be used. Unlike silicon-based membrane realization technologies [1–4], realization of an optically smooth polymer membrane as proposed in this section can be achieved using relatively low temperature processing. The procedure reported here uses a thin photosensitive polymer resin (EPON SU-8 or similar) [7,8] spun on to a silicon or glass slide to produce an polymer membrane that has been fabricated by us with a thickness of 5 microns and with an optically flat surface. Unlike Gold, which is soft and expensive, copper is sufficiently tough and relatively cheap to be thickened to make the resulting membrane self-supporting. Additionally, copper and SU-8 do not react so that copper metalization can be used. On the other hands, sandwiching the metal between two layers of polymer resin prevents oxidation.

The process also permits processing of multiple-layers and opening of interconnecting windows, thus enabling other variations of E-plane circuits to be formed. Active devices can be

mounted on the supported-membrane before the final step of membrane lift-off, and with all processing involving the active device carried out at low temperatures (at 90°C).

4.6.1 INSULATED/NON-INSULATED MEMBRANE-SUPPORTED E-PLANE CIRCUITS

The steps in the fabrication of insulated or non-insulated E-plane circuits are shown in Fig. 4.6.1. What follows is a description of the processing procedures in details.

1. The ultra-thin layer of photosensitive resin is first formed onto an optically smooth silicon slide, Fig. 4.6.1(a).

2. Metalization for the E-plane printed circuit is then deposited and patterned, Fig. 4.6.1(b). The metal is preferably copper or silver, both of which are highly conductive, and is thermally evaporated to a thickness enabling the whole fin to be self-supporting.

An active device can then bonded to the E-plane printed circuit as demonstrated in Section 4.6.2, Fig. 4.6.1(c).

3. Another thin layer of photosensitive resin is spun onto the top of the printed circuit, Fig. 4.6.1(d). This layer of resin, when left unexposed, can act as a temporary shield protecting the metalization from being attacked by the any etchant during the silicon removal and can be removed in the last stage to form a non-insulated E-plane circuits. Alternatively, this layer can be hardened by exposure to ultra-violet light so as to permanently form an insulated shield that can also facilitate DC-bias if the contact holes are present. This layer in both cases is typically 2 to 5 micron thick.

4. Next, the printed circuit is released by wet-etching the silicon slide with potassium hydroxide, Fig. 4.6.1(e).

6. The covering layer of photosensitive resin formed in step 4, if unexposed, can be finally striped off using polymer solvent gamma-butyrolactone (GBL) to form a non-insulated E-plane circuit, as shown in Fig. 4.6.1(f). Otherwise, the final E-plane circuit is insulated.

4.6.2 MEASUREMENTS OF INSULATED POLYMER-MEMBRANE-SUPPORTED E-PLANE CIRCUITS

A range of membrane-supported E-plane circuits have been realized on an polymer membrane of thickness around 8 μm, and two are described here: a finline resonator, and an E-plane bandpass filter. From a series of S-parameter measurements on these circuits, the transmission loss was found to be less than 0.4 dB/cm across W-band. Both insulated and non-insulated E-plane circuits exhibit similar performance, presumably due to the dielectric effects being negligible.

A finline resonator, as shown in Fig. 4.6.2, is mounted on one side of the split block waveguide. Fig. 4.6.3 presents the experimental characterization on a finline resonator. The Q-factor of the resonator, as reflected by the S_{21} of Fig. 4.6.3, is more than 100.

Fig. 4.6.5 presents the S-parameter measurement of an E-plane bandpass filter, shown in Fig. 4.6.4 with a passband insertion loss is around 0.5 dB.

The guide wavelength was found to be very close to the free space wavelength, suggesting that the dielectric effects on the E-plane circuit is virtually negligible. More importantly, matching the guide wavelength to the free-space wavelength considerably relaxes dimensional tolerances.

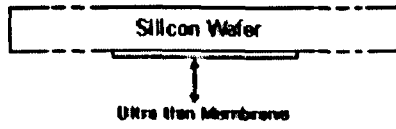

(a)

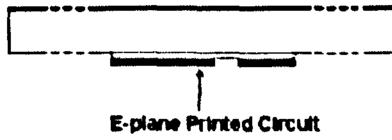

(b)

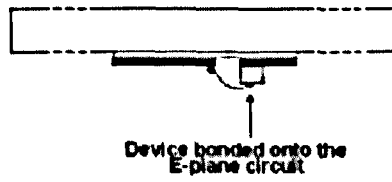

(c)

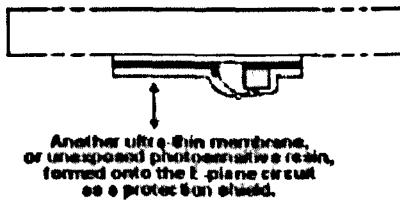

(d)

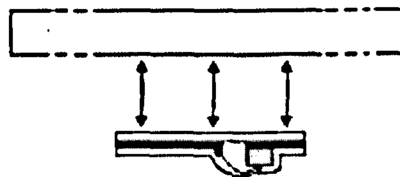

(e)

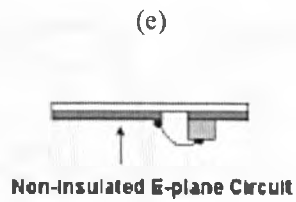

(f)

Fig. 4.6.1 Fabrication steps of insulated membrance-supported E-plane circuits with a mounted active device.

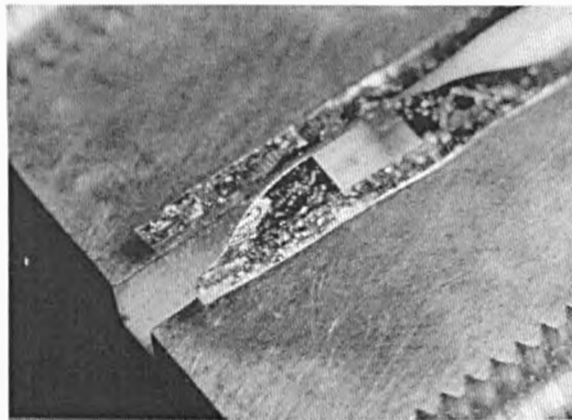

Fig. 4.6.2 Photograph of finline resonator of length 1.8 mm shown mounted in half of a split block waveguide, with metalalization of 5 microns thick

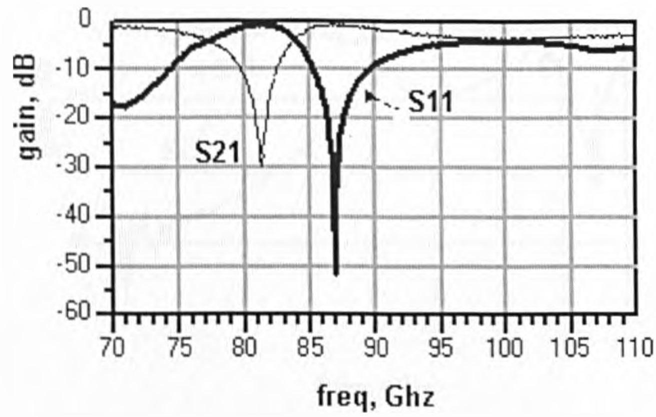

Fig. 4.6.3 Measured S-parameters of a finline resonator , with resonant frequency = 81.5 GHz, resonator length = 1.8 mm.

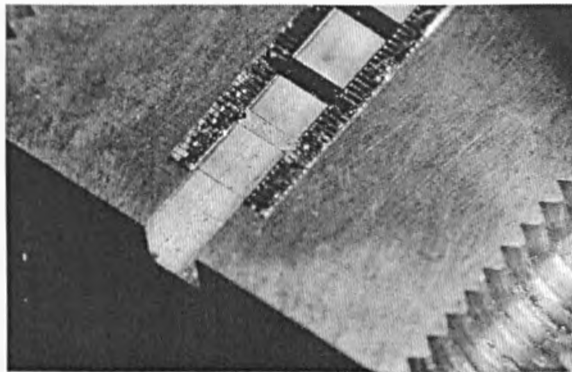

Fig. 4.6.4 Photograph of E-plane ladder bandpass filter shown mounted in half of a split block waveguide, with metalization thickness = 5 μ m.

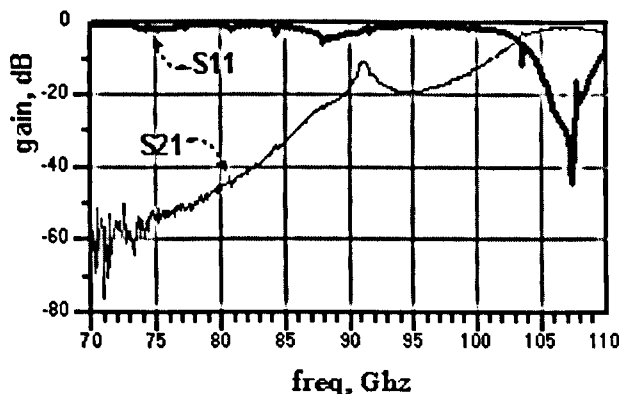

Fig. 4.6.5 Measured S-parameters of a bandpass filter with passband frequency centered at 107 GHz.

4.7 COPPER-ON-POLYMER-MEMBRANE BOARDS

In the previous section, membrane-supported copper E-plane circuits are discussed in some length, with a demonstration on its low loss properties. However, the micromachining technique previously discussed is not the cheapest alternative available. This section further presents another simpler and more economical processing technique for mass-production of self-supporting membrane-based printed circuits. Based on a pre-processed copper-on-membrane board, a membrane-based planar component can be rapidly realized on a 5 μm thick polymer membrane with conventional clean room facilities. The technology requires no thermal processing and is suitable for mass production of millimeterwave or submillimeter-wave components. Transmission losses of these membrane-supported E-plane components are typically less than 0.5 dB/cm. The simplicity of the process is comparable to etching a Duriod-supported printed circuit.

This section expands on the micromachining technologies that we have. Previous work has demonstrated an economical low temperature approach suited to realizing planar circuits

supported on polymer membranes. This section extends these concepts to present a technology analogous to printed wiring boards (PWBs) for E-plane millimeter-wave and submillimeter-wave circuits supported on membrane in waveguide. Boards can be prefabricated and stored and used as required in much the same manner as PWBs are.

4.7.1 MASS PRODUCTION OF PRINTED CIRCUITS USING COPPER-ON-MEMBRANE BOARDS

In the process described in the previous section, the printed circuit is metalized using either thermal evaporation or ion-sputtering, both of which are not only time-consuming, but also difficult to carry out in a nonspecialized or production-oriented laboratory. In this section the use of a pre-processed copper-on-membrane board to realize an polymer-membrane-based component is proposed. This copper-on-membrane board technology enables a membrane-supported printed circuit to be repeatedly produced on an optically smooth polymer membrane of no more than 5 μm thick without requiring thermal processing.

The copper-on-membrane board takes the form of Fig. 4.7.1 where the board is pre-coated with a (possibly thick) conducting layer. In this case the conducting layer consists of copper of around 5 to 10 μm thickness and a thin silver layer as an oxidation shield. Unlike gold, copper is relatively cheap and sufficiently tough to enable the final membrane-supported printed circuit to be self-supporting. The copper layer is completely encapsulated between the shielding layer (i.e. silver) and the polymer membrane, thus avoiding any chemical interaction with the surroundings, including oxidation. The blank copper-on-membrane boards mounted on a glass slide can now be stored for subsequent processing when the metal is patterned to realize a planar circuit.

Referring to Fig. 4.7.1, underneath the shielded copper layer is an ultra-thin layer of polymer membrane of around 5 μm thickness. The material of the membrane can be SU-8, thick

film photoresist, or photosensitive polyamide. The geometry of the membrane can be manually tailored under a microscope. Since the membrane itself is sufficiently thin, minor inaccuracies in cutting the membrane will not severely affect the overall circuit performance at millimeter wave or sub-millimeter wave frequencies. Between the conducting layer and the glass slide is a removable seed layer — a layer of soluble polymer substance, such as a layer of hardened positive photoresist. The final printed circuit together with the tailored membrane can be lifted-off the glass slide by simply dissolving the seed layer with a suitable polymer solvent.

What follows summarizes the procedures to fabricate planar circuits on a pre-processed copper-on-membrane board:

1. Metalization of the printed circuit is photolithographically defined and then etched in a breaker of heated and strongly agitated Iron III Nitride solution, Fig. 4.7.2(a).
2. Active devices, if necessary, are either wire-bonded or chip-attached onto the printed circuit.
3. The membrane is then manually tailored under a microscope to the design specification, Fig. 4.7.2 (b).
4. The membrane together with the printed circuit is then lifted-off the glass slide, by soaking the whole wafer in an polymer solvent such as acetone, Fig. 4.7.2 (c).

The required membrane-supported printed circuit may be mounted in a waveguide or a planar supporting frame. The waveguide or the supporting frame can be fabricated using polymer-based microfabrication as described previously [10].

4.7.2 EXPERIMENTAL RESULTS OF COPPER-ON-MEMBRANE BOARDS

Fig. 4.7.3 shows two waveguide-to-finline transitions mounted in cascaded in the E-plane (across the short dimension) of a W-band waveguide fabricated as split blocks also using polymer-based micromachining [10]. Measurements in Fig. 4.7.4 indicate a loss of around 0.4

dB per transition across W-band with a return loss around 20 dB or better. The transmission loss was found to be typically less than 0.45 dB/cm across W-band. The guide wavelength in all cases was found to be very close to the free space wavelength, suggesting that the dielectric effects on the E-plane circuit are virtually negligible. More importantly, matching the guide wavelength to the free-space wavelength considerably relaxes dimensional tolerances.

4.7.3 FURTHER EXTENTIONS OF THE EXISTING MEMBRANE BOARD TECHNOLOGY

The Copper-on-Membrane board technology and the polymer micromachining previously mentioned are not a mature progress in microfabrication, and there are many aspects that require improvements. In this section, we outline the following improvements to perfect the existing polymer membrane technology.

Alternative Version of Copper-on-Membrane Board. The copper-on-membrane board depicted in Fig. 4.7.1 is not the only version possible. Other variations can be formed with minor changes in processing. For instance, if the photosensitive polymer membrane and the silver layer are interchanged in position, and if the photosensitive polymer membrane has not been exposed to ultra-violet light, it is possible to fabricate double-sided planar components, high-Q E-plane resonators and even electromagnetic bandgap structures.

Alternative Membrane Materials. As with silicon rubber and conventional polyimide, the coefficient of thermal expansion of the photosensitive resin (e.g. SU-8) is larger than that of metals, see Table 4.7.4.1. The effect of thermal expansion in a substrate contributes to variation of the characteristic impedance and effective permitivity of a transmission line. One solution to this problem is to replace SU-8 with a photosensitive polyimide that is chemically based on a low thermal expansion polyimide, Polyimide should have a hardness comparable to conventional polyimide, but its coefficient of thermal expansion is relatively small. Similar to SU-8, the properties of a photosensitive polyimide are chemically changed upon exposure to

UV-light. The exposed portion of the polyimide undergoes crosslinking or scission chemical changes, depending on whether the polyimide is positive-imaged or negative-imaged. For the former, ultra-violet light exposure inhibits solubility. For a positive photosensitive polyimide, ultra-violet light exposure promotes solubility.

Table 4.7.4 The thermal expansion coefficient (TCE) for different materials

Material	Temperature Coefficient of Expansion (TCE)
Silicon Rubber	$>10^{-4}$
Epoxy Resin (eg. SU-8)	$\sim 10^{-4}$
Conventional Polyimide	$\sim 2\times 10^{-5}$
Metals	$\sim 1\times 10^{-5}$
Low Thermal Expansion Polyimide	$\sim 10^{-5}$
Ceramics (SiO_2,Si_3N_4, SiC, Al_2O_3)	$\sim 10^{-6}$

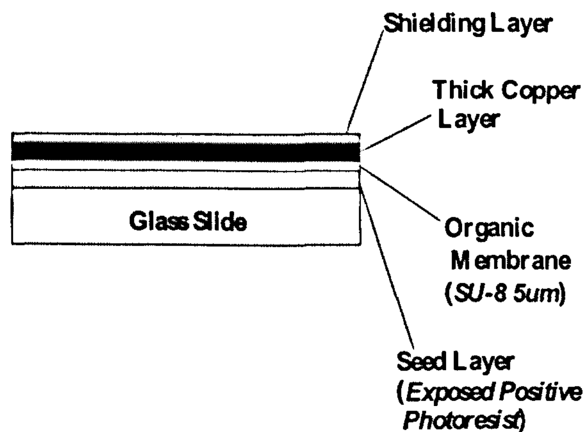

Fig. 4.7.1 Cross sectional view of single-sided Copper-on-Membrane board.

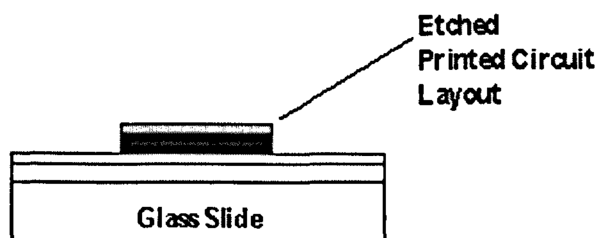

(a)

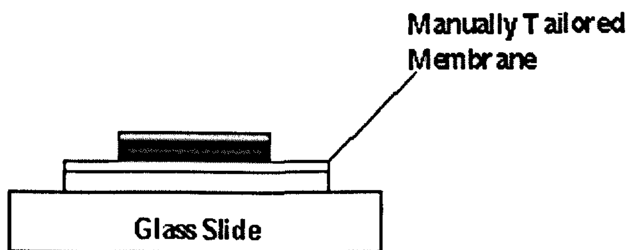

(b)

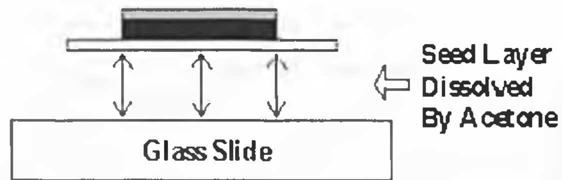

(c)

Fig. 4.7.2 Steps for realization of membrane-based printed circuit from a Copper-on-Membrane board of Fig. 4.7.1.

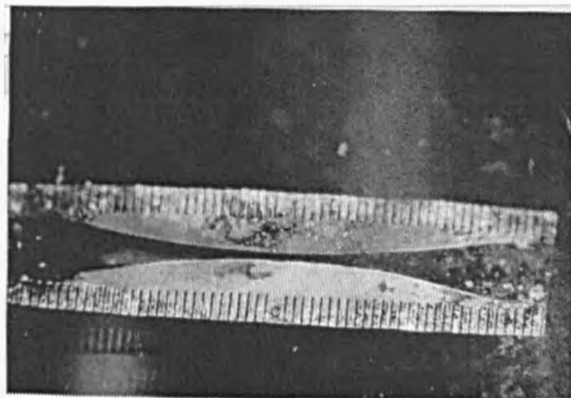

Fig. 4.7.3 A pair of back-to-back membrane-supported finline-to-waveguide transitions.

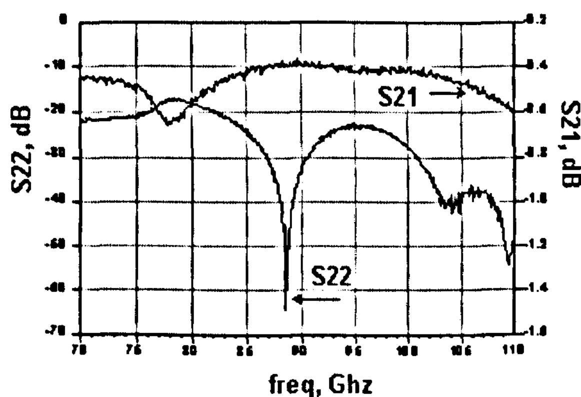

Fig. 4.7.4 Measured S-parameters of the two finline-to-waveguide transitions connected back-to-back.

4.8 CONCLUSIONS

This chapter has critically reviewed some existing micromachining techniques specific for applications in millimeter-wave and submillimeter-wave engineering. A number of novel polymer-based micromachining techniques were developed with an analysis of loss leading to design optimization. These polymer-based micromachining techniques are listed as follows:

1) A low-cost technique to fabricate a polymer-based embedded waveguide with standard flanges. In processing a polymer-based embedded waveguide, a pair of metal blocks, each with an over-sized channel, are first mechanically machined. Micro-features that cannot be mechanically machined can be photolithographically patterned onto the oversized waveguide channel, thus enabling an embedded waveguide to be formed. The final structure can be connected to the exterior via standard milled flange-to-flange interface without damaging the embedded waveguide.
2) A low-cost microfabrication technique that enables a printed circuit to be lithographically fabricated on an polymer membrane of controllable thickness. The method eliminates the

need for high-temperature thermal processing and allows active devices to be integrated without damaging the polymer membrane. A frame of thickened resin provides mechanical stability by maintaining the polymer membrane in tension enabling it to be self-supporting. It has been experimentally demonstrated that the technique can be used to realize low-loss conventional planar membrane-supported printed circuits.

3) A simple and low cost microfabrication method that enables E-plane circuits to be rapidly realized using polymer-based processing. The final membrane-supported E-plane circuits are both optically smooth and self-supporting. It has been experimentally demonstrated that the technique can be used to realize low-loss membrane-supported E-plane components for millimeter wave and frequencies and can be extended to submillimeter-wave frequencies.
4) A simple copper-on-membrane board technology enabling a membrane-supported printed circuit to be rapidly realized on a 5 μm thick membrane. Membrane-supported planar circuits can be easily implemented in this technology with conventional clean-room facilities without requiring thermal processing. The final membrane-supported components are both optically smooth and self-supporting. It has been experimentally demonstrated that the transmission losses of components in all polymer-membrane micromachining technologies are around 0.5 dB/cm.

These fabrication technologies are suited to the low cost productuion of planar active millimeter wave, submillimeter-wave and terahertz circuits. They are suited to the production of one-off circuits (method 4) or volume circuits (metods 2 and 3) mounted in a micromachined waveguide (method 1).

REFERENCES

[1] V. M. Lubecke, K. Mizuno, and G. M. Rebeiz, "Micromachining for terahertz applications," *IEEE Trans. Microwave Theory Tech.*, Vol. 46, pp. 1821–1831, Nov. 1998.

[2] R. M. Henderson, and L. P. B. Katehi, "Silicon-based micromachined packages for high-frequency applications," *IEEE Trans. Microwave Theory Tech.*, Vol. 47, pp.

1563–1569, Aug. 1999.

[3] M. Stotz, G. Gottwald, H. Haspeklo, and J. Wenger, "Planar millimeter-wave antennas using SiNx-membranes on GaAs," *IEEE Trans. Microwave Theory Tech.*, Vol. 44, pp. 1593–1595, Sept. 1996.

[4] G. Sajin, E. Matei, M. Dragoman, "Microwave straight edge resonator (SER) on silicon membrane," *1999 IEEE MTT-S Int. Microwave Symp. Digest*, pp. 283–286, June 1999.

[5] J. E. Harriss, L. W. Pearson, X. Wang, C. H. Barron, Jr., and A.-V. Pham, "Membrane-supported Ka band resonator employing polymer micromachined packaging," *2000 IEEE MTT-S Int. Microwave Symp. Dig.*, pp. 1225–1228, June 2000.

[6] W. Y. Liu, D. P. Steenson and M. B. Steer, "Membrane-Supported Copper E-plane Circuits," *2001 IEEE MTT-S Int. Microwave Symp. Dig.*, May 2001.

[7] W. Y. Liu, D. P. Steenson and M. B. Steer, "Membrane-supported CPW, with Mounted Active Devices," *IEEE Microwave and Guided Wave Letters*, Apr 2001

[8] C. E. Collins, R. E. Miles, G. M. Parkhurst, J. W. Digby, H. Kazemi, J. M. Chamberlain, R. D. Pollard, N. J. Cronin, S. Davies, J. W. Bowen, and D. P. Steenson, "Use of novel photoresists in the production of submillimetre wave integrated circuits," *4th Int. Conf. on Millimeter and Submillimeter Waves and Applications, SPIE,* pp. 108–109, July 1998.

[9] J. W. Digby, C. E. McIntosh, G. M. Parkhurst, B. M. Towlson, S. Hadjiloucas, J. W. Bowen, J. M. Chamberlain, R. D. Pollard, R. E. Miles, D. P. Steenson, L. S. Karatzas, N. J. Cronin, and S. R. Davies, "Fabrication and characterization of micromachined rectangular waveguide components for use at millimeter_wave and terahertz frequencies", *IEEE Trans. Microwave Theory Tech.*, Vol. 48, pp. 1293–1302, Aug 2000.

[10] Y. Liu, K. Cha and T. Itoh, "Non-Leaky Coplanar (NLC) Waveguides with Conductor Backing", *IEEE Trans. Microwave Theory Tech.*, Vol. 43, pp. 1067–1072, May 1995.

[11] W. Y. Liu, D. P. Steenson and M. B. Steer, "A Simple but Novel Technique of Micormachining for Millimeter Wave and Submillimeter Wave Applications, *IWMF'2000* Workshop, Oct. 9-10, 2000.

[12] W. Y. Liu, "Novel Technique of Thin Photoresist Micromachining for Submillimeter Wave Circuits," *SPIE*, Vol 4176-28, September 2000

[13] W. Y. Liu, D. P. Steenson and M. B. Steer, "Mass-Produced Copper-On-Membrane Board for Millimeterwave Circuits," Submitted to *IEEE MTT-S.*

[14] Bedair, S. S., and I. Wolff, "Fast, Accurate and Simple Approximate Analytic Formulas for Calculating the Parameters of Supported Coplanar Waveguides, " *IEEE Trans. MTT*, Vol. MTT-40, pp. 41-48, 1992

[15] Ghione, G., "A CAD-Oriented Analytical Model for the Losses of General Asymmetric Coplanar Lines in Hybrid and Monolithic MICs," *IEEE Trans.*, Vol. MTT-41, 1993, pp. 1499-1510.

[16] K. Beilenhoff and W. Heinrich, "Parasitic Parallel-Plate Line Mode Coupling at Coplanar Discontinuities," Microwave Symposium Digest, 1997., *IEEE MTT-S International*, Volume: 3 , 1997

[17] Hasnain, G., et al., "Dispersion of Picosecond Pulses in Coplanar Transmission Lines," *IEEE Trans.*, Vol. MTT-34, 1986, pp. 738-741

[18] Welch, J.D., and H.J. Pratt, "Losses in Microstrip Transmission Systems for Integrated Microwave Circuits," *NEREM Rec.*, Vol. 8, pp. 100-101, 1966

[19] L.K. Seidel and T.W. Crowe, "Fabrication and Analysis of GaAs Schottky Barrier Diodes on Thin Membranes for Terahertz Applications," *Int. J. IR and MM Waves*, Vol. 10, No. 7, July 1989.

[20] S. Nolte, C. Momma, G. Kamlage, B.N. Chichkov, A. Tunnermann, F. von Alvensleben, and H. Welling, "Micromachining with femtosecond lasers", *Lasers and Electro-Optics, 1998, CLEO 98. Technical Digest. Summaries of papers presented at the Conference on*, pp. 510-511, 1998.

[21] M.C Gower, "Industrial Applications of Pulsed Laser Micromachining", *Lasers and Electro-Optics Europe, 1998, 1998 CLEO/Europe. Conference on*, pp. 247-247, 1998

[22] H. Helvajian, "3D laser micromachining, microthrusters and nanosatellites", *Lasers and Electro-Optics, 1999. CLEO '99. Summaries of Papers Presented at the Conference on*, pp. 512, 1999

Chapter 5: Design and Measurement of QBD Mixer/multiplier

5.1 INTRODUCTION

The modeling techniques for Quantum Barrier Devices and the general theory of subharmonic mixing have been discussed in Chapter 2 and Chapter 3. The basic implementation issues have also been covered in Chapter 4. In this Chapter, the previous theoretical and practical considerations are applied to the design of a 18-to-1 Ghz subharmonically pumped (QBD) mixer, and a 10-to-100 Ghz (QBD) multiplier. The 18-to-1 Ghz subharmonically pumped mixer was introduced in Chapter 3. Instead of discussing the non-Schottky behavior presented in Chapter 3 however, the focus of this chapter is on its general mixing performance. Conversion efficiency in each case was measured and compared with the simulated performance based on the model presented in Chapter 2. Noise measurement at microwave frequencies has also been performed using the 18-to-1 Ghz QBD mixer. Possible alternatives to improve on the overall mixing performance are also studied with reference to the analysis given in Chapter 3.

5.2 QBD DOWN-CONVERTER FROM 18 GHZ TO 1 GHZ USING A QUANTUM BARRIER RESONANT TUNNELING DIODE WITH ANTI-SYMMETRIC CONDUCTANCE.

In this section, we present a successful realization of a Quantum-Barrier-Device-based mixer [1,2,3] that subharmonically down-convert a 18 Ghz signal to 1 Ghz in the absence of any

voltage bias. The mixer is first designed using Agilent's ADS software [14] and then fabricated using duriod. Presently, the accuracy of the ADS microstrip models is in general within 10% related to the actual measurement. The schematic and the layout of the mixer are respectively illustrated in Fig. 5.2.1a and Fig. 5.2.1b. In this design, the gap GAP1 serves as a DC/IF block for the RF input. The butterfly stub, STUB1 is employed as a virtual ground for the RF signal and to effectively maximize the RF voltage across the Quantum Barrier Device. Between the two high impedance lines, TL1 and TL2, is a sharp inductive end. The IF output is inductively terminated using a low pass filter, which enables the IF to be isolated from the fundamental mixing products between the RF and the LO signal.

As illustrated in the cross-sectional layer profile in Fig. 5.3.2, the Quantum Barrier Device used in this design featured two 4.3 nm $Al_{0.4}Ga_{0.6}As$ barriers and a 5.1 nm, undoped GaAs well [19]. The device diameter is around 10 microns, corresponding to the first order conductance 0.0016 mho. Instead of being mounted directly on microstrip, the device was wire-bonded in a leadless inverted device package (LID, see Fig. 5.3.3), which enables its orientation in the layout to be adjusted for the optimal mixing performance. At microwave frequencies, it is believed that the LID package will not contribute any excessive parasitic burden to the overall mixer design.

The measured symmetric conductance of the device is shown in Fig. 5.3.4, and was modeled in ADS [14] using the previously discussed step-function-based approach mentioned in Chapter 2. The frequency dependent characteristic was modeled as a voltage-dependent capacitance connected in parallel with the voltage-dependent conductance. The junction capacitance of the device was found by experiment to be weakly dependent on voltage and can be roughly modeled (using the methodology given in Chapter 2) as a voltage-dependent capacitance model shown in Fig. 5.3.5. In this regard, the nonlinear contribution due to the junction capacitance was taken care by allowing about 10% margin in some key parameters, including the total LO power required and the operating frequencies. With the RF being at around 18~20 Ghz and

the LO at about 8.5~9.5 Ghz, the whole design was optimized in ADS (formerly HPEESOF) [14] in such a way that the conversion loss is reduced to 7 dB at an LO power of around 0 dBm.

The measured results are shown in Fig. 5.2.6, According to the measurement, the best conversion loss was found to be 5 dB when the mixer was pumped at around 0 dbm and the RF applied at –20 dbm at 18.2 Ghz. The simulated minimum conversion loss is also in the neighborhood of 5 dB. The measured conversion efficiency initially agrees very well with the simulation results. But after the SMA in the IF port is soldered and tightened, the LO power required for optimum mixing was found to be –1.5 dBm to give a conversion loss at 6 dBm with slight shift in the RF/LO frequencies.

In addition to the conversion efficiency, the noise performance has also been measured. The experimental setup for noise measurement is demonstrated in Fig. 5.2.7. The noise was measured using the HP8970B Noise Figure Meter, which generates noise through the noise source to the Quantum Barrier Mixer and measures the noisy IF power from the mixer. The LO power source can be any CW Generator, such as HP8671B Synthesized CW Generator. Calibration was first done in a standard way to correct for the noise contribution of the measurement system (the HP8970B). The noise figure was measured by sweeping the LO power level and LO frequency. The best noise figure was found to be –9 dB, which occurred when the LO power was at 1 dB and 9.5 Ghz and the conversion loss was at 5 dB.

There was no success in obtaining W-band mixing using this Quantum Barrier Device structure, even when the device diameter was just 5 microns. The zero-bias capacitance, as given in Fig. 5.2.5, was found to be too high and caused a complete cut-off below W-band. Also, the skin resistances at both device terminals were expected to be excessively high. The doping level at the collector was around 2E+18 cm^{-3}, as opposed to other more general structures with collector doping level at 2E+19 cm^{-3}. Together, the skin loss and the unbiased junction capacitance contributed significantly to the overall low cut-off frequency being well below W-band. Hence, the W-band measurement were not pursued further for this work and in the time available.

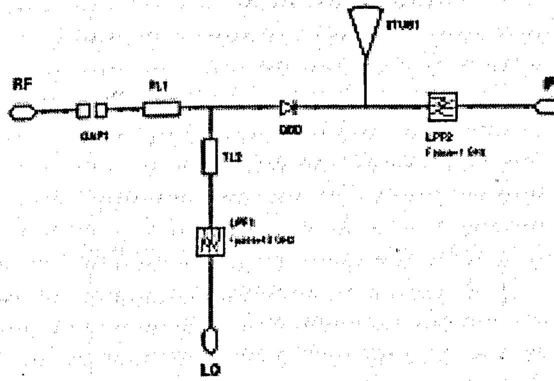

(a)

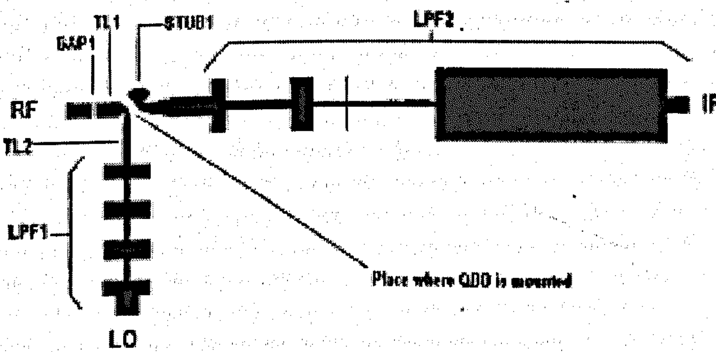

(b)

Fig. 5.2.1 Subharmonic 18-to-1 Ghz Quantum Barrier Mixer (a) Schematic Diagram; (b) Layout.

$0.5\mu m$, GaAs ($1*10^{18}$)
$0.1\mu m$, GaAs ($1*10^{17}$)
$5.1nm$, GaAs (updoped)
$4.3nm$, $Al_{0.4}Ga_{0.6}As$(undoped)
$5.1nm$, GaAs (updoped)
$4.3nm$, $Al_{0.4}Ga_{0.6}As$(undoped)
$5.1nm$, GaAs (updoped)
$0.1\mu m$, GaAs ($1*10^{17}$)
$2\mu m$, GaAs ($1*10^{18}$)
GaAs (N^{+})

Fig. 5.2.2 Layer Profile of the QBD used in this Experiment, Device Diameter=10 microns.

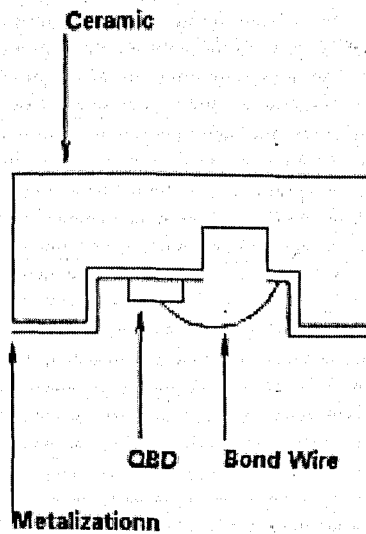

Fig. 5.2.3 QBD mounted in a LID package.

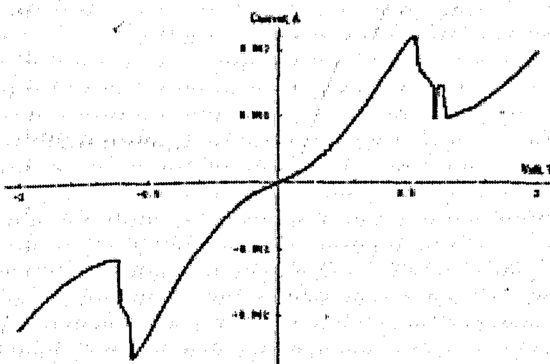

Fig. 5.2.4 Voltage-dependent Conductance of the QBD.

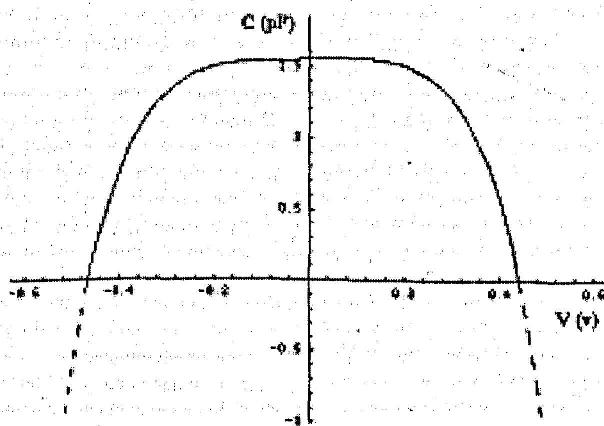

Fig. 5.2.5 Voltage-dependent Capacitance of the QBD (The dashed regions are interpolated regions).

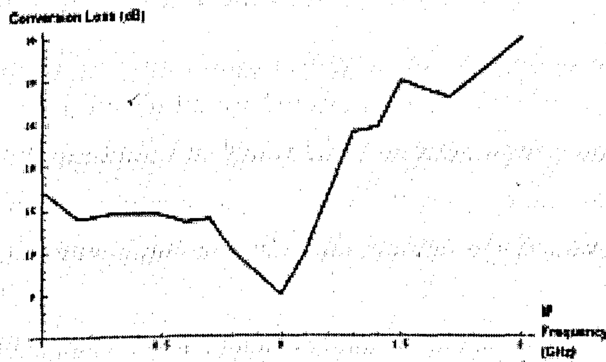

Fig. 5.2.6 Measured Conversion Loss versus IF Frequency (LO Power = 0 dBm, RF Power = -20 dBm, RF Frequency = 18 Ghz, Harmonic Number=2).

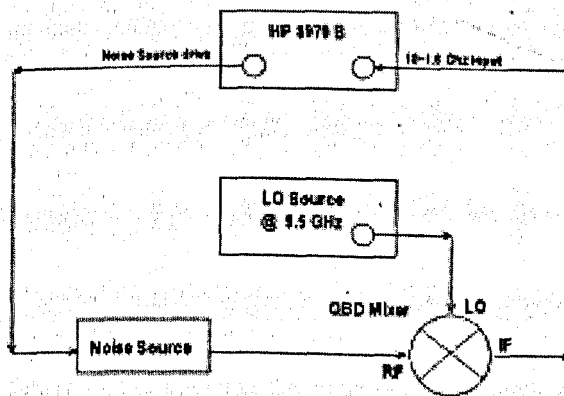

Fig. 5.2.7 Noise Measurement Setup (Measured Noise Figure = 9 dB).

5.3 QBD FREQUENCY MULTIPLIER, 20-TO-100 GHZ

Although not all of our Quantum Barrier Devices have been optimized as a mixing device operating at W-band frequencies, a multiplier based on a Quantum Barrier Device has been realized and was investigated over a range of bias voltages. The multiplier was designed to generate a submillimeter wave signal, using the fifth harmonic of a microwave frequency.

The device used in this study was a 10 micron-diameter double barrier GaAs-AlGaAs RTD, with asymmetric conductance. The layer profile and the current-voltage characteristic of this device are depicted in Fig. 5.3.1. The device capacitance was found to be roughly constant at 0.6 pF across the whole range of device voltages. By far, this device offers the lowest junction capacitance among all our devices. The low junction capacitance is possibly due to the capacitance offset effect by the n- substrate, which makes the current-voltage characteristic asymmetric. In addition to the relatively low junction capacitance, this device structure also has a relatively small voltage-independent conductance. Although the current-voltage characteristic is not symmetric, this is also the only device of ours that can work up to 100 Ghz in the absence of any bias. Apparently, the low junction capacitance and the small voltage-independent conductance consistently have a positive effect on the multiplier performance, as predicted in Chapter 3.

The circuit for this investigation is illustrated in Fig. 5.3.2. A sweep oscillator was used to provide a pump signal of 17 dbm at the frequency range 19 to 22 Ghz. The device was wire-bonded to the center of the coplanar-tee junction. The length of the open-circuit stub connected to the center of the coplanar-tee was adjusted, with the help of Agilent ADS [4], to give the maximum multiplier output. The bias of the device was achieved through the W-band wafer probe, which contains a built-in bias-tee, and which is also employed to capture the multiplier output.

The multiplication efficiency is measured over different bias voltages. The measured multiplier output against the bias voltage is plotted in Fig. 5.3.3. Fig. 5.3.4 shows the measured multiplier output in spectral domain for two different conditions: i.e. when the device was biased to 0.5 volt and when the device was unbiased. The multiplier output was maximum at around –39 dbm at around 100 Ghz, when the device is biased to 0.5 volts and input driven by a 20 Ghz signal at 17 dbm. The multiplier output at 103 Ghz became –42 dbm, when the input was driven by a 10 Ghz signal at 17 dbm and the bias was at 0.5 volts. This measurement agrees very well with the simulated performance (see Table 5.3), when a skin resistance of around 10 Ohm is assumed at the device terminals. The conversion efficiency in this experiment was not high, and the reason is, the author believe, that the circuit topology and the device physical structure were not optimized for frequency multiplication at submillimeter-wave frequencies.

$0.4\mu m$, GaAs ($2*10^{18}$)
$1.7\mu m$, GaAs (undoped)
$1.7nm$, AlAs (updoped)
$4.3nm$, GaAs(undoped)
$1.7nm$, AlAs (updoped)
$1.7nm$, GaAs(undoped)
$150nm$, GaAs ($1*10^{16}$)
$2\mu m$, GaAs ($1*10^{18}$)
GaAs (N^+)

(a)

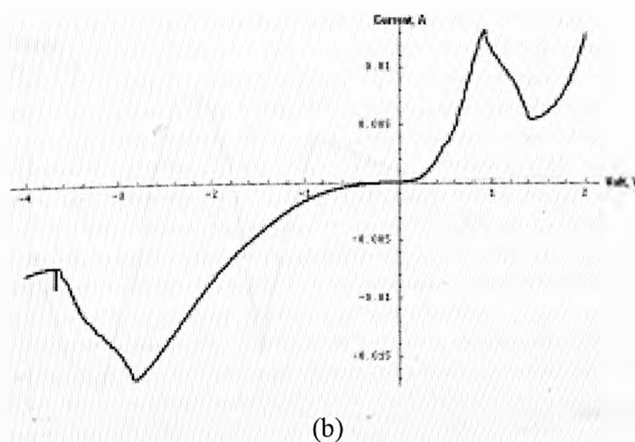

Fig. 5.3.1 Quantum Barrier Device used in the multiplier experiment (a) Cross-sectional layer profile [19]; (b) current voltage characteristic. (device diameter = 10 microns).

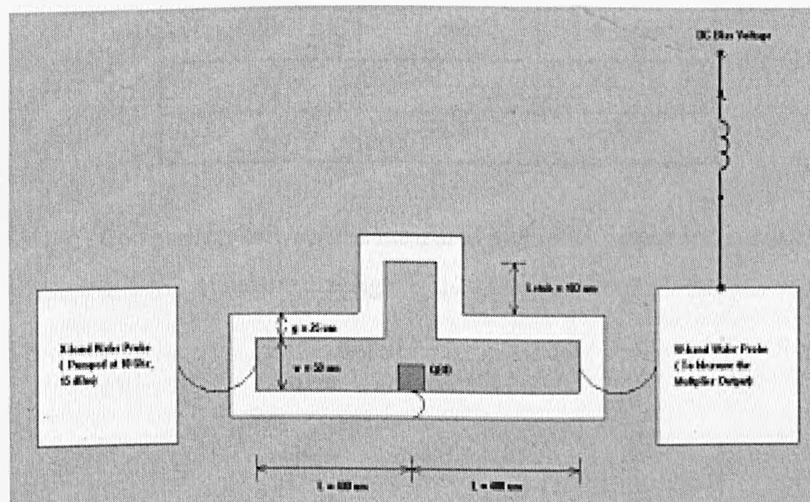

Fig. 5.3.2 Layout of the x5 Quantum Barrier Multiplier.

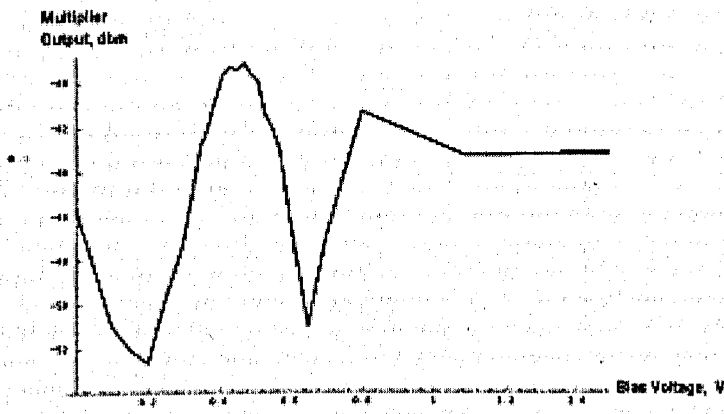

Fig. 5.3.3 Multiplier output versus bias voltage (fundamental signal @ 20 Ghz, 17 dbm).

Harmonic Index (freq=20GHz)	Measured Output (dbm)	Simulated Output (dbm)
3	-40.10	-40.10
4	-39.67	-39.50

Table. 5.3.1 Comparison between the measured multiplier output and simulated output. (fundamental signal @ 20 Ghz, 17 dbm)

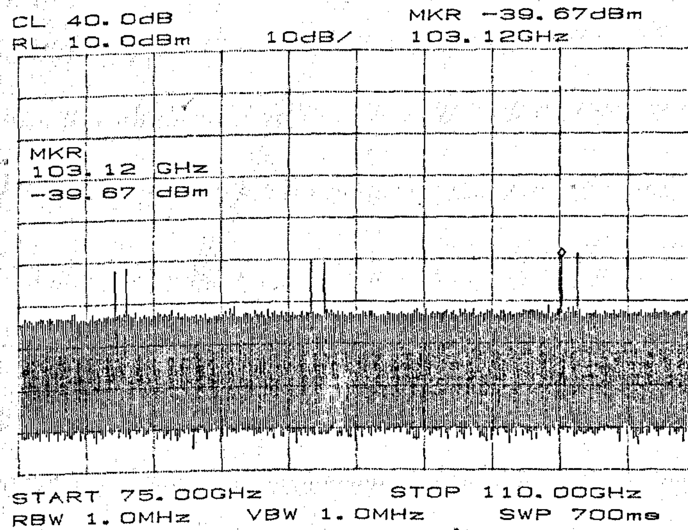

(a)

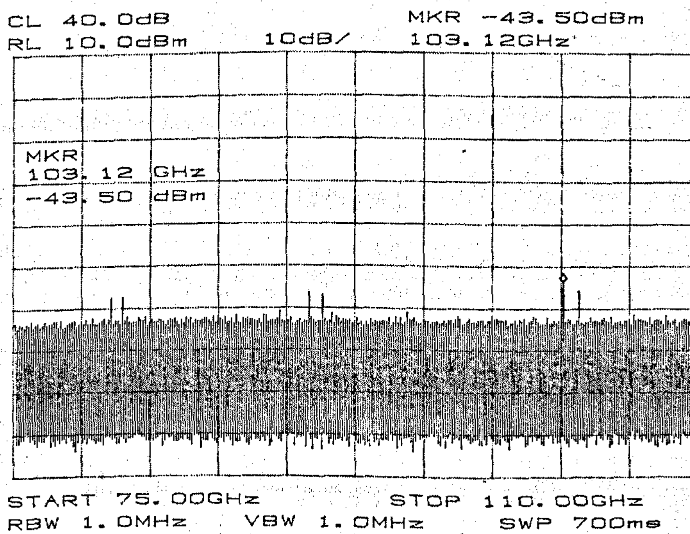

(b)

Fig. 5.3.4 (a) Mutiplier output measured in spectral domain the quantum barrier device is biased to 0.5 volts and (b) Multiplier output measured in spectral domain when the device is unbiased. (Input at 17 dbm, at 20 Ghz)

5.4 CONCLUSIONS

In this chapter, the theoretical and practical considerations which were discussed in the previous chapter have been applied to the design of a 18-to-1 Ghz subharmonically pumped (QBD) mixer, and a 20-to-100 Ghz (QBD) multiplier. Conversion efficiency in each case has been measured and compared with simulated performance based on the simulation model discussed in Chapter 2. Noise measurement at microwave frequencies has also been performed using the 18-to-1 Ghz QBD mixer.

REFERENCES

[1] W.Y. Liu, D.P. Steenson, "18-to-2 GHz Subharmonically Pumped downconverter using a Quantum Barrier Device with Symmetric Conductance", *PREP99*, IEE, Jan, 1999.

[2] W.Y. Liu, D.P. Steenson, "Investigation of Subharmonically Excited Quantum Barrier Mixers", *MTT-S* April, 2000.

[3] W.Y. Liu, D.P. Steenson, "Demonstration of Subharmonically Excited Quantum Barrier Mixers", *SPIE*, April, 1999.

[4] J.N. Schulman, H.J. De Los Santos, and D.H. Chow, "Physics-Based RTD Current-Voltage Equation", *IEEE Electron Device Letters*, Vol. 17, no. 5, May 1996

[5] Gerjuoy, E., and COON, D. D.: "Analytic S-matrix considerations and time delay in resonant tunneling', *Superlattices Microstruct.*, 5, (3), pp. 305-315, 1989

[6] E.R. Brown, O.B. McMahon, L.J. Mahoney and K.M.Molvar, “SPICE model of the rresonant-tunneling diode’, *Electronics Letter*, Vol.32, No.10, May 1996

[7] W. Y. Liu, M. B. Steer, D. P. Steenson, "Characterization of Nonlinear Device Capacitance in Frequency Domain," 8th *IEEE International Symposium on High Performance Electron Devices for Microwave and Optoelectronic Applications.*, pp. 253-258, Nov. 2000.

[8] Yuming Hu and Shawn P. Stapleton, "Double-Barrier Resonant Tunneling Transport Model" *IEEE Journal Of Quantum Electronics.*, Vol. 29, No. 2, pp. 327-339, Feb. 1993.

[9] D. L. Woolard, F. A. Buot, D. L. Rhodes, X Lu, and B. Sperlman, “An Assessment of Potential Nonlinear Circuit Models for the Characterization of Resonant Tunneling Diodes”, *IEEE Trans. on Electron. Devices.*, Vol. 43, No. 2, pp. 332

[10] Anthony E Parker, “A Realistic Large-Signal MESFET Model for SPICE”, *IEEE MTT-S Digest.*, Vol. 3, pp. 1763, 1996

[11] A. E. Parker, “Implementing high-order continuity and rate dependence in SPICE models”, *IEE Proc-Circuits Devices Syst.*, Vol. 141, No.4, August 1994

[12] T.R. Arabi, A. T. Murphy, T. K. Sarkar, R. F. Harrington and A. R. Diordjevic, “On the Modeling of Conductor and Substrate Losses in Multiconductor, Multidielectric Transmission Line Systems”, *IEEE Trans. On Microwave Theory and Techniques*, Vol. 39, pp. 1099-1237, July 1991

[13] J. I. Alonso, J. Borja and F. Perez, “A Universal Model for Lossy and Dispersive Transmission Lines for Time Domain CAD of Circuits”, *IEEE Trans. On Microwave Theory and Techniques*, Vol. 40, pp. 938-947, May 1992

[14] “User Manual”, Agilent ADS, 2001

[15] C. S. Yen, Z. Fazarinc, and R.L. Wheeler, “Time Domain Skin Effect model for Transient Analysis of Lossy Transmission Lines”, *Proceeding of the IEEE*, Vol 70, pp 750-767, 1982

[16] Kim S, and Neikirk D.P. , “Compact Equivalent Circuit Models for the Skin Effect”, *Microwave Symposium Digest, IEEE MTT-S International*, Vol 3, pp 1815-1818, 1996

[17] B.K. Sen and R. L. Wheeler, “Skin Effects models for Transmission Line Structures using Generic SPICE Circuit Simulators”, *Electrical Performance of Electronic Packaging,*

1998, IEEE 7th Topical Meeting, 98, pp 128-131, 1998

[18] Jan Genoe, C.V. Hoof, W.V. Roy, J.H.Smet, K. Fobelets, R. P. Mertens and G. Borghs, "Capacitances in Double-Barrier Tunneling Structures", *IEEE Trans. On Electron Devices*, Vol. 38, No. 9, Sep 1991

[19] D. P. Steenson, "High Frequency Applications of Quantum Barrier Devices," Doctor Dissertation, University of Leeds, 1994

[20] G.W.Rhyne, M.B.Steer, and B.D.Bates, " Frequency domain nonlinear circuit analysis using generized power series," *IEEE Trans. Microwave Theory Tech.*, Vol. 36, pp. 379-387, Feb. 1988

[21] C. R. Chang, M. B. Steer, and G. W. Rhyne, " Frequency domain spectral balance using the artithmetic operator method," *IEEE Trans. Microwave Theory Tech.*, Vol. 37, pp. 1681-1688, Nov. 1988

[22] A. Ushida and L. O. Chua, " Frequency domain analysis of nonlinear circuits driven by multi-tone signals," *IEEE Trans. Circuits Syst.*, Vol. CAS-31, pp. 766-779, Sept. 1984

[23] W.Y. Liu, D.P. Steenson, " Frequency-domain characterization of conductance and capacitance of Resonant Tunnelling Diode," *2001 International Symposium on Electron Devices for Microwave and Optoelectronic Applications*, EDMO 2001, Nov. 2001

Chapter 6: Future Work

6.1 INTRODUCTION

While the last few chapters have presented a technological groundwork for device modeling, and the theory of subharmonic mixing and micromachining work, there remain a number of unresolved issues, which cannot be addressed within such a short time frame. In this chapter, some of these unresolved issues are presented as future research topics. Particular reference will be given to the applications at microwave and millimeter wave frequencies.

6.2 REDUCTION OF VALLEY CURRENT IN RTD

The figure of merit of an RTD is largely determined by its peak-to-valley-current ratio --- a ratio of peak current to valley current in the negative differential resistance region. If the RTD is used as an oscillating device, a large peak-to-valley-current ratio is desirable as is a large voltage range over which this occurs , i.e. more available ac output power. In terms of nonlinearities for frequency-conversion purposes, a large peak-to-valley-current ratio can result in an output characteristic with rich high-order nonlinearities. According to our experiment (as mentioned in Section 2.3.2), cooling the quantum barrier device leads to a drop in the valley current and a slight rise in the peak current. In other words, the net ratio of peak-to-valley-current was found to increase as temperature decreases. The classical Boltmann transport model fails to explain this phenomenon. This suggests that the valley current is a function of temperature, whereas the peak current is not. The original standard formula suggested by Esaki at el [11] successfully predicts the current-voltage characteristic, but it does not account for the valley current. It has been suggested by some researchers [12] that the scattering of electrons is believed to be a cause of valley current, and this introduces a broadening of the total transmission coefficient. This broadening effect reduces the

peak-to-valley-current ration and increases the valley current. Since the ideality of an RTD is directly linked to the temperature-dependent valley current for most applications, more research on modeling the valley current is warranted.

6.3 PHYSICAL MODEL OF NONLINEAR RTD CAPACITANCE

In the past four decades, more than 3000 research articles have been published on various aspects of resonant tunneling diodes (RTD). Of these research publications, more than 60 per cent address the various issues of electronic transport in an RTD, with emphasis mainly on the current-voltage relationship. But in fact, the capacitance-voltage characteristic plays a highly critical role in determining the cut-off frequency of a device. So far, few papers have been published on modeling of device capacitance analytically, from a physical basis. Presently, the RTD has not gained any commercial interest, in part, because of the fact that there are not enough simulation models that reliably predict the frequency response. However, the present lack of commercial interest in RTDs does not rule out the possibility of another better device operating in Quantum mechanical principle. To be able to optimize the frequency-domain performance of a device, be it an RTD or not, we needs an empirical, but non-classical, capacitance-voltage model that can predict the capacitance from the physical parameters.

6.4 CASCADE OF MULTIPLE DOUBLE-BARRIER STRUCTURES AS A MIXING DEVICE, BY EPITAXIAL GROWTH

Sollner et al [13] and many other researchers following them have successfully demonstrated the terahertz oscillation by RTDs when used as an oscillating device. In fact, even though RTDs have not gained acceptance by this industry, the RTDs are considered by many as one of the candidate devices for terahertz engineering. However, like many other neglected semiconductor devices, the output power of an RTD in an RTD-based oscillator is generally too

small for many electronic applications. To get more power, it has been suggested to connect RTD's in series [19] so that the power output becomes a superimposition of all the individual RTD's output. The problem with this scheme is that it is not easy to bias all the serially connected RTD's correctly to obtain the desired oscillation. But this is only a minor restriction for oscillator design. Theoretically speaking, the parasitic effects of serially connected resonant tunneling lattice are distributed in nature. If the skin effect between two neighboring devices is negligible, there should be an added degree of freedom in impedance matching and in control of parasitics. There has not been any published analysis on the frequency-domain behavior and the frequency-conversion performance of a series of resonant tunneling diodes. Epitaxial growth of one layer currently costs around US$7000. It is not wise to go ahead with experimental investigation without theoretical groundwork. Thus, more analytical research on this series connected RTD lattice is warranted.

6.5 Leaky Wave Control and Optimal Thickness of Membrane in Planar Membrane-Supported CPWs

As mentioned in Chapter 4, a membrane-supported CPW without a cover is subject to radiation loss and leaky mode loss. One solution as suggested in Chapter 4 for the CPW is to have the metalization of the CPW totally encapsulated by the dielectric membrane, and suspended in mid-air within an enclosed environment. In order to obtain the best performance for this structure, we need to determine the height of the membrane and the membrane thickness. The condition for suppressing the leaky mode loss, as discussed by [3], requires that the phase velocity of the parallel TEM modes must be greater than the waveguide mode. Reference [3] employed a computationally-expensive spectra-domain analysis to determine if the said condition is satisfied. Reference [7] employs a more simplified approach to find the power coupling from the CPW mode to the parasitic parallel line mode, but still requires a numerically intensive finite element method to find the voltages and currents for these two modes. This can be too time-consuming, particularly if our purpose is just to determine the optimal dielectric thickness and its height from the bottom ground plane. In this regard, it is proposed to

develop a semi-empirical model which evaluates the near-optimal design parameters with reduced computational complexity.

6.6 CIRCUIT INTEGRATION BY HIGH RESOLUTION 3-D MICROMACHINING

One of the most painful issues in implementation of terahertz frequency circuits is to mount an active device to the circuit, which does not need to be 2-dimensional. Even an experienced expert in terahertz receiver design once admitted that it takes longer than a day or two to mount a device and to form a electrical contact. For years, the traditional (but painful) whisker contacting approach has been the standard technique and obviously needs a replacement. It is worth considering a solution from 3-D micromachining, which presently has gone to nanometric scale.

At present, most of the terahertz mixers were implemented on a dielectric-less membrane [14-19], with the active mixing device completely integrated into the circuit. In doing so, the parasitics due to wire-bonding can be significantly reduced. More importantly, more man-engineering hours can be shifted from "whiskering" to design optimization. Undeniably, our previously discussed micromachining techniques (mentioned in Chapter 4) still have a long way to go, particularly if the circuit to be implemented is non-planar. However, our micromachining techniques can be improved by taking advantages of the existing 3-D micromachining technologies that enable active devices an other high-resolution patterns to be directly written onto a polymer membrane. The candidates of the 3-D micromachining technologies are:

Microstereophotolithography With a microstereophotolithography process [8,9], a 2-D pattern at micron dimensions is directly written on the surface of a photopolymerizable resin by a moving focused light beam. During the process of writing, the light beam is repeatedly moved by a dynamic pattern generator, until the patterned areas are selectively polymerized. The

non-written areas remain liquid and can be striped off using an appropriate solvent. The photopolymerizable resin can be SU-8 or other thinner photoresists such as PNNA. Microstereophotolithography eliminates the need for a photomask. With this technology, 3-D structure can be obtained by vectorial tracing of light beam on the photopolymerizable resin layer by layer. The disadvantage of this technology is that, because of the wavelength of light and diffraction effects, the construction of structures of sizes below 250 nm is essentially out of reach.

Electron Beam Lithography Electron-beam lithography [10] employs the working principle of electron microscope technology, where a highly focused electron beam (of around 1 keV) is written directly onto a surface with a suitable resist material. It offers an advantage of not requiring a photomask to produce high definition surface structures in resist material. In principle, very fine structures well below 100 nm dimensions can be written. This technology has been extensively employed for mask making and for formation of quantum dots. The main disadvantage with this technique is that the low-mass electrons can easily scatter from the electrons in the resist material, and both the scattered and secondary electrons cause lateral spread due to proximity effects. As a result, the electron beam resolution achievable at the surface can quickly deteriorates as the beam penetrates the resist. As such, this technique is not suitable for high-resolution 3-D microstructures. Another disadvantage of this technique is that in general the process is too slow for commercial direct high volume batch production of micro-components.

High Energy Ion Beam Direct Writing High Energy Ion Beam micromachining [11] employs a scanning focused MeV ion beam to expose resist material. Unlike low-mass electron beams as discussed in the last paragraph, the high-energy ion beam has a very high penetrating power; e.g. 2 Mev protons will penetrate 62 micron2 in depth. The exposure rate with depth is also relatively uniform. The use of ion beams of different energies enables slots, channels and holes to be form with different depths. In addition, the angle of the resist surface can be adjusted with respect to the beam, and this allows complex non-prismatic shapes to be

machined. Rapid prototyping is possible. High energy ion beam micromachining has great potential for producing high aspect ratio 3-D submicron structures.

In terms of facility availability, the equipment for microstereolithography or 3-D photolithography can be easily implemented within a factory-based laboratory with a moderate investment. However, because of the resolution related problems, integrating a millimeter-wave circuit containing a quantum barrier device cannot be easily achieved with microstereolithography alone. Undoubtedly, high-energy ion beam writing offers a more promising solution to fabricate a small area containing an active device at nanometer scale. But the high-energy ion beam equipment is very scarce and the cost of implementing this technology is not easily affordable by a medium-size commercial organization. Electron-beam writing equipment is commonly available in almost all academic laboratories. However, writing design with large die area by electron-lithography is time consuming. The only option left here is apparently to combine electron-beam lithography with either 3-D photolithography or microstereolithography. It appears that all these techniques have their own advantages and disadvantages. In this regard, the author suggests that 3-D micromachining using a combination of these lithographical techniques should be further studied.

6.7 . CONCLUSIONS

In conclusion, this chapter has presented the following areas which represent the main unresolved issues during this research and which therefore warrant future study. In the presentation, particular attention has been given to applications in millimeter wave and submillimeter wave frequencies.

1) Further study of quantum mechanical behavior of valley current in such a way that the valley current can be suppressed by appropriate choice of physical parameters.

2) Analytical model of device capacitance for quantum barrier resonant tunneling diodes.

3) Nonlinear analysis of cascaded double-barrier structures as a frequency-conversion device.

4) Analytical model for leaky wave control and optimal thickness of membrane in planar membrane-supported CPW.

5) Integration of millimeter wave or submillimeter wave circuits by 3-D micromachining.

REFERENCES

[1] C. E. Collins, R. E. Miles, G. M. Parkhurst, J. W. Digby, H. Kazemi, J. M. Chamberlain, R. D. Pollard, N. J. Cronin, S. Davies, J. W. Bowen, and D. P. Steenson, "Use of novel photoresists in the production of submillimetre wave integrated circuits," *4th Int. Conf. on Millimeter and Submillimeter Waves and Applications, SPIE,* pp. 108–109, July 1998.

[2] J. W. Digby, C. E. McIntosh, G. M. Parkhurst, B. M. Towlson, S. Hadjiloucas, J. W. Bowen, J. M. Chamberlain, R. D. Pollard, R. E. Miles, D. P. Steenson, L. S. Karatzas, N. J. Cronin, and S. R. Davies, "Fabrication and characterization of micromachined rectangular waveguide components for use at millimeter_wave and terahertz frequencies", *IEEE Trans. Microwave Theory Tech.*, Vol. 48, pp. 1293–1302, Aug 2000.

[3] Y. Liu, K. Cha and T. Itoh, "Non-Leaky Coplanar (NLC) Waveguides with Conductor Backing", *IEEE Trans. Microwave Theory Tech.*, Vol. 43, pp. 1067–1072, May 1995.

[4] W. Y. Liu, D. P. Steenson and M. B. Steer, "A Simple but Novel Technique of Micormachining for Millimeter Wave and Submillimeter Wave Applications, *IWMF'2000* Workshop, Oct. 9-10, 2000.

[5] W. Y. Liu, "Novel Technique of Thin Photoresist Micromachining for Submillimeter Wave Circuits," *SPIE*, Vol 4176-28, September 2000

[6] W. Y. Liu, D. P. Steenson and M. B. Steer, "Mass-Produced Copper-On-Membrane Board for Millimeterwave Circuits," Submitted to *IEEE MTT-S.*

[7] K. Beilenhoff and W. Heinrich, "Parasitic Parallel-Plate Line Mode Coupling at Coplanar Discontinuities," Microwave Symposium Digest, 1997., *IEEE MTT-S*, Vol. 3 , 1997

[8] A. Bertsch, H. Lorenz and P. Renaud, "Combining Microstereolithography and thick Resist UV Lithographicy for 3-D Microfabrication", Micro Electro Mechanical Systems, 1998. MEMS 98. Proceedings., *The Eleventh Annual International Workshop* on , 1998, Page(s): 18 –23

[9] Maruo, S.; Ikuta, K.; Hayato, K. "Light-driven MEMS made by high-speed two-photon microstereolithography," *Micro Electro Mechanical Systems*, 2001. MEMS 2001. The 14th IEEE International Conference on , 2001, Page(s): 594 –597

[10] Frank Watt, "Focused High Energy Proton Beam Micromachining, A Perspective View", *Nuclear Instruments and Methods in Physics Research*, B. 158 (1999) 165-172, NIMB, Elsevier, Singapore.

[11] R.Tsu and L. Esaki, "Tunneling in a Finite Superlattice," *Applied Physics Letters*, vol. 22, pp. 562-564, 1973

[12] Wan-Rone Liou, and Patrick Roblin, "High Frequency Simulation of Resonant Tunneling Diodes," *IEEE Transactions on Electron Devices*, Vol., 41, No. 7. July 1994.

[13] E.R. Brown, T.C. L. G. Sollner, C. D. Parker, W. D. Goodhue and Chen, "Oscillations up to 420 Ghz in GaAs/AlAs resonant Tunneling Diodes," *Appl. Phys. Lett.*, vol. 55, no. 17, pp. 1777-1779, 1989

[14] P.H. Siegel, R.P. Smith, S. Martin and M. Gaidis, "2.5 THz GaAs monolithic membrane-diode mixer", *IEEE Trans. Microwave Theory and Tech.*, Vol. 47, No. 5, May 1999, pp. 596-604.

[15] Michael C. Gaidis, Herbert M. Pickett, C. D. Smith, Suzanne C. Martin, R. Peter Smith, and Peter H. Siegel, "A 2.5 THz receiver front end for spaceborne applications, " *IEEE Trans. Microwave Theory and Tech.*, Vol. 48, No. 4, April 2000, pp. 733-739.

[16] N. R. Erickson, R.P Smith, S. C. Martin, B Nakamura, and I. Mehdi, "High efficiency MMIC frequency triplers for millimeter and submillimeter wavelengths," *2000 IEEE MTT-S Int. Microwave Symp. Dig.*, Vol. 2, pp. 1003-1006, June 2000.

[17] A. Maestrini, D. Pukala, F. Maiwald, E. Schlecht, G. Chattopadhyay, and I. Mehdi, "Cryogenic operation of GaAs based multiplier chians to 400GHz," proceedings of the *8 th International Conference on Terahertz Electronis*, Darmstadt, 28-29 September 2000.

[18] F. Maiwald, S. Martin, J. Bruston, A. Maestrini, T. Crawford, I. Mehdi, and P. H. Siegel, "2.7 THz waveguide tripler using monolithic membrane diodes (MOMED)," *2001 IEEE MTT-S Int. Mic. Sym.*, Dec. 2001

[19] Suzanne Martin, Barbara Nakamura, Andy Fung, Peter Smith, Jean Bruston, Alain Maestrini, Frank Maiwald, Peter Siegel, Erich Schlecht, and Imran Mehdi , " Fabrication of 200 to 2700 GHz Multiplier Devices using GaAs and Metal Membranes", *IEEE MTT-S International Microwave Symposium*, Phoenix, Arizona, May 20-25, 2001

Chapter 7: Conclusions

7.1 INTRODUCTION

This chapter summarizes and emphasizes the salient features of the previous chapters, and provides an assessment of the significance of the results of this research.

7.2 SUMMARY AND CONCLUSIONS

The purpose of this research was to study the behavior of subharmonic mixing employing double barrier resonant tunneling device (Quantum Barrier Device) at microwave and millimeter wave frequencies and to develop an enabling technology for the Quantum Barrier mixer at or above millimeter wave frequencies. In summary, the following are the achievements during this research:-

4) Develop of current-voltage characteristic for the Quantum Barrier Device using continuity function approach to model sharp discontinuities along its characteristic that cannot be accurately curve-fitted using conventional regression algorithms and the physical models available in the open literature.
5) Examination of the harmonic content resulting from abrupt transitions in the electrical characteristic of the Quantum Barrier Device, with suggestions on possible structural modifications to the device which would potentially lead to improvements in the mixing performance.

6) Development of a technique to extract the nonlinear capacitance model of the Quantum Barrier Device in the frequency domain, using the available nonlinear conductance model and the frequency-domain measurements.
7) Derivation of a general theory of subharmonic mixing, with particular attention given to subharmonic mixing using a quantum barrier device.
8) Demonstration of the factors which favor the use of a Quantum Barrier Diode as a mixing device at microwave frequencies and revealing any shortcomings, with analysis and experimental proof.
9) Realization of a Quantum Barrier Mixer downconverting 18 Ghz to 1 Ghz in the absence of any bias, with the lowest conversion loss at 7 dB.
10) Development of a low-cost micromachining technology with performance comparable to the existing GaAs (or Silicon) membrane technology, for integration of these high frequency devices in the future, with successful implementation of the following:-

    a) Embedded-polymer-based waveguide;
    b) Polymer-membrane-supported coplanar waveguides;
    c) Polymer-membrane-supported copper E-plane circuits; as well as
    d) A copper-on-membrane board methodology for mass-production of membrane-supported circuits.

The following section once again outlines the significant aspects of Chapter 2-6:

In Chapter 2, the all modeling aspects of a resonant tunneling diode were presented, with a brief review on the shortcoming of the physics-based modeling. The negative resistance regions of an RTD are highly discontinuous. Thus, to be able to model the discontinuities exactly, a chain of step-function based continuity functions were incorporated into our measurement based modeling of the current-voltage characterisitic. The capacitance-voltage characteristic was then extracted in the frequency domain using the current-voltage characteristic and the spectral domain measurements.

In Chapter 3, the general subharmonic mixing theories were presented with particular reference given to subharmonic mixing using a quantum barrier RTD. The features of an RTD in mixing applications were further elaborated to provide suggestions on how to optimize the mixing performance by tailoring the nonlinearities of the device characteristics.

Chapter 4 presented several novel polymer-based micromachining technologies, which were originally intended for future implementation of a Quantum Barrier mixer operating at submillimeter wave frequencies. These polymer-based micromachining techniques, including polymer-membrane-supported coplanar waveguides, polymer-membrane-supported copper E-plane circuits and copper-on-polymer-membrane boards, have been demonstrated with VNA measurements at W-band frequencies. Some critical transmission parameters affecting the efficiency of the existing membrane-supported CPWs were identified, with self-contained analytical derivations where possible. These parameters include the relative dielectric constant of membrane-supported CPW, dispersion effects, dielectric loss and the radiation loss due to leaky parallel plate mode.

In Chapter 5, measurements of a mixer at microwave and a frequency multiplier at millimeter wave frequencies were carried out. According to the measurement, the conversion loss of the microwave subharmonic mixer using our Quantum Barrier Device was found to be less than 7 dB at 18 Ghz, which was slightly better than the simulated conversion loss at this frequency. The noise figure is around 9 dB using an LO pump at 20 dBm at 18.5 Ghz. Our x5 frequency multiplier has not been optimized for efficient frequency multiplication and thus the measured conversion efficiency was not considered as a conclusion. Most of our available resonant tunneling devices were found to cut off at around 40 Ghz, which significantly degrades the frequency-conversion efficiency at W-band.

Chapter 6 helps to draw this work to a conclusion by pointing the way to future work for this research. The future work covers some remaining unresolved issues of the RTD modeling

work, and feasibility study of total integration for applications at millimeter wave and sub-millimeter wave frequencies.

Appendix 1 -- Listing of Harmonic Decomposition Program

```
#include <stdio.h>
#include <math.h>
#define pi 3.1415926

/**************************************************

This program demonstrates harmonic decomposition on a
nonlinear i-v characteristic, V=I^3.

The i-v characteristic and LO voltage and the RF
voltage need to be changed if this program is used
to model real-life example. The I-V characteristic and
the signal v are to be specified by users. Basically,

1) To specify the rf and lo, please modify the function "v".

2) To specify the i-v, please modify the function "i".

To use this program, please first compile the code.
For instance, if the platform is UNIX, then the following
command can be used to compile the source code into run-
time executable:

> gcc -o decomp decomp.c -lm

To run this software, simply enter "decomp" if the
```

platform is UNIX. The run log will appear as follows:

```
Coefficient of harmonic ( 0*wlo + 0*wrf) = -0.000008 + j*0.000000
Coefficient of harmonic ( 0*wlo + 1*wrf) = 509.999993
+ j*0.000011
Coefficient of harmonic ( 0*wlo + 2*wrf) = -0.000009 + j*0.000021
Coefficient of harmonic ( 0*wlo + 3*wrf) = 160.000005
+ j*0.000006
Coefficient of harmonic ( 1*wlo + 0*wrf) = 461.249992
+ j*0.000009
Coefficient of harmonic ( 1*wlo + 1*wrf) = -0.000020 + j*0.000014
Coefficient of harmonic ( 1*wlo + 2*wrf) = 179.999997
+ j*0.000018
Coefficient of harmonic ( 1*wlo + 3*wrf) = 0.000009 + j*0.000023
Coefficient of harmonic ( 2*wlo + 0*wrf) = -0.000009 + j*0.000018
Coefficient of harmonic ( 2*wlo + 1*wrf) = 134.999996
+ j*0.000016
Coefficient of harmonic ( 2*wlo + 2*wrf) = -0.000005 + j*0.000011
Coefficient of harmonic ( 2*wlo + 3*wrf) = -0.000000 + j*0.000010
Coefficient of harmonic ( 3*wlo + 0*wrf) = 67.500005 + j*0.000016
Coefficient of harmonic ( 3*wlo + 1*wrf) = 0.000007 + j*0.000022
Coefficient of harmonic ( 3*wlo + 2*wrf) = 0.000001 + j*0.000011
Coefficient of harmonic ( 3*wlo + 3*wrf) = -0.000000 + j*0.000006

****************************************************/


#define max_harmonic_index_lo 6
#define max_harmonic_index_rf 6

double v(double w_lo_t, double w_rf_t)
{
```

```
/*****************************************************
 This function is to be modified by the user. The content
 is currently defaulted to vlo = 3.0 * cos( wlo * t) and
 vrf = 4.0 * cos( wrf*t) as an example.
 *****************************************************/
        double v1;
        double v2;
        double v;

        v1 = 3.0 * cos( w_lo_t);
        v2 = 4.0 * cos( w_rf_t);
        v = v1 + v2;
        return (v);
}

double i(double v)
{

/*****************************************************
 This function is to be modified by the user. The content
 is currently defaulted to i=v^3 as an example.
 *****************************************************/


        double i;
        i = 5.0*pow(v, 3.0);
        return ( i );
}
```

```
double coeff_r (int m_lo, int m_rf)
{

/*****************************************************

 This function performs harmonic decomposition using
 Equation 3.2.43 in Chapter 3 and the output is the
 real part of the coefficient of harmonic

        m_lo * wlo + m_rf *wrf

 where m_lo and m_rf denote the harmonic index for the
 LO and the RF respectively.

*****************************************************/

        int nn_lo, nn_rf;
        double n_lo, n_rf;
        double N_lo, N_rf;
        double sum_r = 0.0;
        double sum;
        double q=2.0;


        for( nn_lo=0; nn_lo<=max_harmonic_index_lo-1; nn_lo++)
                for( nn_rf=0; nn_rf<=max_harmonic_index_rf-1;
                    nn_rf++)
                        {

                          n_lo = (double) nn_lo;
```

```
                    n_rf = (double) nn_rf;
                    N_lo = (double) max_harmonic_index_lo;
                    N_rf = (double) max_harmonic_index_rf;


                    sum_r  += 1.0/( N_lo* N_rf) *
                    i(v(2.0 * pi * n_lo/N_lo,
                       2.0 * pi * n_rf/N_rf))
                    * cos ( 2.0 * pi * ((double)m_lo*n_lo/N_lo

                                   +
                        (double)m_rf*n_rf/N_rf) ) ;



                    }

    if (m_lo != max_harmonic_index_lo
            && m_rf != max_harmonic_index_rf )
                        q=2.0;
    if (m_lo == 0 && m_rf == 0 )
                        q=0.5;
    if (m_lo == max_harmonic_index_lo
            || m_rf == max_harmonic_index_rf )
                        q=1.0;
    if (m_lo == 0 && m_rf == max_harmonic_index_rf )
                        q=0.5;
    if (m_lo == max_harmonic_index_lo && m_rf == 0 )
                        q=0.5;
    sum_r = sum_r * q;

    return (sum_r);
```

```
}

double coeff_i (int m_lo, int m_rf)
{

/****************************************************

 This function performs harmonic decomposition using
 Equation 3.2.43 in Chapter 3 and the output is the
 imaginary part of the coefficient of harmonic

       m_lo * wlo + m_rf *wrf

 where m_lo and m_rf denote the harmonic index for the
 LO and the RF respectively.

 ****************************************************/

       int nn_lo, nn_rf;
       double n_lo, n_rf;
       double N_lo, N_rf;
       double sum_i = 0.0;
       double q;


       for( nn_lo=0; nn_lo<=max_harmonic_index_lo-1; nn_lo++)
              for( nn_rf=0; nn_rf<=max_harmonic_index_rf-1;
                     nn_rf++)
                     {

                     n_lo = (double) nn_lo;
```

```
            n_rf = (double) nn_rf;
            N_lo = (double) max_harmonic_index_lo;
            N_rf = (double) max_harmonic_index_rf;

            sum_i  += 1.0/( N_lo* N_rf) *
            i(v(2.0 * pi * n_lo/N_lo,
               2.0 * pi * n_rf/N_rf))
            * sin ( 2.0 * pi * ((double)m_lo*n_lo/N_lo

                              +
                  (double)m_rf*n_rf/N_rf) ) ;

            }

    if (m_lo != max_harmonic_index_lo
          && m_rf != max_harmonic_index_rf )
                        q=2.0;
    if (m_lo == 0 && m_rf == 0 )
                        q=0.5;
    if (m_lo == max_harmonic_index_lo
          || m_rf == max_harmonic_index_rf )
                        q=1.0;
    if (m_lo == 0 && m_rf == max_harmonic_index_rf )
                        q=0.5;
    if (m_lo == max_harmonic_index_lo && m_rf == 0 )
                        q=0.5;
    sum_i = sum_i * q;

    return (sum_i);
}
```

```
int main()
{

/******************************************************

 This main function of the program print out the
 harmonic content in complex number.

 ******************************************************/
        int i , j;

        for (i=0; i<= max_harmonic_index_lo/2; i++)
                for (j=0; j<= max_harmonic_index_rf/2; j++)
        {
          printf(
  "Coefficient of harmonic ( %d*wlo + %d*wrf) = %f + j*%f\n",
          i, j, coeff_r( i,j), coeff_i(i,j));
        }
        return;
}
```